Advanced Instrumental Approaches to Study the Fate and Distribution of Emerging Chemical Pollutants

by
Misha Zvekic

B.Sc., Vancouver Island University, 2021

A Thesis Submitted in Partial Fulfillment of the
Requirements for the Degree of

MASTER OF SCIENCE

in the Department of Chemistry

Advanced Instrumental Approaches to Study the Fate and Distribution of Emerging Chemical Pollutants

by

Misha Zvekic
B.Sc., Vancouver Island University, 2021

Supervisory Committee

Dr. Erik Krogh, Supervisor
Department of Chemistry

Dr. Chris Gill, Departmental Member
Department of Chemistry

Dr. Dennis Hore, Departmental Member
Department of Chemistry

Abstract

As novel chemicals and materials are discovered and manufactured, the concentration and diversity of environmental contaminants increase. The fate and distribution of contaminants depend both on intrinsic chemical properties and extrinsic environmental conditions. When chemicals pollute water, they can leave that environmental compartment via loss to the air, sorption processes (e.g., to soils, plants, microplastics), or accumulation in organisms. Some contaminants persist over long timescales, eventually degrading or transforming. To understand and predict contaminant behaviour, it is key to characterize their physicochemical properties and analyze their environmental partitioning. Here, mass spectrometry (MS) is employed to achieve the sensitivities required to analyze chemicals at environmentally relevant concentrations. A direct MS approach, condensed phase membrane introduction mass spectrometry (CP-MIMS), is used to investigate legacy pollutants such as polycyclic aromatic hydrocarbons (PAHs), and emerging pollutants such as microplastics, nonylphenol, and *para*-phenylenediamine quinones (PPDQs). Using CP-MIMS, the sorption kinetics (k'_{sorb}) and thermodynamics (K_{OC}) between microplastics and chemical contaminants (nonylphenol and PAHs) were analyzed. Plastic and sediment partitioning and aqueous solubility of PPDQs were also characterized. Lastly, chemical partitioning was analyzed in a pregnant sixgill shark (*Hexanchus griseus*) collected from the Strait of Georgia in 2019. CP-MIMS was initially used and provided important preliminary data that informed the application of appropriate conventional approaches. High resolution mass spectrometry (HRMS) and inductively coupled plasma optical emission spectroscopy (ICP-OES) was used to analyze the concentrations and maternal transfer of perfluoroalkyl substances (PFAS) and heavy metals, respectively, in this unique biological specimen.

Table of Contents

List of Tables

List of Figures

List of Abbreviations and Symbols

C_w^{sat}	aqueous solubility
6PPDQ	6PPD-quinone
6PPD-quinone	*N*-(1,3-dimethylbutyl)-*N*'-phenyl-*para*-phenylenediamine-quinone
77PDQ	77PD-quinone
Ag	silver
ANT	anthracene
ATR-FTIR	Attenuated Total Reflection Fourier Transform Infrared
Ba	barium
BCF	bioconcentration factor
Be	beryllium
Bi	bismuth
Ca	calcium
Cd	cadmium
CI	chemical ionization
Co	cobalt
CP-MIMS	condensed phase membrane introduction mass spectrometry
CPPDQ	CPPD-quinone
Cr	chromium
CRM	certified reference material
Cu	copper
DI	deionized
DIA	Data Independent Acquisition
DMS	direct analysis with mass spectrometry
DPPDQ	DPPD-quinone
DTPDQ	DTPD-quinone
dw	dry weight
EI	electron ionization
ESI	electrospray ionization
Fe	iron
f_{OC}	fraction of organic carbon
GC	gas chromatography
HDPE	high-density polyethylene
HRMS	high resolution mass spectrometry
ICP	inductively coupled plasma
ICP-MS	inductively coupled plasma mass spectrometry
ICP-OES	inductively coupled plasma optical emission spectroscopy
IPA	2-propanol/isopropanol
IPPDQ	IPPD-quinone
K_a	acid dissociation constant
K_{AW}	air-water partition coefficient
K_D	sorption partition coefficient
k'_{loss}	analyte depletion rate constant
k'_{obs}	observed rate constant

K_{OC}	organic carbon-water partition coefficient
K_{OW}	octanol-water partition coefficient
k'_{sorb}	sorption rate constant
LC	liquid chromatography
LDPE	low-density polyethylene
LOD	limit of detection
lw	lipid weight
sd	standard deviation
SoG	Strait of Georgia
SoM	Strait of Messina
methanol	MeOH
Mg	magnesium
Mn	manganese
Mo	molybdenum
MRM	Multiple Reaction Monitoring
MS	mass spectrometry
MS/MS	tandem mass spectrometry
MTR	maternal transfer ratio
m/z	mass-to-charge ratio
NAP	naphthalene
Ni	nickel
NON	nonylphenol
PAH	polycyclic aromatic hydrocarbon
Pb	lead
PBDE	polybrominated diphenyl ether
PCB	polychlorinated biphenyl
PDMS	polydimethylsiloxane
PFAS	perfluoroalkyl substances
PFBA	perfluorobutanoic acid
PFBS	perfluorobutane sulfonate
PFCA	perfluorocarboxylic acid
PFDA	perfluorodecanoate
PFDoDA	perfluorododecanoate
PFDoS	perfluorododecane sulfonate
PFDS	perfluorodecane sulfonate
PFHpA	perfluoroheptanoate
PFHpS	perfluoroheptane sulfonate
PFHxA	perfluorohexanoate
PFHxDA	perfluorohexadecanoate
PFHxS	perfluorohexane sulfonate
PFNA	perfluorononanoate
PFNS	perfluorononane sulfonate
PFOA	perfluorooctanoate
PFOcDA	perfluorooctadecanoate
PFOS	perfluorooctane sulfonate

PFPeA	perfluoropentanoate
PFPeS	perfluoropentane sulfonate
PFSA	perfluorosulfonic acid
PFTeDA	perfluorotetradecanoate
PFTrDA	perfluorotridecanoate
PFUnDA	perfluoroundecanoate
POP	persistent organic pollutant
p^*	vapour pressure
PP	polypropylene
PPD	*para*-phenylenediamine
PPDQ	*para*-phenylenediamine quinone
PS	polystyrene
PYR	pyrene
RSD	relative standard deviation
RT	retention time
SoG	Strait of Georgia
SoM	Strait of Messina
Sr	strontium
SRM	Selected Ion Monitoring
TWPs	tire wear particles
UV	ultraviolet
V	vanadium
Zn	zinc

Acknowledgements

For **Chapter 2** and **Chapter 3**. This author acknowledges Vancouver Island University and University of Victoria for ongoing support of the Applied Environmental Research Laboratories and students. Thanks to Agilent Technologies for funding (UCR Grant# 4088) and providing the 7010 triple quadrupole mass spectrometer, and to LifeLabs for providing 5975 single quadrupole mass spectrometer. Research was supported through the Natural Sciences and Engineering Research Council of Canada (Discovery RGPIN-2022-05349 ETK, RGPIN-2021-02981 CGG, USRA MZ, and CGS-M MZ).

For **Chapter 4**. This author acknowledges Vancouver Island University, University of Victoria, University of Toronto, and the Canadian Graduate Student Research Mobility Protocol for supporting this work. Research was supported through the Natural Sciences and Engineering Research Council of Canada (Discovery RGPIN-2022-05349 ETK, USRA MZ, and CGS-M MZ). Special thanks to Dr. Garth Covernton for collecting and providing the specimens, and to Dr. Erick Groot and Cecile Van Woensel for their support. Thank you to Dr. Philip Morrison and our anonymous reviewers for sharing their insights into shark biology.

Thank you to every administrator that has organized my research funding. Thank you to my committee member Dr. Dennis Hore for his insights and support of this work.

Special thanks to my professors who challenged and changed me. Thanks to Dr. Chris Gill for seeing my potential and giving me my first work opportunity. Thanks as well to Dr. Christine Tong for supporting me in my first research project and mentoring me throughout the years. Thank you to Peter Diamente for teaching me the joys of instrumentation. Thank you, Dr. Larissa Richards, for your support through research and through loss. Above all, thank you, Dr. Erik Krogh. Without you, I never would have heard my calling in chemistry.

To my colleagues, I want to single out a few though I have been helped by many more. Thank you, Dr. Gregory Vandergrift, for your encouragement and mentorship when I was an undergraduate researcher. Thank you, Joseph Monaghan (soon to be Dr.), it was always exciting to work with you. I would like to thank Angelina Jaeger, Jon Davidson, Simon Maguire, and Lily Eggert for their support and encouragement through this degree. Thank you to Holly Barrett (also soon to be Dr.), and the rest of the Peng Group for sharing your expertise, humour, and city with me.

Thank you to my friends: I am honoured at the number of you, and you have helped me through this time directly and indirectly. Thanks to my family for their support throughout my university degrees, the completion of which would not be possible without you, especially my mother to whom I owe much.

I would like to thank the music of Darlingside, Graveyard Club, and Anaïs Mitchell (among others) for shepherding me.

Dedication

I am thankful to the people I have lost for having known them for the time that I did. I am forever changed by you.

Thank you, Armin Saatchi, for being who you were and so well.

Thank you, Dad, especially, for always humouring me and for valuing gentleness. I will miss you always, my friend.

i carry your heart with me(i carry it in

my heart)

— E. E. Cummings

Chapter 1: Introduction

1.1 Fate and distribution of trace pollutants

In the 21st century, increased urbanization has led to a rising number of anthropogenic environmental contaminants.[1–3] A contaminant is defined as substances present at higher levels than expected or ideal, and may be pollutants with adverse biological impacts.[4] The diversity of chemicals (e.g., perfluoroalkyl substances) and materials (e.g., plastics) polluting the environment increase as new substances are created and used.[5] The distribution and fate of environmental contaminants involves many compartments as illustrated in **Figure 1.1.1** including water, sediment, air, and biota.[6] The physical and chemical properties of a chemical govern its environmental partitioning, and a compound released in the environment may not stay where it was first introduced. Aquatic contaminants are of particular concern because water sources are often biota-rich and can function as highways for the distribution of contaminants across large geographical areas.[7] Aquatic contaminants can exit that environmental compartment via loss to the atmosphere, sorption to other matrices (such as sediments, plants, plastics), or bioaccumulation within organisms.[5,6] Compounds that remain in the bulk aquatic phase will eventually undergo physical, chemical, or biological transformation into different compounds.[6,8] Chemistry creates chemicals and materials which benefit humanity but can result in unintended environmental consequences. Just as true, the only means to understand and solve such problems lie in chemistry.

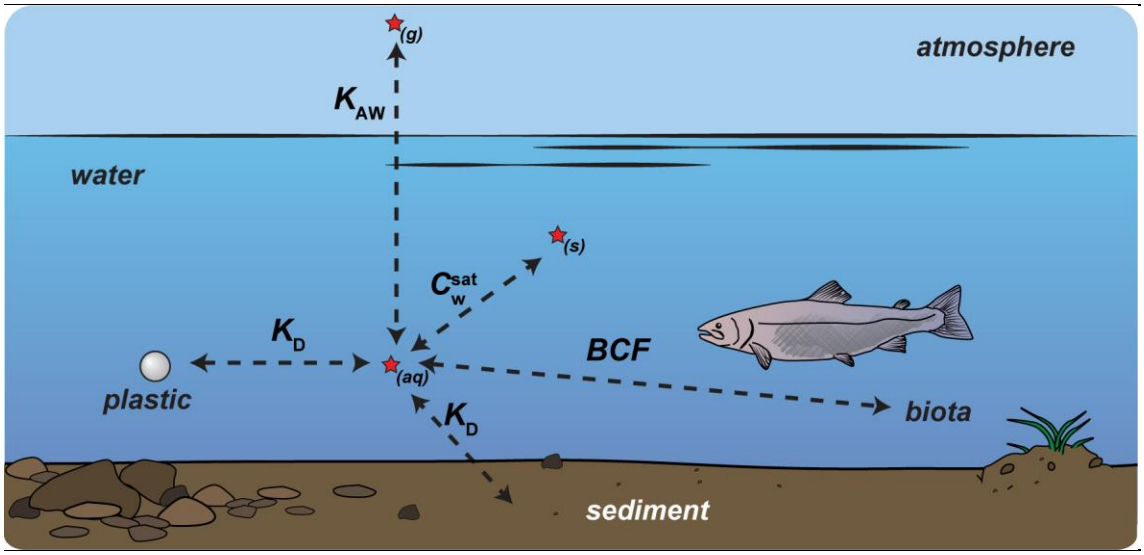

Figure 1.1.1. Potential distribution pathways for a chemical (represented here by a red star) within and out of an aquatic environment. The processes are governed by air-water partitioning (K_{AW}), sediment- and plastic-water partitioning (K_D), aqueous solubility (C_w^{sat}), and bioconcentration (which can be measured with a bioconcentration factor (BCF)).[9]

The level of risk of a compound is increased with its toxicity, environmental persistence, mobility, and bioaccumulation potential, all of which are relevant to

environmental impact.[10] The more persistent, or resistant to degradation a compound is, the longer its half-life.[6] The more mobile, the greater global distribution it will have. Many persistent organic pollutants (POPs) display toxicity effects at trace concentrations, such as 6PPD-quinone which has a LC_{50} for juvenile coho in the part per billion (ppb) range (95 μg L^{-1}).[11] Bioaccumulation can result in biomagnification up a food web,[8] culminating in threateningly high levels in apex predators.[12] For example, polychlorinated biphenyls (PCBs) have been banned near-globally for decades because of their carcinogenicity, but despite bans and low environmental concentrations (ppb), the levels within organisms are known to accumulate to concentrations 1000× that observed in the water column,[13] even up to 1300 mg kg^{-1} in orca blubber.[12] To fully understand the behaviour of a given contaminant in the environment, both its fate and distribution must be considered. This analysis can be accomplished via chemical measurement of the contaminant's physicochemical properties and its abundance in different environmental compartments.

Within its lifetime, the environmental partitioning of a compound is governed by its specific physicochemical properties. To what extent a compound exists in the atmosphere, dissolved in water, or bound to sediment depends on many factors including air-water partitioning (K_{AW}), sediment sorption equilibria (K_D), solubility (C_w^{sat}), hydrophobicity (K_{OW}), and vapour pressure (p^*).[9] Contaminants that accumulate in organisms at greater rates than they are excreted bioaccumulate, and to what extent and where this occurs is also compound specific. Hydrophobic, lipophilic organic pollutants tend to accumulate in fatty tissue including livers, while elemental contaminants may accumulate in other organs (e.g., both necessary Ca^{2+} and toxic Pb^{2+} accumulate in bones)[14] depending on their size, charge, and polarizability.[6] Some contaminants may be passed from mother to offspring through a process termed maternal transfer, however the potential for this process to occur, and its efficiency, is governed by species-specific biological transfer mechanisms and the properties of the compounds. Characterizing and controlling environmental contaminants is a monster of many heads, as both old and new chemicals and materials are discovered to be contaminants of concern. Characterization of physicochemical properties enables predictive modelling to help achieve a better understanding of the fate and impact of environmental contaminants.[15]

The fate of a contaminant encompasses the changes that can occur to the compound. Contaminants can weather physically via exposure to physical and chemical processes, with their physical and chemical properties changing accordingly. They can chemically transform via oxidation (such as photo-oxidative or thermo-oxidative weathering) or reduction processes. Metabolic processes within biota may also transform contaminants into different chemical forms or different compounds altogether. Elemental compounds can change their oxidation state, their chemical speciation, or may decay into a different element if they are unstable but are otherwise significantly more persistent than organic contaminants.[6] Ultimately, even the most persistent organic pollutants will eventually oxidize or reduce completely.

Differing chemical properties result in multiple categories and levels of risk and thus specific regulations for contaminants of concern. There are many classes of pollutants, with different regulatory bodies placing suggestions, limitations, and bans for the allowable

concentration levels released to the environment and levels permissible in drinking water.[16] The Stockholm Convention on Persistent Organic Pollutants in 2001 organized a list of such compounds with the aim of eliminating organic contaminants that are persistent, bio-accumulative, and pose risk to human and environmental health. The list of contaminants of emerging concern is always being refined and updated with new information,[17] and which contaminants are considered 'emerging' is a matter of perspective. Certain legacy pollutants persist ubiquitously in the environment, even after the enforcement of stringent regulations and bans as is the case with PCBs.[12] Some 'older' pollutants may never be meaningfully eliminated in our lifetimes, but the longer a harm has been known, the more time scientists have been given to study the contaminant with the aim of implementing remediation efforts and preventing future harm.

Heavy metals and polycyclic aromatic hydrocarbons (PAHs) are examples of ubiquitous and persistent environmental pollutants.[18] Some metals are necessary for biological health, but others can be incredibly toxic. Some PAHs have been classified as carcinogenic or possibly carcinogenic to humans.[5] Both types of contaminants have been found to accumulate in organisms and persist over long timescales (e.g., decades in the case of select PAHs, while many inorganic elements are so stable that they will not meaningfully degrade)[6,19] and can be considered legacy contaminants. Heavy metals can be introduced to the environment by anthropogenic activities including industries (e.g., mining) and pollution and will persist in the environment very effectively. PAHs are formed in natural processes and created or released to the environment through anthropogenic means such as fossil fuel extraction and incomplete combustion.[18] Both contaminant classes have been relatively well-studied compared to 'newer', emerging contaminants.

Contaminants of emerging concern are often accompanied with a greater paucity of data for their toxicity impacts and physicochemical properties relative to established, legacy contaminants. These include agrochemicals, pharmaceuticals, personal care products, plastics, and plastic additives.[7,10] In brief, these compounds are produced because they have useful applications. Surfactants such as perfluoroalkyl substances (PFAS) and nonylphenol are examples of useful compounds which have more recently drawn concern. PFAS, typically used for water-resistant applications,[8] are colloquially known as 'forever chemicals' because of their environmental persistence and show evidence of negative health impacts.[20,21] Like PFAS, nonylphenol is a compound with a myriad of industrial applications,[22] but has also been discovered to demonstrate endocrine disrupting effects.[23] In the early 2000s, nonylphenol was discovered to co-occur with another type of emerging contaminant, microplastics, as it found use as a plastic additive.[24]

Unlike the other pollutants discussed here, microplastics are solids which can cause physical health impacts such as blockages, damage, and reduced nutrient absorption when organisms mistake them for food items.[25] Plastics production increased in the 1940s,[26] and microplastics were first defined in 2004.[27] Microplastics are pieces of plastic size 1 μm–5 mm, and are termed nanoplastics when smaller (1–1000 nm).[28] Ultimately, smaller plastics are created when plastics are exposed to sun, oxygen, and physical abrasion.[29] Such weathering processes are inevitable when plastics are left in the environment, resulting in increased surface area and polar surface character,[29,30] altering the properties of this

pollutant. Microplastics may act as environmental vectors of chemical contaminants.[7,28] Because of the lighter density of most plastics relative to water, these co-occurring pollutants could have increased mobility.[10] Through processes of sorption and desorption, chemicals can bind reversibly or irreversibly to plastics, or leach from them.[2]

One key example of emerging concern for plastics leaching chemical pollutants arises from tire wear particles (TWPs) on roadways.[31] *Para*-phenylenediamine quinones (PPDQs) are derived from the ozonation of *para*-phenylenediamine (PPD) antiozonants added to tire rubber to sacrificially react with ozone.[31] The compound (*N*-(1,3-dimethylbutyl)-*N*'-phenyl-*p*-phenylenediamine-quinone (6PPDQ), was discovered in a recent 2020 landmark paper by Tian *et al.* to be the cause of mass deaths of coho salmon in the Pacific Northwest.[31] Since its initial discovery, 6PPDQ and analogous compounds have been identified and quantified in road dust, sediments, snowmelt, fish tissues, and other matrices.[32–36] The toxicity has been further studied for coho salmon, brook trout, rainbow trout, and other fish.[11,37,38] These additives and transformation product compounds leach from tire rubber into waterways, and the environmental and physicochemical behaviour of these compounds are still largely undefined.

The toxic or persistent aspect of different chemical pollutants cause them to be of concern to scientists, health officials, and different governments and industries.[15] To fully contextualize the scale and fate of pollution, accurate, precise, and sensitive chemical measurement is required. Analytical chemistry techniques can be applied to quantify the presence and abundance of chemicals in different environmental compartments (e.g., air, water, sediment, microplastics) and biological organisms (and the different tissues therein). Chemical partitioning in different environmental compartments can be further elucidated with physical chemistry techniques. These physicochemical properties can be used to improve computational modelling systems used to predict chemical distribution and transformation and toxicity mechanisms.[39–41] To back up lab-based studies, it is necessary to measure the distribution of chemical contaminants in real-world environmental samples. However, if the analytes are present, or worse toxic, in environmental samples at levels lower than the sensitivity of the applied analysis technique, they will not be measured. This information can and must be accessed with sensitive and selective analytical instrumentation.

1.2 Measurement and analysis

To measure the concentration of a chemical in a sample, an appropriate analytical technique must be selected. Environmental samples are complex, containing mixtures of analytes at broad ranges of concentrations and additional matrix components (e.g., salts, dissolved organic material, sediments) which may interfere with a measurement. Different instrumental techniques are well-suited to different contaminant classes (e.g., polar or nonpolar organic contaminants, metals) with differing levels of selectivity and sensitivity. No single analytical instrument is a universal analyzer capable of measuring all pollutants. Techniques such as Inductively Coupled Plasma Optical Emission Spectroscopy (ICP-OES) can be applied for trace elemental analysis, while most organic contaminants can be measured sensitively with some form of gas chromatography mass spectrometry (GC-MS)

or liquid chromatography mass spectrometry (LC-MS). These techniques are sensitive and selective, but under certain circumstances alternative approaches like direct analysis with mass spectrometry can be applied with equal efficacy or unique benefits.[42,43]

To quantify the concentration of metals, a conventional approach involves an inductively coupled plasma (ICP) torch.[42] The ICP torch is used to atomize and ionize the elements present in a sample, and different detectors can then be used to identify and quantify the elements present. ICP can be coupled to mass spectrometry (ICP-MS) or optical emission spectroscopy instrumentation (ICP-OES). For ICP-MS, ions formed in the plasma can be directed to a mass spectrometer where they are analyzed based on their mass-to-charge ratio (m/z). ICP-OES measures light intensity at element-specific emission wavelengths. Atoms in the plasma can become electronically excited. After excitation, electrons return to a lower energy state, and emit photons of wavelengths that are specific to the energy differences between the electronic levels. ICP-OES allows the intensity of the emission at each wavelength to be quantified. The specificity is somewhat lower in ICP-OES compared to ICP-MS as metals may share the same or similar emission wavelengths for some electronic transitions and ICP-MS also has the added advantages of higher sensitivities, larger linear dynamic ranges, and the ability to distinguish elemental isotopes.[42,44] However, the sensitivity and selectivity offered by ICP-OES makes the approach well-suited for many analyses and emission wavelengths can be chosen that maximize sensitivity and minimize interferences in analysis.[42]

In analytical chemistry, mass spectrometric techniques are often favoured over spectroscopic techniques because of the sensitivity, selectivity, and precision that mass spectrometry (MS) offers. To be detected with MS, a molecule must first be ionized. Every molecule has mass (m) and, when ionized, they are given a charge (z). MS measures analytes by their m/z ratio which can help elucidate the identity of a molecule. Prior to MS analysis, molecules typically undergo separation via chromatography, then the separated molecules are ionized in the mass spectrometer's ionization source. These ions are sorted by their m/z by the mass analyzer, and finally measured by the detector. In chromatographic separation, the time it takes for an analyte to elute through the chromatography column (the retention time) is based on the properties (e.g., size, hydrophobicity/hydrophilicity, vapour pressure) specific to that analyte which govern its affinity for the stationary (column material) and mobile (gas or solvent) phases.[43] Unique compounds with identical m/z ratios can be discriminated if their retention times differ.

For MS, the types of ionization sources are diverse, and different sources are better equipped to ionize different analytes based on their chemical structure. Electron ionization (EI) is a technique which can analyze both polar and nonpolar analytes. In EI, neutral gas-phase analytes are directed to an EI source where a controlled electron beam (typically 70 eV) strikes the molecules with the energy required to form a radical cation (**Equation 1.1**).[43] This approach has some advantages (e.g., the fragmentation patterns are reproducible which allows for reference library searches) but it is a hard ionization method which can result in complete fragmentation and no stable formation of the parent ion.[43]

$$M + e^- \rightarrow M^{+\bullet} + 2e^- \qquad \textbf{(Equation 1.1)}$$

EI is typically coupled to GC sample introduction as molecules must be in the gas phase to be ionized, but it can be coupled to LC methods in a process called liquid electron ionization (see **Figure 1.2.1A**).[45] The LEI interface uses a combination of low liquid flows, heat, and a co-axial gas flow to enable vaporization of the solvent and analyte molecules. These gas-phase compounds can then be directed towards the EI source for ionization (see **Figure 1.2.1B** for a simplified image of the LEI interface and an EI source).

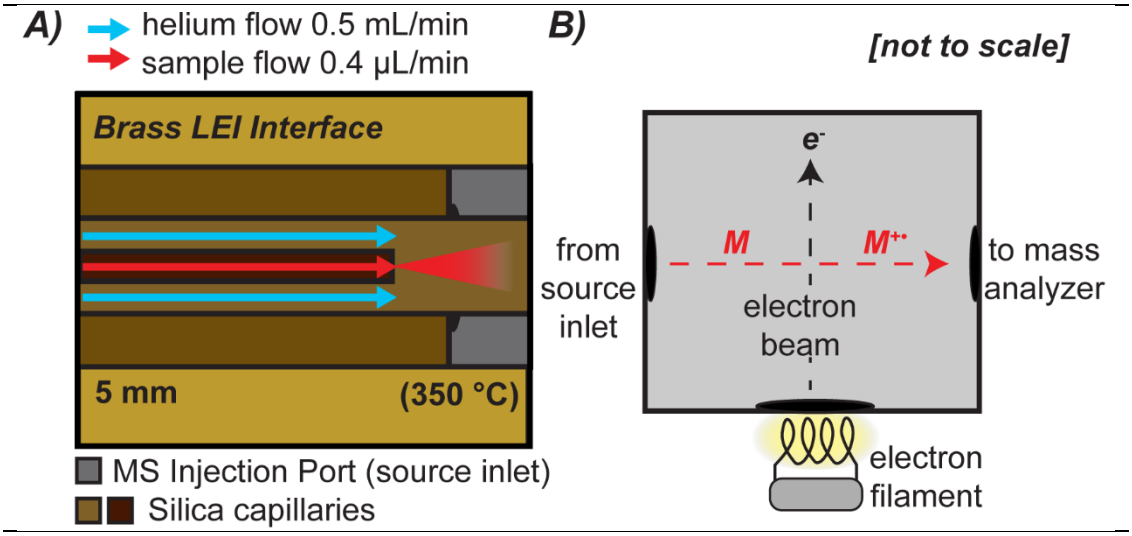

Figure 1.2.1. A) Liquid electron ionization (LEI) interface adapted from Vandergrift *et al.* [46] and simplified electron ionization (EI) source.

Chemical ionization (CI) applied in this thesis has a similar ionization source as EI with slightly altered geometry. Unlike EI, CI is a soft ionization technique which often results in a protonated or deprotonated parent molecular ion without extensive fragmentation. In CI, the electron beam ionizes a reagent [47] forming reagent ions which then ionize the analyte of interest by forming charged adducts or through proton-transfer reactions.[43,48] **Equations 1.2–1.3** show the example formation of the $CH_3OH^{+\bullet}$ and $CH_3OH_2{}^+$ reagent ions from methanol in the CI source, with **Equations 1.4–1.5** showing the probable mechanisms of formation for protonated molecular ions.

$$CH_3OH + e^- \rightarrow CH_3OH^{+\bullet} + 2e^- \quad \textbf{(Equation 1.2)}$$

$$CH_3OH^{+\bullet} + CH_3OH \rightarrow CH_3O^{\bullet} + CH_3OH_2{}^+ \quad \textbf{(Equation 1.3)}$$

$$CH_3OH_2{}^+ + M \rightarrow CH_3OH + [M+H]^+ \quad \textbf{(Equation 1.4)}$$

$$CH_3OH^{+\bullet} + M \rightarrow CH_3O^{\bullet} + [M+H]^+ \quad \textbf{(Equation 1.5)}$$

A third type of ionization is electrospray ionization (ESI), another soft ionization technique. This approach is extremely sensitive to pH-ionizable analytes as ionization is often achieved through protonation. However, ESI is rarely applied to nonpolar analytes as their ionization energy requirements are much greater than polar analytes which can be more easily be protonated, deprotonated, or form metal adducts.[43] In ESI, a voltage is

applied to a metal capillary through which solvent, in which the analyte is dissolved, is flowing. In the positive ionization mode illustrated in **Figure 1.2.2**, the applied electric potential results in a current flow which pulls electrons towards the electrode and away from solution. This oxidation reaction causes positive charge to build up at the tip of the solvent exiting the capillary. The buildup of charge forms a pointed Taylor cone (see **Figure 1.2.2**) because of the Coulombic repulsion between the positive ions. When the charge density reaches a critical level, a jet of solvent is formed which is attracted towards the source inlet. This jet breaks down, forming positively-charged droplets which further repel each other, breaking into smaller droplets as the solvent evaporates and the droplets become more unstable. The nebulized solution of ionized analytes are attracted to the ESI source inlet. There are multiple mechanisms of ionization at play in ESI, such as the ion evaporation model and charged-residue model.[43] In the ion evaporation model, the ion simply evaporates from the surface of the solvent droplet, while in the charged-residue model the solvent molecules evaporate while imparting a charge or multiple charges on the compound.[43,49] Which model acts dominantly depends on properties such as the presence of functional groups and the size, and thus relative volatility, of the analyte.[43]

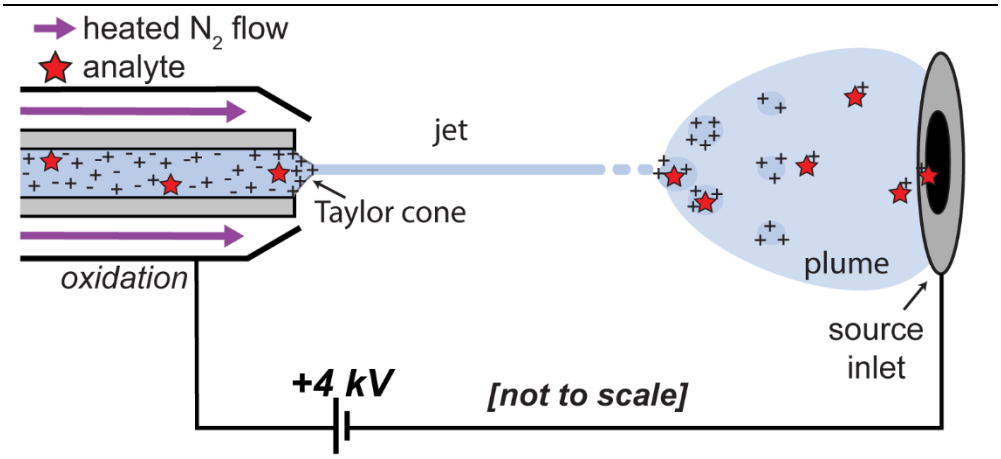

Figure 1.2.2. Simplified positive-mode electrospray ionization (ESI) mechanism.

In turn, ionization sources can be coupled to different mass analyzers with different levels of specificity and sensitivity. In this thesis, three types of mass analyzers were used: single quadrupole, triple quadrupole, and an Orbitrap high resolution mass spectrometry (HRMS) instrument. All mass analyzers control the movement of ions in some way, by carefully controlling and manipulating electromagnetic fields. A single quadrupole guides ions with defined *m/z* ratio to a MS detector. A quadrupole consists of four metal rods to which direct current and alternating radio frequency are applied (see **Figure 1.2.3A**).[43] Ions are attracted or repelled to the alternating charge applied to the quadrupoles, and thus can be manipulated across space to a detector. All ions can be passed through sequentially (this mode is termed a Full Scan), but if there is a specific analyte of interest, the current applied to the quadrupoles can be adjusted to only permit ions of a specific *m/z* to pass (termed a Selected Ion Monitoring (SIM) scanning mode).

A triple quadrupole uses three of these quadrupoles in series (see **Figure 1.2.3B**) and provides additional selectivity through tandem mass spectrometry (MS/MS). Ions of a defined *m/z* ratio are allowed to pass through the first quadrupole, then exposed to an inert gas (e.g., nitrogen) in the second quadrupole where collisions between ions and gas molecules result in smaller fragment progeny ions.[43] Finally, in the last quadrupole either fragments with specific *m/z* are passed through to the detector, or all fragment ions are passed. The reason why tandem mass spectrometry is useful is because it is possible for unique molecules to have the same initial *m/z*, but the way ions fragment is dependent on their chemical structure. Fewer molecules will have identical parent ion → progeny ion ($m/z \rightarrow m/z$) transitions. Full Scan and SIM mode are still possible with triple quadrupoles, but Selected Reaction Monitoring (SRM, monitors an ionic fragmentation pathway) and Multiple Reaction Monitoring (MRM, monitors at least two ionic fragmentation pathways) modes add additional specificity even when quadrupole mass analyzers only have unit mass resolution.

An Orbitrap mass analyzer has unique high specificity due to its high mass resolution. The electric field curvature of the Orbitrap is due to the complex shape of the electrodes (**Figure 1.2.3C**) and governs the movement of ions. The ions induce an image current on the outer electrodes as they move in complex patterns around the central electrode, and the axial oscillation of a given ion's motion (ω_z) can be converted to its *m/z*.[43] Due to the high precision of the *m/z* measurement, Orbitraps have high mass resolution much greater than the unit mass resolution of most quadrupole instruments. For example, the isotopic mass of one sulfur (31.972071 u) and two oxygens (31.98983 u) can be distinguished with the precision of HRMS, but not a typical quadrupole MS. The high specificity of HRMS allows for the discrimination of two ions with different chemical formulas but the same nominal mass, and also allows for the estimation of molecular formulas.

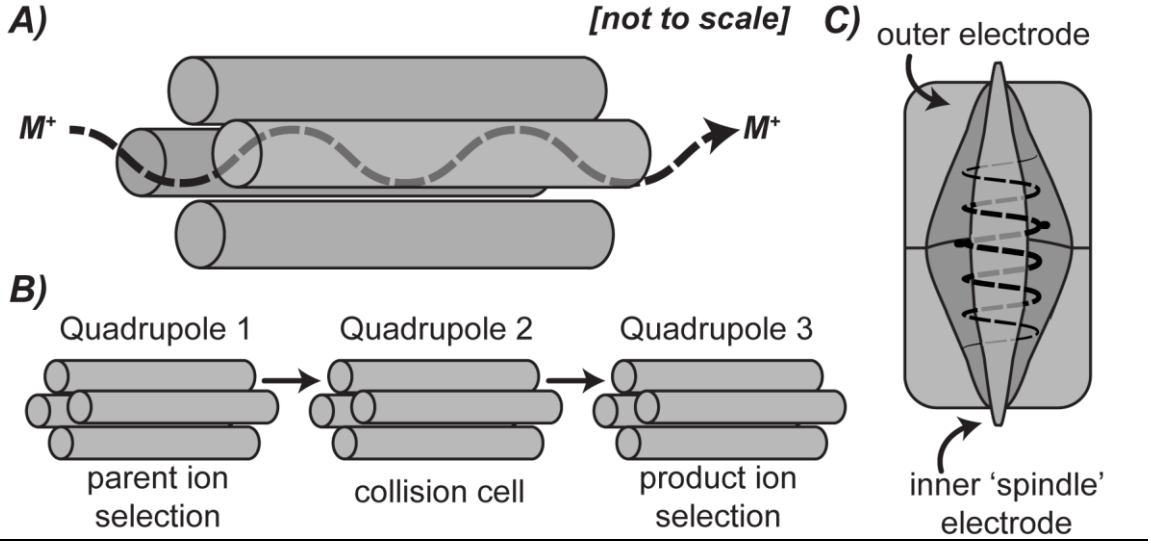

Figure 1.2.3. A) Single quadrupole B) triple quadrupole, and C) Orbitrap mass spectrometer. Example successful ion trajectory represented as a black dashed line.

Conventional applications of MS involve chromatographic separation such as LC or GC for quantitation of a contaminant. LC and GC-MS are the gold standard, especially when coupled to tandem mass spectrometry and/or high resolution mass spectrometry, as chromatographic separation results in strong evidence for the identity of a given analyte.[43] Direct analysis with mass spectrometry (DMS) is a form of MS which removes chromatographic separation and instead analytes are entrained to the mass spectrometer as a mixture. DMS provides a limitation as it does not readily discriminate isomers, though isomer differentiation is not always necessary and there are several advantages to DMS.

The DMS technique used in this thesis, and described in detail in **Chapter 2**, is condensed phase membrane introduction mass spectrometry (CP-MIMS). The greatest advantages of DMS comes down to shorter analysis time and lower cost per sample. **Figure 1.2.4** illustrates a comparison of example analysis workflow for the DMS technique CP-MIMS compared to conventional MS. CP-MIMS is impermeable to charged and undissolved matrix components, and consequently the sample clean-up required before measurement with conventional MS can be reduced or skipped. Consequently, samples with complicated matrices containing sediments, plastics, high salt or dissolved organic material concentrations, can be analyzed directly without extensive or expensive (time and supplies) work up. Without chromatographic separation, time per measurement is reduced dramatically, allowing for high throughput analysis. Finally, and most distinctively, CP-MIMS allows for continuous sample introduction to the ion source, resulting in real-time measurements that can capture dynamic processes within a sample.[50] To gain additional specificity, CP-MIMS can be coupled to different combinations of ion sources and mass analyzers. In this thesis, LEI and CI were used in **Chapter 2** and **Chapter 3** for the analysis of polycyclic aromatic hydrocarbons and nonylphenol with single and triple quadrupole mass analyzers. ESI was utilized in **Chapter 3** and **Chapter 4** for the analysis of *para*-phenylenediamine quinones, perfluorosulfonic acids, and perfluorocarboxylic acids with triple quadrupole and Orbitrap mass analyzers.

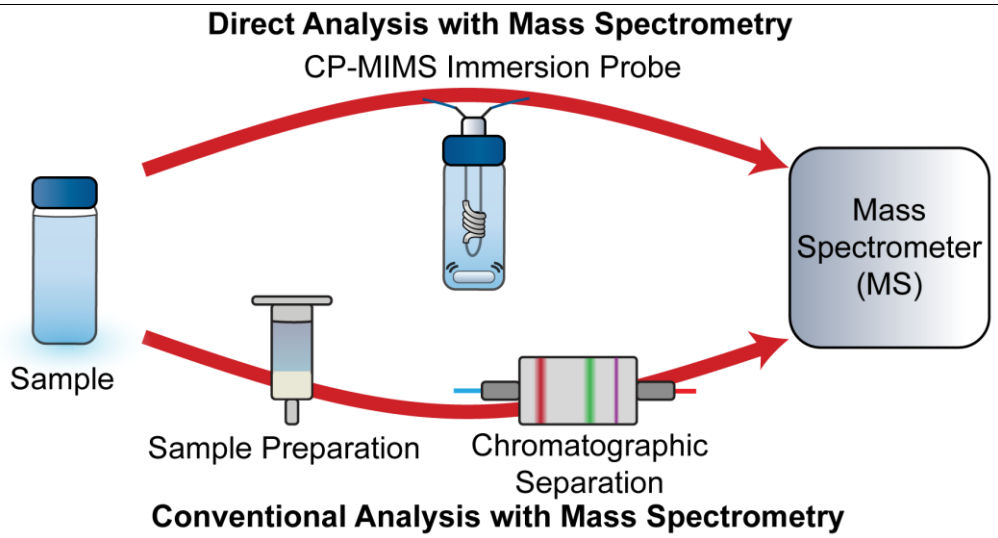

Figure 1.2.4. Example workflow of direct (top) and conventional (bottom) mass spectrometry sample analysis.

1.3 Description of work

This thesis investigates the fate and distribution of diverse contaminant classes while applying both conventional and non-conventional analytical approaches where appropriate. **Chapter 2** studied the interaction of two environmental contaminants: microplastics and trace levels of chemical contaminants. Here, the rate and extent of microplastic–contaminant sorption for trace level contaminants to microplastics was monitored in real-time using CP-MIMS-LEI/CI. Target contaminant (naphthalene, anthracene, pyrene, and nonylphenol) sorption behaviours were examined at nanomolar concentrations with four plastic types: low-density polyethylene (LDPE), high-density polyethylene (HDPE), polypropylene (PP), and polystyrene (PS). Under the conditions employed here, short-term sorption kinetics were assessed using on-line mass spectrometry for up to one hour. Subsequent sorption was followed by periodically measuring contaminant concentrations for up to three weeks. This work provided kinetic insights into surface interactions and describes a powerful experimental platform to directly observe contaminant sorption behaviours under a variety of environmentally relevant conditions. This work was further developed in **Chapter 3** by constructing sorption isotherms for the PAHs previously examined on LDPE, as well as including other analytes (such as PPDQs) and sorbents (such as sediments). The sorption and solubility of PPDQs were studied using CP-MIMS/MS-ESI.

In **Chapter 4**, the concentration of contaminants in a unique shark sample was studied. In 2019, a deceased 4 m long adult female bluntnose sixgill shark, pregnant with 72 pups, was recovered from Coles Bay on Vancouver Island, BC, Canada. This specimen provided a unique opportunity to examine maternal transfer of contaminants in an aplacental shark species. During preliminary work using CP-MIMS for analysis, it appeared that the matrix components interacted with the CP-MIMS membrane. More conventional methods with extensive sample cleanup were henceforward employed. Liver subsamples of the adult and offspring were analyzed for 18 targeted inorganic elements by inductively coupled plasma optical emission spectroscopy (ICP-OES) and 21 targeted perfluoroalkyl substances (PFAS) by liquid chromatography-electrospray ionization-high resolution mass spectrometry (LC-ESI-Orbitrap MS). The maternal transfer efficiencies in liver tissue were subsequently examined for both contaminant classes. Most metals were found to be higher in the mother compared to the offspring. Conversely, high maternal transfer efficiencies were observed for PFAS. This study highlighted the unique maternal transfer of PFAS in bluntnose sixgill sharks.

Chapter 2: Monitoring microplastic–contaminant sorption processes in real-time using membrane introduction mass spectrometry

Reproduced with minor changes and permission from Misha Zvekic (formal analysis, funding acquisition, investigation, methodology, visualization, writing the original draft, and review and editing), Greg W. Vandergrift (methodology, review and editing), Christine C. Tong (resources, supervision, review and editing), Chris G. Gill (resources, funding acquisition, review and editing), and Erik T. Krogh (conceptualization, formal analysis, funding acquisition, methodology, project administration, resources, supervision, review and editing) from *Environmental Science: Processes and Impacts*, "Monitoring microplastic–contaminant sorption processes in real-time using membrane introduction mass spectrometry" 2023, **25**, 1169. **DOI:** 10.1039/D3EM00083D.

2.1 Introduction

Microplastics have been observed in all environmental compartments and are a growing environmental concern.[51] They occur in a variety of material types and morphologies ranging from microfibers to plastics as large as 5 mm.[25] Microplastics can be transported great distances,[52] and have become globally ubiquitous.[53,54] Even if plastic production halted, levels of microplastics in the environment would continue to increase as plastics from a variety of consumer products and industrial processes fragment into smaller pieces due to environmental weathering.[55] The increased surface-area-to-volume ratio of micro- and nano-plastics compared to their larger counterparts provides more sites for adsorption.[25] The physical impacts of microplastics on organisms resulting from ingestion is of toxicological concern,[25] resulting in a combined, multi-stressor effects.[56,57]

Many classes of chemical contaminants have been observed to sorb to microplastics, including metals, antibiotics, polycyclic aromatic hydrocarbons (PAHs), and other persistent organic pollutants.[51,56,58–60] While the health and environmental impacts of trace contaminants sorbed to microplastics have not been fully characterized,[54] they may serve as an additional source and sink for contaminants, influencing their fate and distribution.[61] Characterizing chemical microplastic–contaminant sorption interactions can help answer emerging environmental and physiological questions about the behaviour and risks associated with microplastic pollutants.[61,62] Key knowledge gaps regarding microplastic sorption processes include the effect of environmental conditions (e.g., pH, salinity, and organic matter), weathering effects (e.g., photo-oxidation, fragmentation, and biofouling), and the effects of competitive sorption of multiple contaminants, particularly for less well-studied materials (e.g., tire particles).[28,63,64]

Sorption processes encompass both adsorption (the process of chemical sorbates adhering to the surface of the solid sorbent) and absorption (the process of sorbates permeating into the bulk volume of the sorbent).[65,66] The rate of sorption is expected to be first order in both the sorbate (aqueous contaminant) and the sorbent (plastic) (**Equation 2.1**)

$$Sorption\ Rate = k_{sorb}\ [free\ sorbent\ sites]\ [sorbate] \qquad \textbf{(Equation 2.1)}$$

where k_{sorb} represents the overall second order sorption rate constant (conc^{-1} time^{-1}) and the number of free sorbent sites is related to the number of sorption sites on the sorbent (conc), and [sorbate] represents the concentration of the contaminant of interest (conc). When either the sorbent or sorbate is present in considerable excess, the sorption behaviour can be described as pseudo first order, where k' is used to represent a pseudo first order rate constant (time^{-1}). While adsorptive and absorptive processes are occurring simultaneously, different sorption processes may occur over significantly different time scales (e.g., minutes vs weeks).[66] In such cases, the overall kinetics can be expressed as a summation (**Equation 2.2**). Such behaviour has been observed for sorption onto biochar with a fast sorption to the outer surface and a much slower diffusion into pore structures.[67]

$$k'_{\text{overall}} = k'_{\text{fast}} + k'_{\text{slow}} \qquad \textbf{(Equation 2.2)}$$

While most microplastic–contaminant sorption studies have been performed using pristine plastics,[51] environmental microplastics undergo significant chemical and physical transformation resulting from sun exposure and mechanical abrasion.[55] The changes induced by weathering processes, which include increased brittleness, fragmentation, and surface oxidation, may impact their sorption behaviour.[68] For example, photo-oxidation leads to the introduction of more polar hydroxyl and carbonyl groups,[29] which may decrease sorption for hydrophobic microplastic–contaminant pairs.[69] Conversely, increases in the hydrophilic character of plastics may lead to additional interactions for polar or charged contaminants through hydrogen-bonding or electrostatic interactions.[70] It should be noted that hydrophobicity is not the only factor that influences sorption behaviour.[71] Systematic comparisons of sorption across different microplastic–contaminant pairs as well as weathered and pristine plastics are challenging and represent an existing knowledge gap.[72]

Microplastic–contaminant sorption is conventionally characterized by a series off-line discrete samples collected over a range of concentrations. The resulting isotherms can be used to determine partition coefficients (K), which describe the thermodynamic sorption affinity between sorbate and sorbent at equilibrium.[68,73] Dynamic behaviour can be captured by collecting discrete samples over time and employed to describe kinetic parameters. These approaches are both time and labour intensive. Considering the multitude of potential contaminants, plastics, and environmental conditions, the use of a high throughput, on-line analytical method offers significant advantages. Condensed phase membrane introduction mass spectrometry (CP-MIMS) is one such method and can be used to monitor contaminant concentrations in real-time over time scales of minutes to hours.[74,75] A semi-permeable polydimethylsiloxane (PDMS) membrane separates the sample from a flowing solvent (acceptor) phase that is directly infused into a mass spectrometer. PDMS is permeable to hydrophobic analytes and impermeable to water, particulate matter, ions, and hydrophilic compounds.[76] This allows for the direct observation of the free aqueous solution phase concentration of contaminants in complex heterogeneous solutions. The technique has been coupled to electrospray ionization (ESI) which is well suited to measuring trace concentrations of organic amines[77] and carboxylic

acids.[78] CP-MIMS can also be coupled to liquid electron ionization (LEI) and liquid electron ionization/chemical ionization (LEI/CI) ion sources for analysis of non-polar compounds such as polycyclic aromatic hydrocarbons (PAHs).[46,47,79]

Presented here is the use of CP-MIMS with LEI to directly monitor the solution phase concentrations of three PAHs (naphthalene, anthracene, and pyrene) and nonylphenol in response to the addition of four different microplastic substrates (low- and high- density polyethylene, polystyrene, and polypropylene). The application of the experimental platform detailed here uniquely provides real-time kinetic sorption information for multiple contaminants at trace concentrations in complex solutions, and allows for longer-term sorption monitoring without requiring the separation of the plastics from solution or pre-concentration of analytes prior to measurement. Changes in contaminant concentrations were followed in real-time over the first hour and monitored intermittently thereafter over three weeks to characterize the rate and extent of sorption processes. Additionally, low-density polyethylene was photochemically aged by ultraviolet light to investigate the impact of photo-oxidation upon sorption behaviour.

2.2 Material and Methods

2.2.1 Sorbate chemical contaminant solutions

Naphthalene (99%), pyrene (98%), and nonylphenol (97%) were obtained from Sigma Aldrich (Oakville, ON, CAN). Anthracene (99%) was obtained from Alfa Aesar (Ward Hill, MA, USA). A multi-component stock solution was prepared in HPLC-grade methanol (VWR International, Edmonton, AB, CAN). This combined stock solution was used to prepare aqueous solutions in the low ppb range in deionized (DI) water (18 MΩ-cm, Facility Scale Reverse Osmosis/Ion Exchange Water Purification System, Applied Membranes Inc., Vista, CA, USA). Aqueous solutions contained less than 0.2% *v/v* methanol co-solvent and were slightly acidic (pH ~5) as measured with a benchtop pH meter (Accumet Fisherbrand™ AE150, Fisher Scientific, Toronto, ON, CAN).

2.2.2 Microplastic pellet sorbents

Low-density polyethylene (LDPE), high-density polyethylene (HDPE), isotactic polypropylene (PP), and polystyrene (PS) pellets (nurdles) were obtained from Sigma-Aldrich (Saint Louis, MO, USA). Additional information including physical characteristics are included in **Table 2.5.1** and **Table 2.5.2**. Prior to analyte sorption experiments, the pellets were soaked in methanol overnight and air-dried for about a week. Fresh, clean pellets were used in each experiment to minimize potential confounding effects caused by contamination or insufficient cleaning.

2.2.3 Photochemical ageing of LDPE pellets

LDPE pellets were aged in controlled conditions using ultraviolet (UV) light to investigate the impact of photochemical ageing on sorption. The intensity and wavelength distribution of two UV light sources have been described previously in comparison to

natural sunlight.[29] For the UV-C ageing treatment, pellets were placed on a tray and irradiated in a Rayonet© reactor (Southern New England Ultraviolet Company, Branford, CT, USA) with eight mercury vapour lamps (RPR-2537°A, Southern New England Ultraviolet Company) for 214 hours (9 days). For the UV-B ageing treatment, the pellets were exposed to Reptile UVB 150 Exo Terra® Bulbs (26 W PT2189, Rolf C. Hagen Inc., Montreal, QC, CAN) for a period of 169 days (~5 months). Pellets were aged at ambient temperatures (24–28 °C) in the laboratory, with periodic manual mixing to increase uniformity of the treatment. Attenuated Total Reflection Fourier Transform Infrared (ATR-FTIR) spectra were obtained periodically throughout the ageing process with a Nicolet iS5 FT-IR Spectrometer (Thermo Fisher Scientific, Madison, WI, USA) equipped with a Diamond crystal iD5 ATR accessory. A description of the surface changes due to photochemical ageing have been described elsewhere.[29]

2.2.4 Condensed phase membrane introduction mass spectrometry

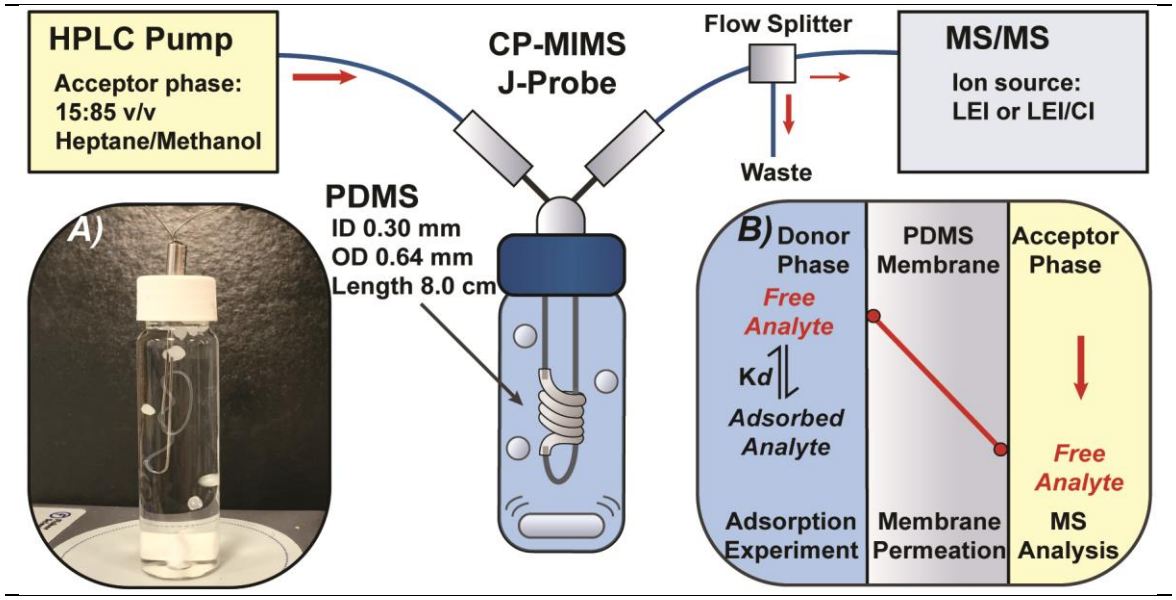

Figure 2.2.1. Schematic diagram of condensed phase membrane introduction mass spectrometry (CP-MIMS) with liquid electron ionization (LEI) or liquid electron ionization/chemical ionization (LEI/CI). Arrows show the direction of acceptor phase solvent flow. Inset A) shows a photograph of the CP-MIMS J-probe submerged in aqueous solution in the presence of plastic pellets. Inset B) shows the free analyte in the aqueous phase partitioning into and diffusing through the PDMS membrane whereupon it is dissolved in a flowing solvent acceptor phase and transported to a mass spectrometer

The concentration of contaminants in aqueous solution were monitored in real-time using a semi-permeable CP-MIMS membrane immersion probe (J-Probe) mounted into a Teflon-backed cap screwed onto the sample vial (**Figure 2.2.1**). The probe consisted of an 8.0 cm long, 170 µm thick (0.30 mm ID, 0.64 mm OD) hollow fibre polydimethylsiloxane (PDMS) membrane (Silastic brand, Dow Corning, Midland, MI, USA) mounted onto 22-gauge stainless-steel hypodermic tubing (0.33 mm ID; 0.64 mm OD) after swelling the

PDMS in heptane. An acceptor solvent phase consisting of 15:85 heptane/methanol (*v/v*) (HPLC-grade heptane, Fisher Chemical, Ottawa, ON, CAN) was continuously pumped through the lumen of the immersion probe at 50 µL min^{-1} with an HPLC pump (1100 series, Agilent Technologies Inc., Santa Clara, CA, USA). Post-membrane, the acceptor phase was split roughly 1:100 to waste by a passive flow-splitter comprised of a zero dead volume stainless-steel tee. The remaining nanoflow (400 nL min^{-1}) of acceptor phase was directed through the LEI capillary, volatilized, and delivered to a MS instrument. Two mass spectrometers were employed in this study due to instrument availability. For convenience, the triple quadrupole (7010B, Agilent Technologies, Santa Clara, CA, USA) equipped with a LEI/CI ion source was used to monitor the short-term kinetic experiments, and a single quadrupole (5975, Agilent Technologies) equipped with a LEI source was used for intermittent sampling during the longer-term sorption experiments. A detailed description of the CP-MIMS-LEI/CI interface has been described elsewhere.[46–48] The specific operational parameters for each mass spectrometer and minor modifications for the LEI/CI interface are detailed in **Table 2.5.3**. The selected ion monitoring *m/z* and MS/MS transitions used to measure the analytes by the two instruments are summarized in **Table 2.5.4** and **Table 2.5.5,** along with multi-point calibration parameters, demonstrating linear responses over the concentration ranges employed for this study.

2.2.5 Short-term chemical sorption monitoring with CP-MIMS

Short-term sorption monitoring experiments were carried out in 250 mL amber glass bottles containing 230 mL of an equimolar multi-component aqueous solution (170 nM naphthalene, anthracene, pyrene, and nonylphenol). The sample was stirred magnetically at 300 RPM with a Teflon-coated stir bar. The CP-MIMS probe was transferred from deionized (DI) water and inserted into the solution until 5 minutes of steady-state signal (S_0) was observed by a triple quadrupole MS with a LEI/CI interface as illustrated by the chronogram in **Figure 2.2.2A**. With the CP-MIMS membrane immersed in the solution, the screw cap lid was temporarily opened, and plastics were quickly added. Comparison experiments between types of plastics were conducted with approximately the same plastic surface areas (54 ± 2 cm^2) (**Table 2.5.2**). Given the different sizes of the plastic pellets, this corresponded to 100, 170, 127, and 120 pellets for LDPE, HDPE, PP, and PS, respectively. The MS signal chronograms (S_t) for each analyte were then monitored in real-time. After each experiment, the CP-MIMS probe was rinsed in pure methanol followed by immersion in DI water to prevent analyte carry-over and return signals to baseline levels (**Figure 2.2.2A**).

The MS signal traces were then background-subtracted, smoothed with a 10-point running boxcar, and normalized (**Figure 2.2.2B**) according to **Equation 2.3**

$$\text{Normalized MS Signal} = S_t/S_0 \qquad \textbf{(Equation 2.3)}$$

where S_t is the signal at time = t and S_0 is the initial signal at time = 0. The concentration at any time (C_t) was determined by scaling the initial concentration (C_0) by the normalized MS signal above. Initial rates were assessed over the first 10 minutes and are included in **Table**

2.5.6. Since all measurements were made within the linear calibration range, multi-point calibration curves obtained on the same day provided equivalent results (**Figure 2.5.1**).

First order rate constants (k'_{obs}) were determined from the slope of log transformed concentration data plotted versus time using the integrated rate expression (**Equation 2.4**). For short term kinetic studies, the data was typically fit over the first hour of sorption, which corresponds to *ca.* 1000 measured data points. Once first order kinetic behaviour was established, shorter experimental runs (e.g., 20 min) provided consistent results. The linearized data consistent with first order behaviour is given in **Figure 2.2.2C**.

$$\ln\left(\frac{S_t}{S_0}\right) = -k'_{\text{obs}}\, t \qquad \textbf{(Equation 2.4)}$$

Under the conditions employed here, a 10–30% drop in signal intensity was observed (depending on the analyte) during continuous monitoring for periods of 30–60 minutes (**Figure 2.5.2**), due in part to analyte depletion from mass transport across the membrane. The small systematic loss of analyte was corrected for with control experiments analyzed over the same time period without plastic pellet additions. First order rate constants for analyte depletion in the absence of plastics (k'_{loss}) are summarized in **Table 2.5.7,** based on triplicate control experiments. Sorption rate constants (k'_{sorb}) were then determined from **Equation 2.5** as the difference between the observed rate constant and the rate constant associated with loss due to other processes.

$$k'_{\text{sorb}} = k'_{\text{obs}} - k'_{\text{loss}} \qquad \textbf{(Equation 2.5)}$$

Control experiments were performed to compare short-term sorption rates at different initial analyte concentrations (**Figure 2.5.3**), sorption of analytes by themselves and in multi-contaminant solutions (**Figure 2.5.4**), pseudo-first order sorption kinetics at different initial analyte concentrations (**Figure 2.5.5**) and at different plastic loadings (**Figure 2.5.6**), and analyte depletion in different sample volumes (**Figure 2.5.7**).

2.2.6 Long-term chemical sorption monitoring with CP-MIMS

Long-term sorption experiments were completed in 40 mL glass vials capped with Teflon-backed septa containing 39 mL of aqueous solutions containing naphthalene, anthracene, pyrene, and nonylphenol. All analytes were equimolar (475 ± 5 nM) except anthracene (170 nM) due to its lower aqueous solubility limit.[9] Plastic pellets of LDPE, HDPE, PS, and PP were added with the same surface area of 9.1 ± 0.3 cm^2 corresponding to 17, 28, 22, or 21 pellets, respectively (**Table 2.5.1**, **Table 2.5.2**). Solutions were magnetically stirred at 500 RPM with a Teflon-coated stir bar at room temperature, shielding them from ambient light for a 3-week period, during which they were intermittently sampled (4–8 time points). Solution phase concentrations were determined by CP-MIMS-LEI utilizing a single quadrupole MS for *ca.* 5 minutes to obtain a steady state signal. All experiments using pristine plastics were made as triplicate sets, with each measured data point obtained using unique samples to eliminate the confounding influence of analyte depletion due to membrane transport. Control experiments with identical initial concentrations were conducted in parallel with vials containing no plastics to correct for

any analyte loss due to processes other than sorption to plastics, such as volatilization or adsorption to the vial.[80] Because of the limited supply of UV-B aged LDPE and the 5-month ageing time needed to produce them, these experiments were only made once per time point. These samples and the corresponding controls were filtered into a clean vial prior to measuring with CP-MIMS to avoid potential effects of small fragments adhering to the membrane probe.

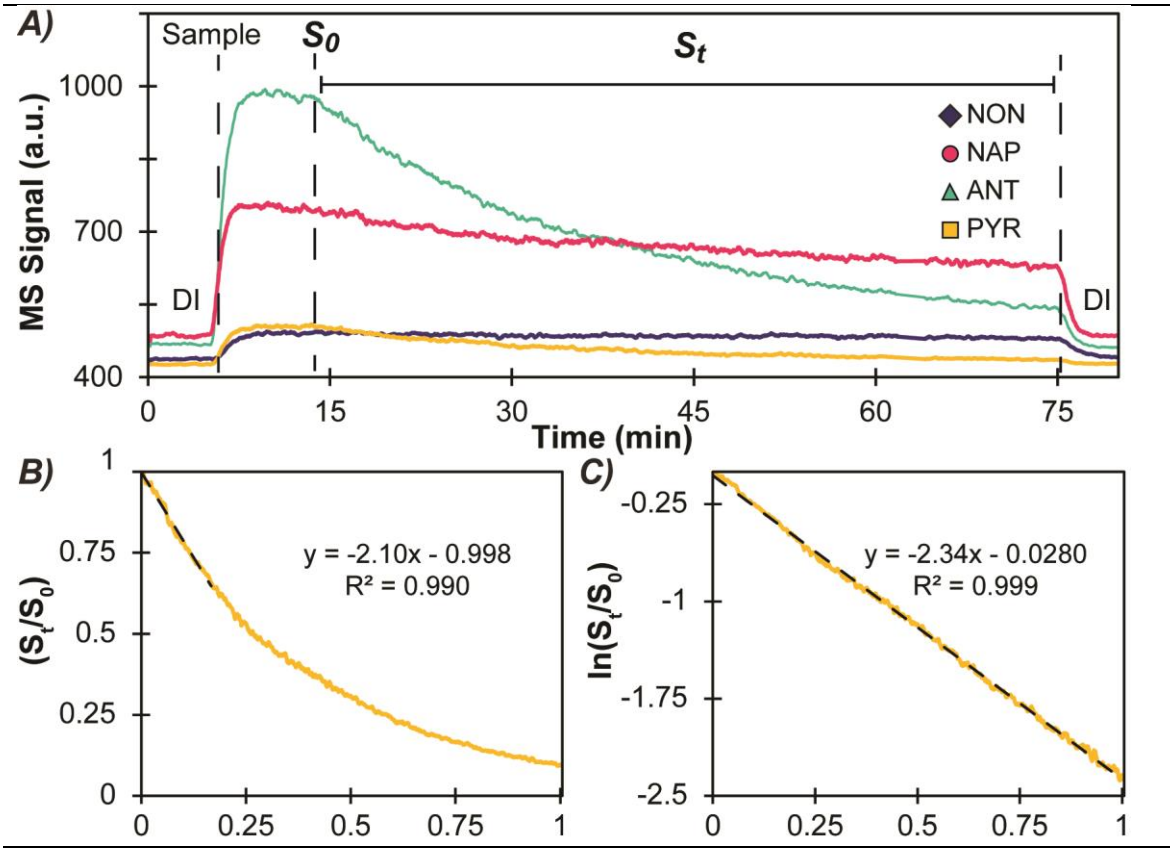

Figure 2.2.2. A) Signal chronogram of an experiment monitoring the sorption of four aqueous contaminants upon low-density polyethylene pellets. At t = 6 min, the probe was taken out of a DI blank and immersed in a combined standard solution containing equimolar contaminants (170 nM). At t=14 min, 100 pellets were added to the solution and sorption was monitored until t=75 min when the probe was returned to DI water. Sorption for anthracene is presented in B) as the processed normalized signal (S_t/S_0), and C) gives the natural log transformed signal (ln S_t/S_0), from which observed pseudo-first order rate constants (k'_{obs}) were determined from the slope of the best fit line.

The contaminant concentration remaining in solution relative to the control sample was expressed as $(S_t^{exp}/S_t^{ctrl}) \times 100\%$, where S_t^{exp} and S_t^{ctrl} are the baseline corrected, smoothed, steady-state signal chronogram levels for the experimental vials and control vials, respectively. The amount of contaminant in solution lost to sorption was then converted to a percent sorbed to plastic (**Equation 2.6**).

$$\text{Percent Analyte Sorbed} = (1 - (S_t^{\text{exp}}/S_t^{\text{ctrl}})) \times 100\% \qquad \textbf{(Equation 2.6)}$$

2.3 Results and Discussion

2.3.1 Microplastic–contaminant sorption monitoring

In this study, changes in the aqueous phase concentration of four contaminants are monitored over time in the presence of different types of pristine microplastics, one of which was also photochemically aged for comparison. Experiments were performed under comparable conditions of low sorbate concentration (nM) in the presence of excess sorbent (g L^{-1}), giving rise to pseudo-first order kinetic behaviour. Where possible, contaminants were examined at equimolar concentration with plastics at equal surface areas, making differences between contaminants and between different plastic types directly comparable. The plastic loading and concentration of the sorbate can be tuned to increase the initial sorption rates for convenience. The loading chosen here is based on the observable decrease in the solution phase concentration of PAHs on LDPE over the course of 60 min. The other plastics' loadings were matched to an equivalent surface area so that the kinetic trends could be directly compared. Higher microplastic loadings do not affect the trends in rate constants as demonstrated in **Figure 2.5.6**. In addition to nonylphenol, a structurally-related homologous series of three PAHs were chosen for analysis to compare short-term kinetic behaviour. All first order rate constants discussed below are conditional upon the experimental parameters employed. The following discussion is structured to examine both the short-term (hours) and long-term (weeks) sorption behaviours upon pristine, non-aged plastics. The effect of photochemical ageing on sorption to LDPE is subsequently discussed.

2.3.2 Short-term sorption kinetics

Initial sorption rates (μM h^{-1}) over the first ten minutes were observed to depend on the initial concentration of the sorbate (**Figure 2.5.3**) and the amount of plastic sorbent present consistent with the rate law (**Equation 2.1**). The log transformed decay curves illustrated pseudo-first order kinetic behaviour under the conditions employed here (**Figure 2.2.2**). The situations under which pseudo-first order kinetics may occur include when the initial concentration of sorbate is in vast excess compared to the limited number of binding sites (ϕ), as well as the conditions employed here where the number of binding sites were in excess and consequently remain invariant.[81] The corresponding rate constants (k'_{obs}) were determined from the linearized plots for each of the chemical microplastic–contaminant combinations. Control experiments run with individual contaminants demonstrated that sorption kinetics were not impacted by the presence of multiple analytes under the described conditions (**Figure 2.5.4**). The observed rate constants (k'_{obs}) were independent of initial sorbate concentrations (**Figure 2.5.5**) but do depend on the amount of microplastics added (**Figure 2.5.6**). For consistency, all subsequent experiments were carried out at equimolar contaminant concentrations and equal surface area plastic loading. **Figure 2.3.1** illustrates the observed first order kinetic behaviour of each sorbate (naphthalene, anthracene, pyrene, and nonylphenol) on LDPE in

panel A, and the kinetic behaviour of pyrene sorption on each of pristine plastics (LDPE, HDPE, PS, and PP) in panel B.

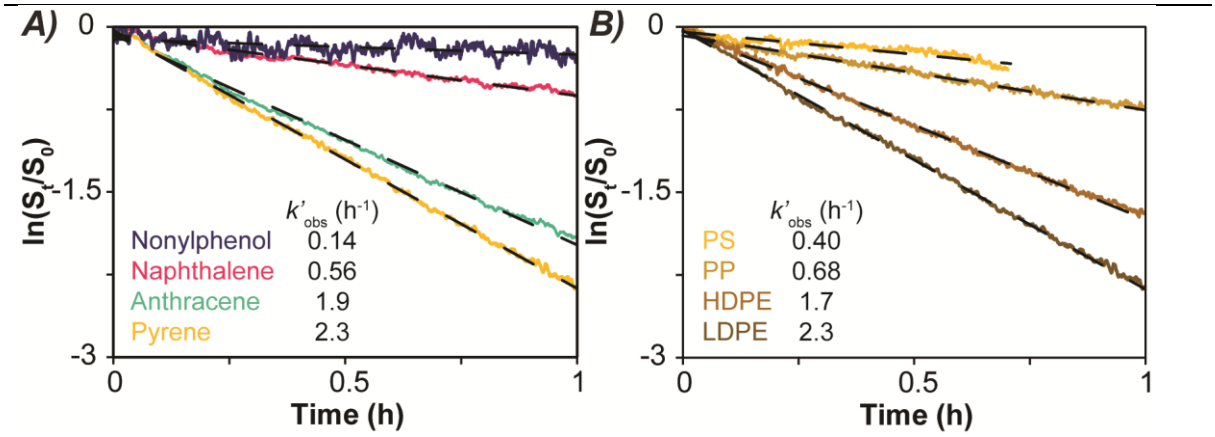

Figure 2.3.1. A) Observed first order kinetic sorption traces of naphthalene, anthracene, pyrene, and nonylphenol upon LDPE pellets, and B) pyrene on LDPE, HDPE, PP, and PS pellets. All target analytes were at equimolar concentrations (175 ± 5 nM) and all plastics were present at equivalent surface area amounts (~54 ± 2 cm^2). First order rate constants observed (k'_{obs}) are included.

The process of continuously measuring sorption by CP-MIMS results in a small but measurable analyte depletion via mass transport across the sampling membrane. Over time, this can become significant depending on the sample volume, membrane permeability, and acceptor phase flow rate. This effect is more pronounced in the limit of small sample volumes (**Figure 2.5.7**), so these on-line sorption experiments were performed using larger (230 mL) samples in screw cap glass bottles using a triple quadrupole MS equipped with an LEI/CI interface that yielded higher sensitivity via MS/MS measurements. This reduces (but does not eliminate) analyte depletion effects, and the observed rate constants were corrected via control experiments where no sorbent was added (**Figure 2.5.2, Table 2.5.7**). The values for the short-term sorption rate constants (k'_{sorb}) are summarized in **Table 2.3.1**.

Table 2.3.1: First order rate constants for short term microplastic–contaminant sorption [a]

	k'_{sorb} ± sd (h^{-1})			
Plastic	Naphthalene	Anthracene	Pyrene	Nonylphenol
LDPE	0.5 ± 0.2	2.0 ± 0.2	2.2 ± 0.3	nd
HDPE	0.3 ± 0.1	1.6 ± 0.3	1.6 ± 0.3	nd
PS	nd	0.34 ± 0.09	0.41 ± 0.08	nd
PP	0.13 ± 0.08	0.26 ± 0.09	0.2 ± 0.1	nd
UV-C wLDPE	0.5 ± 0.1	2.0 ± 0.2	2.3 ± 0.3	1.0 ± 0.3

[a] All contaminant sorbates were equimolar at 175 ± 5 nM in the presence of excess plastic at constant surface area of 54 ± 2 cm^2. Where sd is standard deviation based on $n \geq 3$ and nd is non-detect. All kinetic studies presented were obtained using CP-MIMS-LEI/CI utilizing MS/MS (**Table 2.5.4**).

Several trends in the sorption rate constants are immediately observable and depicted graphically in **Figure 2.3.2A**. Nonylphenol shows no appreciable sorption to any of the pristine plastics over the initial hour of on-line monitoring. Secondly, the sorption rate constants for PAHs increase with their size and hydrophobic character as characterized by their octanol-water partition coefficient (K_{OW}). A linear free energy relationship between log K_{OW} and log k'_{sorb} is presented in **Figure 2.3.2B**. Naphthalene appears to sorb slower (2–5 fold) than anthracene and pyrene, which tend to sorb at similar rates (typically within 10–20%). The relative sorption rates among the sorbates investigated (pyrene ≥ anthracene > naphthalene ≥ nonylphenol) holds for all the pristine (non-aged) plastic types evaluated.

Contaminant sorption on different plastics typically followed the trend observed for pyrene (**Figure 2.3.1B**), with the PEs being 3 to 5-fold faster than PP and PS. LDPE consistently demonstrated faster sorption than HDPE for all three PAH contaminants. Although nonylphenol exhibited no appreciable sorption over the course of an hour to any of the pristine plastics studied here, it was observed to sorb significantly over a period of days and weeks (see below).

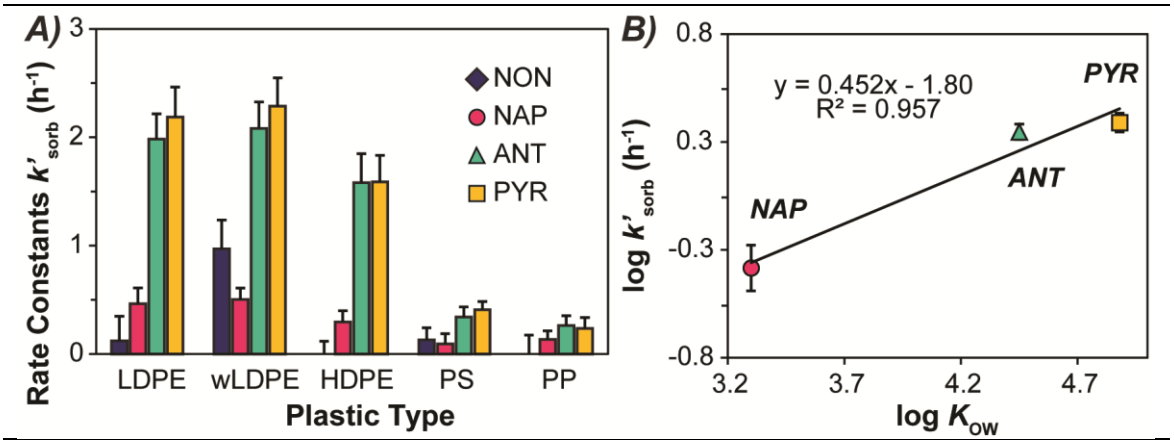

Figure 2.3.2. A) Pseudo-first order rate constants associated with the sorption of contaminants upon different microplastics (non-aged LDPE, HDPE, PS, PP, and UV-C aged LDPE (wLDPE)). B) Linear free energy relationship between the sorption rate constants onto non-aged LDPE and the hydrophobicity of PAHs.

Sorption interactions between plastics and non-polar chemical contaminants are thought to be driven primarily by hydrophobic interactions.[62,66] A linear free energy relationship was observed between log k'_{sorb} and log K_{OW} for the structurally related PAH series across all the pristine microplastics studied here (**Figure 2.5.8**). Nonylphenol was not expected to follow the trend depicted in **Figure 2.3.2B**, given the potential of hydrogen bonding interactions with both the aqueous solvent and the plastics. However, the relatively slow sorption behaviour for this compound was unexpected given its relatively hydrophobic character (log K_{OW} ~3.80–4.77).[82] Though others have observed a correlation, log K_{OW} has not always been observed to be a good predictor of sorption affinity.[83] This suggests that there are other factors at the microplastic–contaminant interface that may influence sorption kinetics.

2.3.3 Long-term sorption

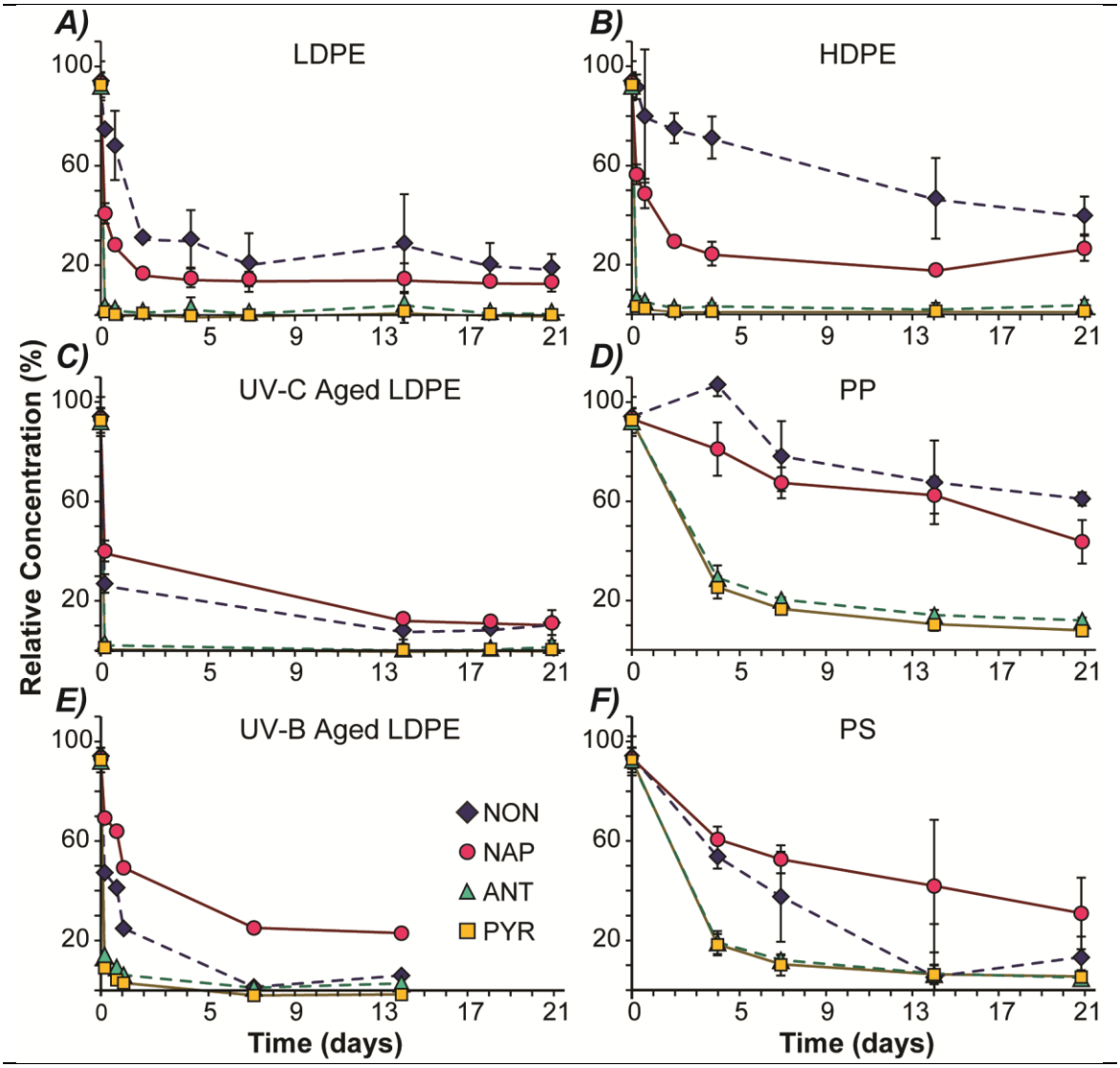

Figure 2.3.3. Percent aqueous concentration of nonylphenol (blue diamonds), naphthalene (red circles), anthracene (green triangles), and pyrene (yellow squares) to equivalent surface areas (8.8–9.4 cm^2) of LDPE, HDPE, PP, and PS microplastic pellets. Experiments for each time point were performed in replicate trials with error bars shown as standard deviation for n ≥ 3 (except for UV-B aged LDPE, n = 1). All concentrations were at 475 ± 5 nM except for anthracene which was at 170 nM.

Changes in aqueous contaminant concentrations were monitored over three weeks by intermittent sampling with CP-MIMS to follow slower processes and the extent of microplastic–contaminant sorption. In general, pyrene and anthracene sorbed the fastest and to the greatest extent on all plastics studied here and sorption to PEs reached equilibrium observably faster than to PP and PS (**Figure 2.3.3**). The extent of sorption of pyrene and anthracene to PEs was greater than 96% sorbed within two days. Naphthalene

sorption was slower than the more hydrophobic PAHs, requiring 3–5 days to reach equilibrium at 87% and 73% sorbed for LDPE and HDPE, respectively. These results are consistent with those reported by Wang *et al*., who observed the sorption trend of pyrene > anthracene > naphthalene upon LDPE.[73] Generally, nonylphenol demonstrated the slowest sorption, requiring two or three weeks in some cases, sorbing to a lesser extent than the PAHs ranging from 39–81% on PP, HDPE, LDPE. Sorption of nonylphenol on PS was anomalous because it sorbed faster and to a greater extent (90%) than naphthalene (70%), although both contaminants sorbed considerably slower than pyrene and anthracene. This suggests that there may be a unique surface interaction (such as pi-stacking) between nonylphenol and PS.[84] It is worth noting that the PS employed here has a density greater than water (**Table 2.5.1**) making it more susceptible to mechanical fragmentation by the magnetic stir bar used to continuously agitate the solution. A small amount of fragmentation was observed, though not characterized, and may have increased the surface area favouring adsorption processes. The use of a shaker table in place of mechanical stirring is recommended for future work. The extent of chemical sorption at three weeks as the percent of analyte sorbed to plastic is illustrated in **Figure 2.3.4** and summarized in **Table 2.5.8** for all microplastic–contaminant pairs.[73]

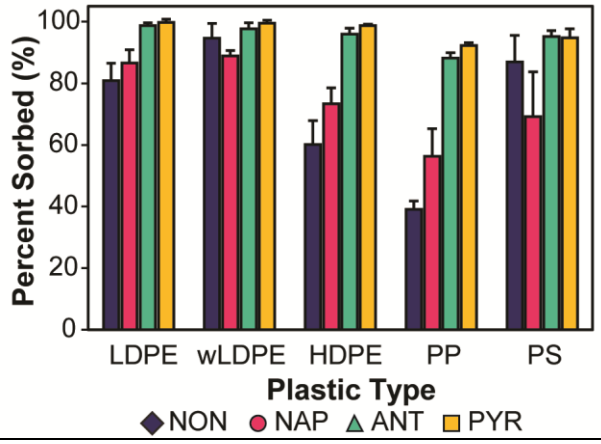

Figure 2.3.4. Percent of contaminant sorbed to equivalent surface areas (8.8–9.4 cm^2) of LDPE, UV-C aged LDPE (wLDPE), HDPE, PP, and PS microplastic pellets using **Equation 2.6**. Nonylphenol (blue), naphthalene (red), anthracene (green), and pyrene (yellow). All concentrations are at 475 ± 5 nM, except anthracene at 170 nM. Average of n ≥ 3, standard deviation represented by error bars.

In general, the extent to which contaminants sorbed correlated with their short-term sorption rates, although it is apparent that not all microplastic–contaminant pairs had fully equilibrated after three weeks (**Figure 2.3.3**). The presented results are broadly consistent with other reports indicating LDPE has a greater [80] or equivalent [65,69,85] sorption capacity than HDPE. The lower sorption to HPDE compared to LDPE observed in the presented data could be due to differences in microscopic surface areas, available plastic free volumes, or the greater crystallinity and density of HDPE relative to LDPE.[86] This group and others have found that the sorption capacity of PE was greater than that of PP.[69,87] There is some inconsistency in the literature regarding comparisons between PE

and PS, [63,69,73,84,88–90] which may in part be due to the differing prevalence of cross-linkages, porosity, and microscopic surface areas of different PS samples.[60] Given that the PS and isotactic PP used in this experiment are glassy,[65,91] it is likely that absorption processes are considerably lesser than in the more rubbery PEs because of their greater chain mobility and free volume. [84,92,93]

2.3.4 Sorption to aged LDPE

To examine the impact of photochemical ageing upon sorption, LDPE pellets were aged using two different UV light sources. The different light sources nominally described here as UV-B and UV-C have been previously characterized and used to examine photochemical aging rates via Attenuated Total Reflectance Fourier Transform Infrared (ATR-FTIR) spectroscopy.[29] While it is not expected that the ageing will affect sorption to all plastics in the same way, LDPE was chosen for this study because it was observed to demonstrate the most rapid sorption processes.

Nonylphenol was observed to sorb faster and to a greater extent on UV-C aged LDPE when compared to non-aged LDPE, while PAH sorption was largely unaffected by ageing (**Figure 2.3.2A, Figure 2.3.3**). The increased affinity of nonylphenol (**Figure 2.5.9**) is attributed to hydrogen-bonding interactions between oxidized functional groups (carbonyl and hydroxyl groups) on the aged plastic surfaces (**Figure 2.5.10**) and the hydroxyl group of nonylphenol. Hydrogen-bonding has been found to be a significant interaction between contaminants and plastics with polar functional groups [58,94,95] including weathered plastics.[70] The unchanged PAH sorption behaviours indicates that the increased number of hydroxyl and carbonyl moieties on the UV-C aged LDPE [29] either did not impede hydrophobic sorption or was compensated for by other processes. Surface cracking or fragmentation, for example, could increase available adsorption sites.[85] While, UV-B ageing conditions resulted in visible plastic fragmentation noted below, it did not appear to increase overall sorption.

UV-B ageing altered LDPE in two ways: it increased the brittleness of the plastic and also affected sorption behaviour. Mechanical stirring resulted in fragmentation of UV-B aged LDPE (**Figure 2.5.11**) into secondary microplastic particles due to its weakened integrity.[55,96] All PAH analytes appeared to sorb more slowly (**Figure 2.3.3**) to UV-B aged LDPE than both pristine and UV-C aged LDPE, suggesting a decreased sorption capacity. For example, the extent of naphthalene sorption was *ca.* 10% lower on UV-B treated LDPE. Nonylphenol, on the other hand, was observed to sorb to a slightly greater extent on UV-B aged LDPE as compared to UV-C aged LDPE. This is likely because the UV-B treated LDPE exhibited a greater surface oxidation than the UV-C treated LDPE as demonstrated in their ATR-FTIR spectra (**Figure 2.5.10**).

The increased brittleness [55] and decreased sorption capacity [69] is attributed to an increase in plastic crystallinity caused by UV-B ageing which is consistent with what has been observed by others.[55,67] Crystallinity increases during photochemical ageing due to cross-linkage reactions between polymer radicals [97] and is limited by the diffusion and mobility of radicals further into the plastic.[98] UV-C ageing occurred over the course of days,

while an equivalent amount of UV-B ageing requires months to achieve a similar state of oxidation.[29] Although not quantified here, the longer UV-B ageing time possibly led to increased crystallinity throughout the plastic. UV-C lamps are often used to rapidly age plastics for sorption studies,[83,85,99] but it is apparent that subtle, yet important, sorption behaviour changes either do not or have a limited time to occur under accelerated UV-C ageing.

2.3.5 Advantages and Limitations

This work presents the use of CP-MIMS as an *in situ* process monitoring strategy to follow sorption kinetics in real-time. The method has several advantages including the ability to monitor multiple trace organic analytes simultaneously in complex heterogeneous solutions without discrete sample collection, handling, pre-concentration, or chromatographic separation steps. Changes in solution phase concentrations in the presence of solid sorbents such as anthropogenic plastics and natural sediments can be rapidly assessed along with the effects of other sample conditions including salinity, pH, and high dissolved organic matter content. Continuous monitoring strategies are well-suited to processes that occur on a time scale of minutes to hours and can be employed to develop kinetic models with high temporal resolution (> 10^3 data points per hour). Slower sorption processes can be followed over longer time frames (days–months) by intermittently immersing the membrane into solution for a few minutes. The technique is limited to membrane-permeable neutral, hydrophobic analytes which can be resolved by distinct *m/z* parent ions and/or fragment ions with a mass spectrometer. Kinetics are limited to those which are slower than membrane transport kinetics, which depend on membrane thickness, acceptor phase composition, and diffusivity of specific analytes. The time constant for the analytes and conditions reported here range from 0.6 to 1.3 min^{-1} (see **Table 2.5.9**) and represent the upper limit of rate constants that can be measured.[100] For extended continuous monitoring applications, analyte depletion can be observed. This affect can be corrected using paired control samples without sorbent or minimized with experimental modifications such as larger sample volumes, smaller membrane geometries, and/or lower acceptor phase flow rates.

2.4 Conclusion

The simultaneous sorption of four chemical sorbates (naphthalene, anthracene, pyrene, and nonylphenol) on different plastic sorbents (LDPE, HDPE, PP, and PS) was investigated under comparable conditions using membrane introduction mass spectrometry to monitor aqueous solution phase concentrations over time. Short-term sorption kinetics were measured continuously over a one-hour period, with initial sorption of equimolar contaminants following the trend pyrene ≥ anthracene > naphthalene > nonylphenol on LDPE. The first order rate constants for pyrene and anthracene sorption were observed to be 5 times greater than naphthalene, while nonylphenol sorption too slow to detect on this time scale. The initial sorption for the PAH sorbates followed the trend of LDPE > HDPE > PS ≥ PP. Long-term sorption was measured periodically for up to three weeks, with the extent of sorption observed following similar trends to that observed in short-term kinetics experiments. LDPE was photochemically aged using UV light to

examine the impact of surface oxidation on sorption. Nonylphenol sorption increased whereas PAH sorption remained largely unaffected. This study represents the first use of direct analysis with mass spectrometry to monitor sorption processes in real-time at environmentally relevant analyte concentrations. Future work will investigate sorption on understudied plastics (including rubbers, fibers, and nanoplastics) and investigate changes in environmental conditions (salinity, pH, and dissolved organic matter), using the method described here and combining MIMS with conventional batch sorption experiments.

2.5 Supporting Information

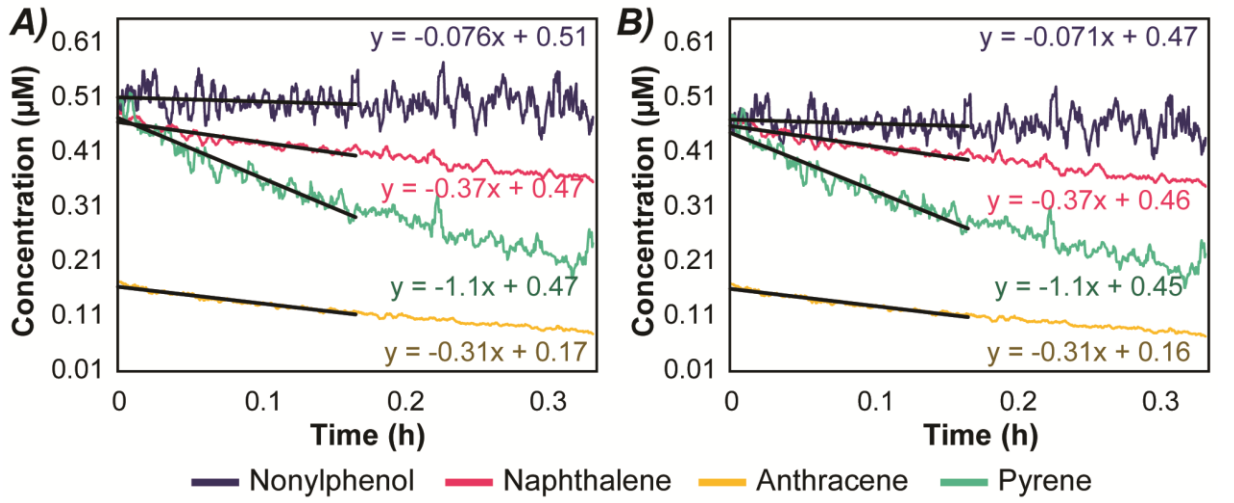

Figure 2.5.1. Initial sorption kinetics of four aqueous contaminants onto 100 LDPE pellets as determined by two different data treatments: A) converting the signal to concentration based on a five-point, same-day calibration curve, and B) normalizing the signal by the initial signal and multiplying the result by the known initial concentration, a one-point calibration curve. The initial concentrations of the analytes were 0.4776 μM naphthalene, 0.4687 μM pyrene, 0.4716 μM nonylphenol, and 0.1693 μM anthracene.

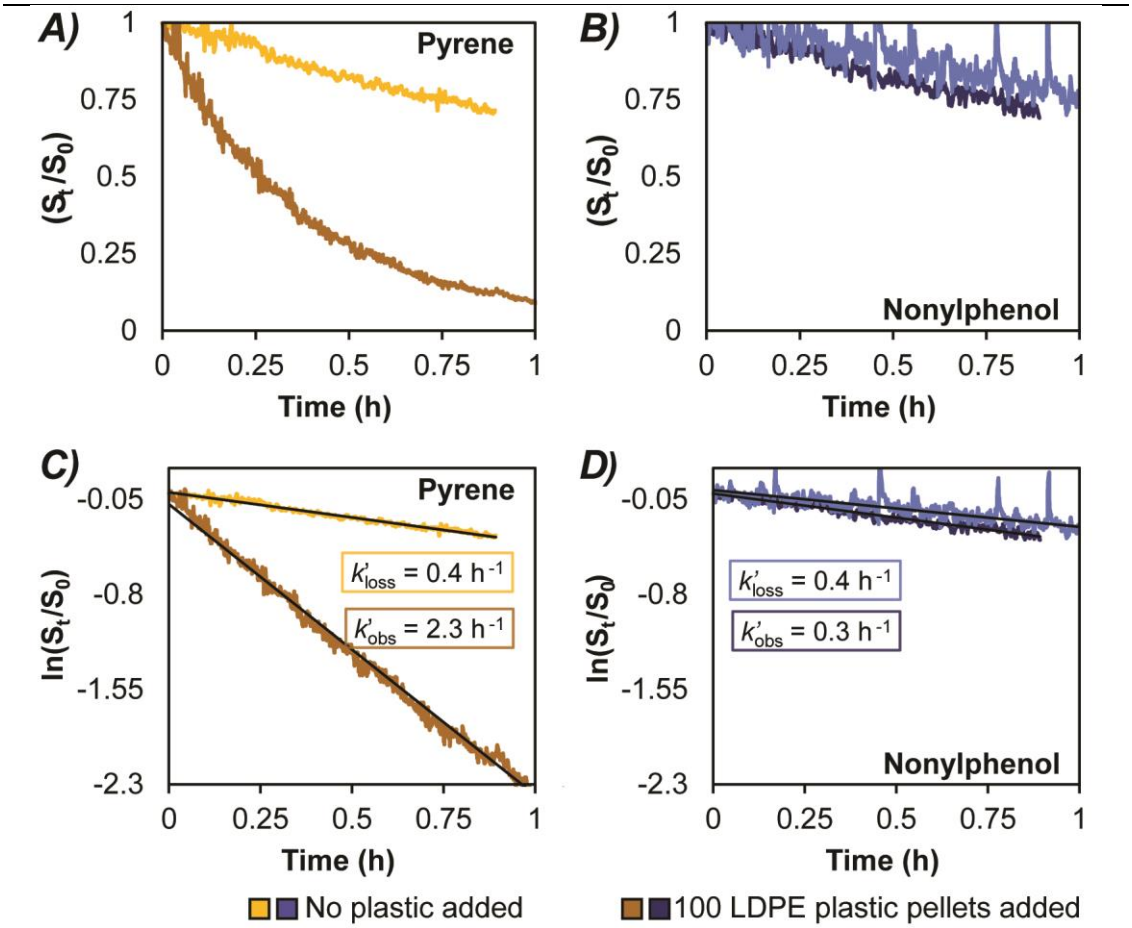

Figure 2.5.2. Comparison of analyte depletion (light colours) and sorption to LDPE (dark colours) for pyrene and nonylphenol. A) and B) shows normalized sorption for both analytes, while C) and D) shows the natural logarithm of the normalized signal. The pseudo-first order rate constants associated with each type of experiment are given. Rate constants shown here are for a single replicate (n = 1), while rate constants in **Table 2.3.1** are an average based on at least three replicates (n ≥ 3).

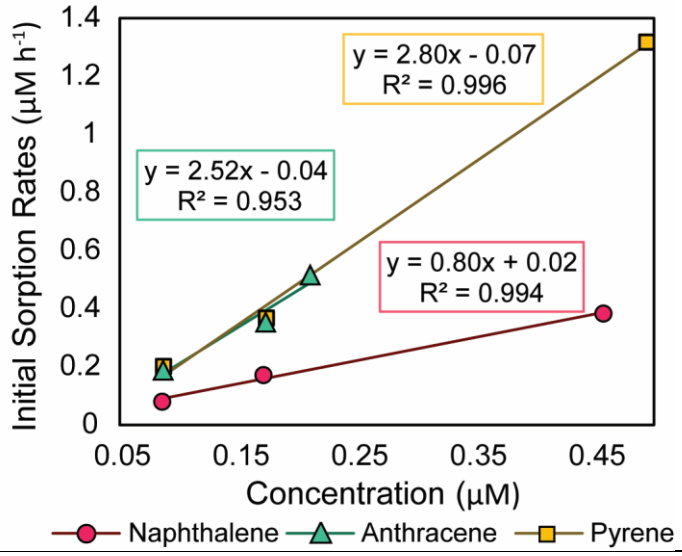

Figure 2.5.3. The sorption rates of analytes at different concentrations onto 100 LDPE. (n = 1 per experiment)

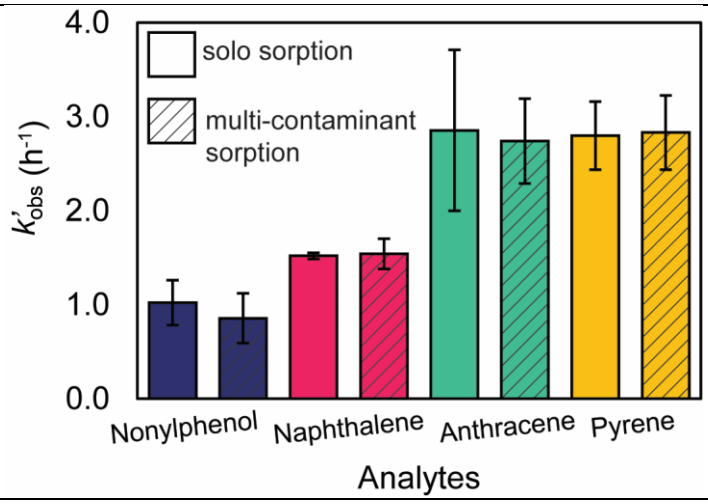

Figure 2.5.4. Initial sorption kinetics (k'_{obs}) onto 17 LDPE pellets of analytes undergoing solo sorption and sorption in the presence of the other three contaminants. Experiments were performed in triplicate, results shown as the average k'_{obs} with error bars showing the standard deviation. The sorption rate constants for the different experimental treatments were statistically non-significant.

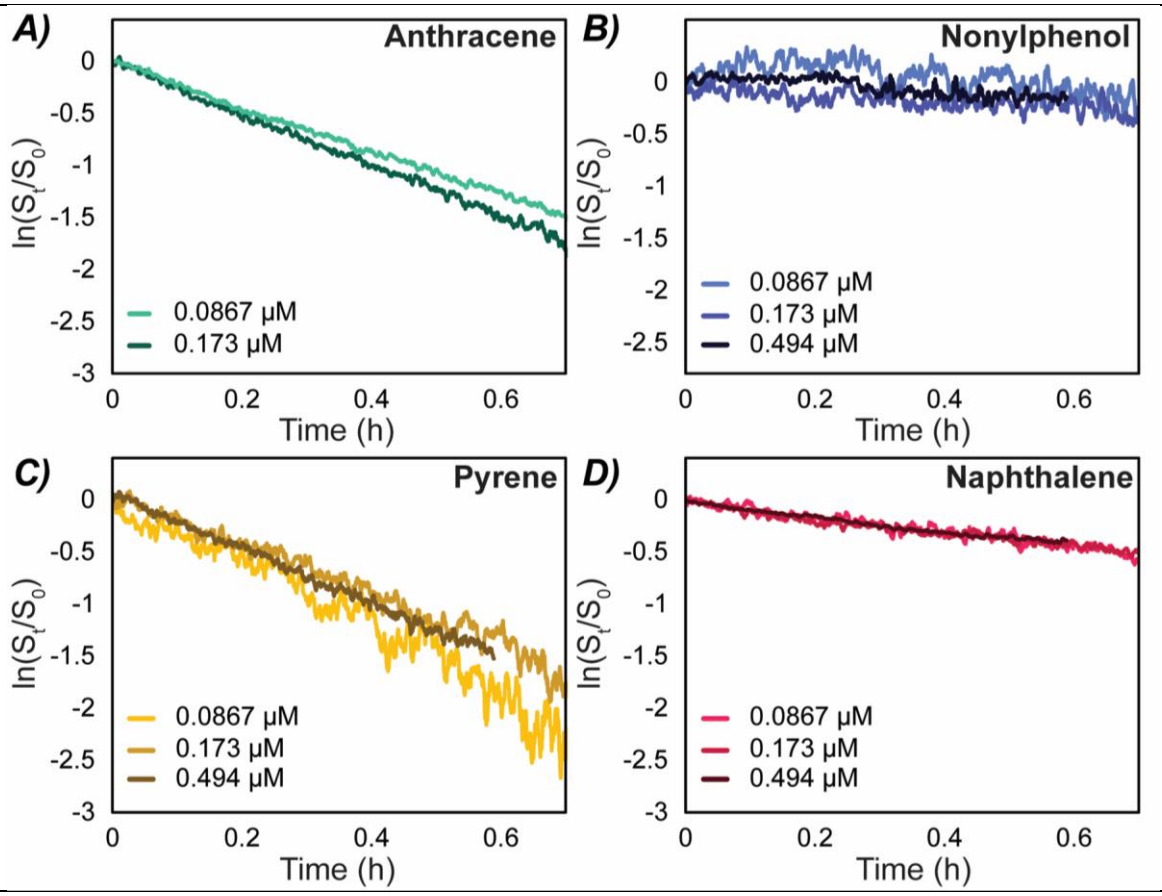

Figure 2.5.5. Linearized time dependent sorption onto 100 LDPE pellets for A) anthracene B) nonylphenol C) pyrene and D) naphthalene at different concentrations (0.09 µM light shade, 0.2 µM medium shade, 0.5 µM dark shade). (n = 1 per experiment)

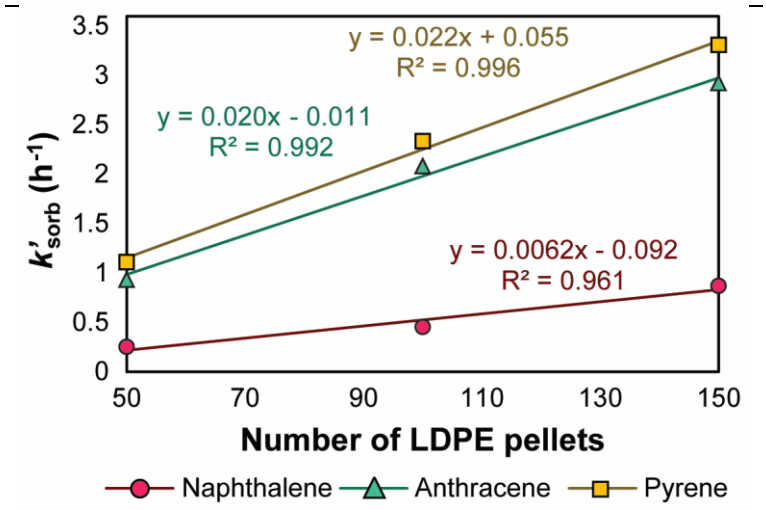

Figure 2.5.6. Initial sorption of analytes onto 50, 100, and 150 LDPE pellets. (n = 1 per experiment)

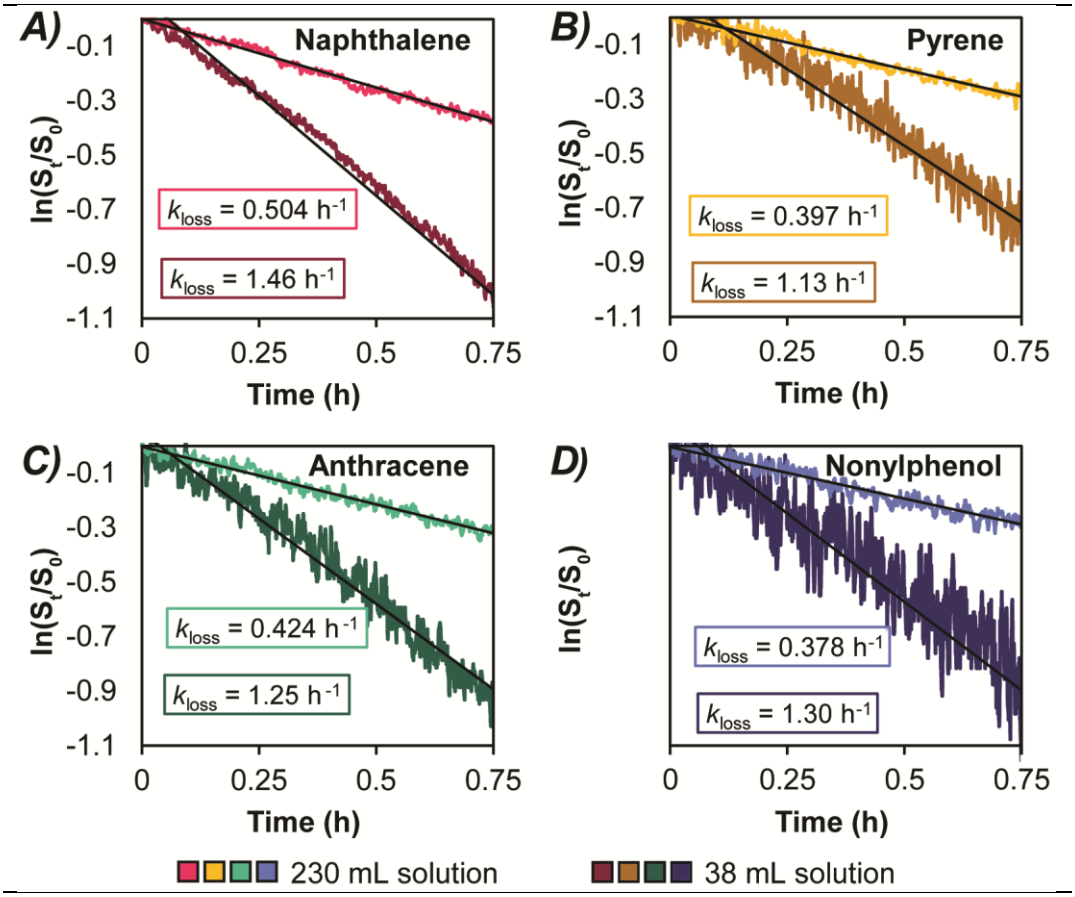

Figure 2.5.7. Comparison of analyte depletion for four analytes at the same initial concentration in the 40 mL vials used in long-term sorption experiments (dark colours) and the 250 mL vials used in short-term sorption experiments (light colours) (n = 1 for each type of experiment).

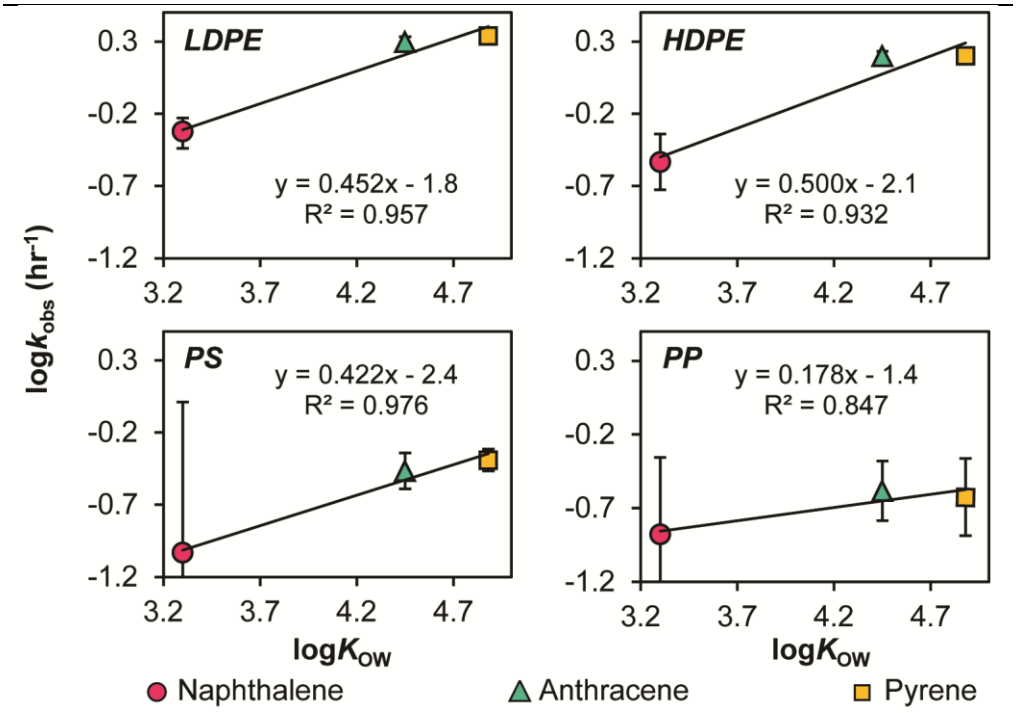

Figure 2.5.8. The relationship between the rate constants (k'_{obs}) of naphthalene, anthracene, and pyrene adsorbing onto LDPE, HDPE, PS, and PP and contaminant hydrophobicity (K_{OW}).

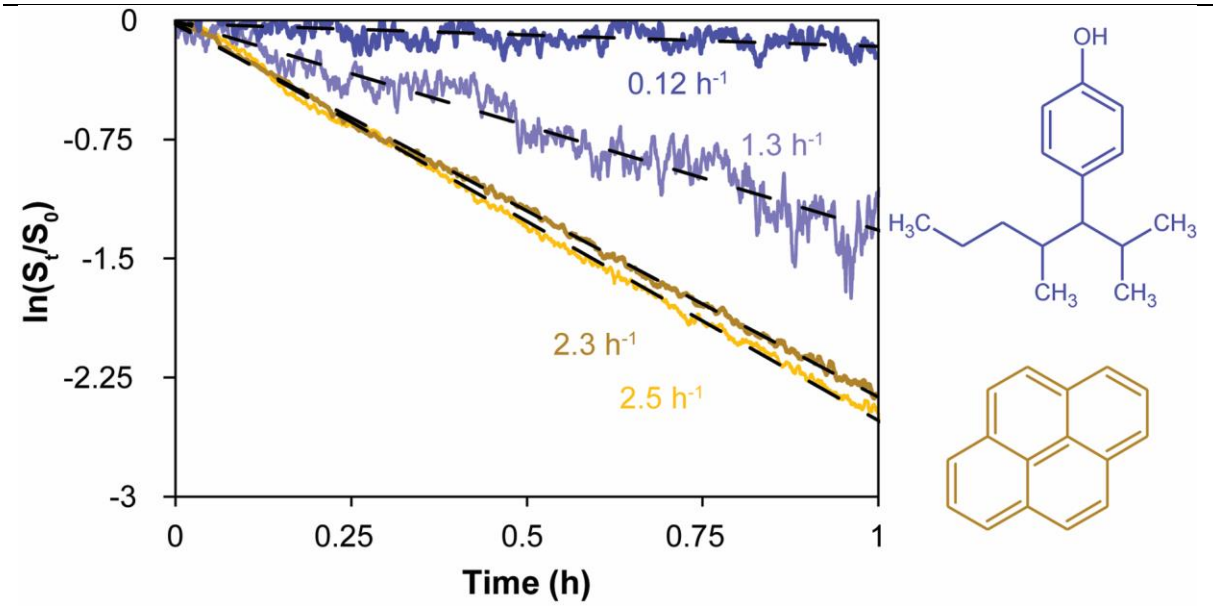

Figure 2.5.9. Comparison of nonylphenol (blue) and pyrene (yellow) sorption on non-aged (dark shade) and aged (light shade) LDPE. The observed rate constants (k'_{obs}) are included next to the sorption trace.

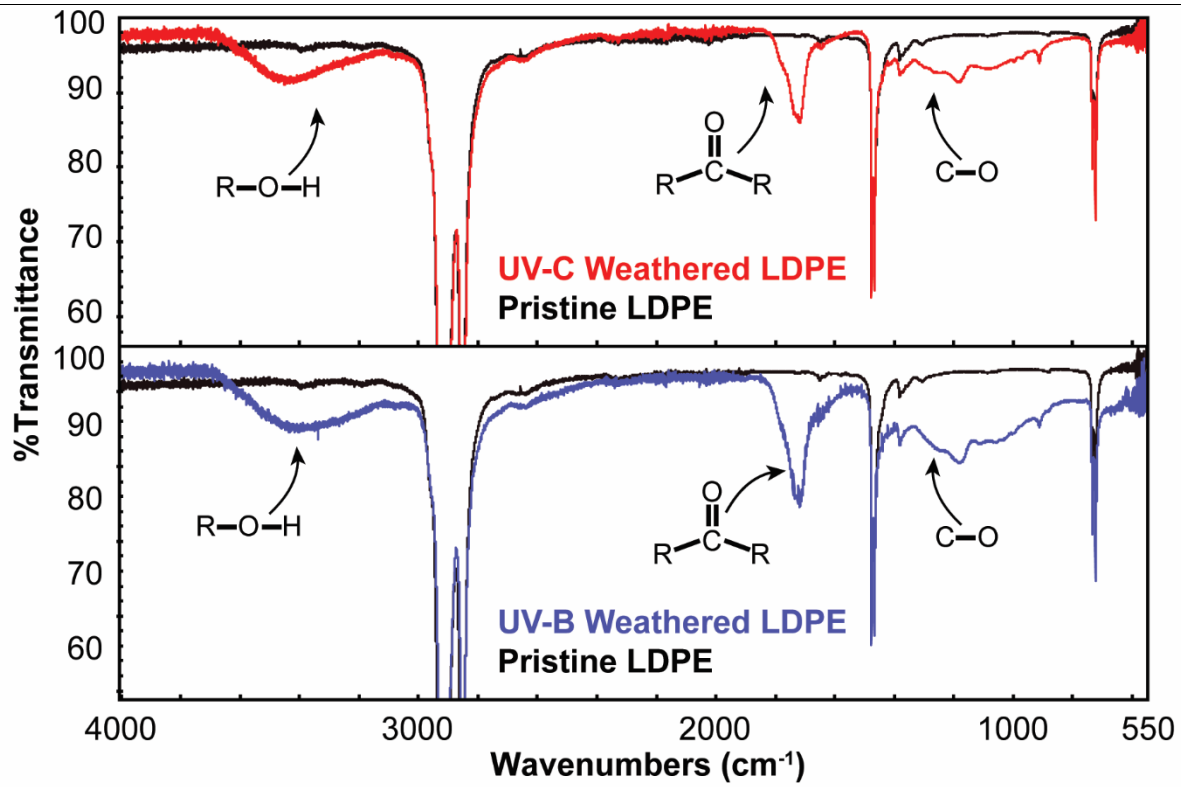

Figure 2.5.10. ATR-FTIR spectra of (top, red) UV-C aged (λ_{max} 254 nm, 8 days long), (bottom, blue) UV-B aged (λ_{max} 313 nm, 5.5 months long), and (black) pristine non-aged low-density polyethylene used in long-term sorption experiments. Spectra were taken with a Nicolet iS5 FT-IR Spectrometer with a Diamond crystal iD5 ATR accessory (Thermo Fisher Scientific, Madison, WI, USA). Using OMNIC 9.2.86 software, 16 scans were taken per measurement with a data spacing of 0.060 cm^{-1}.

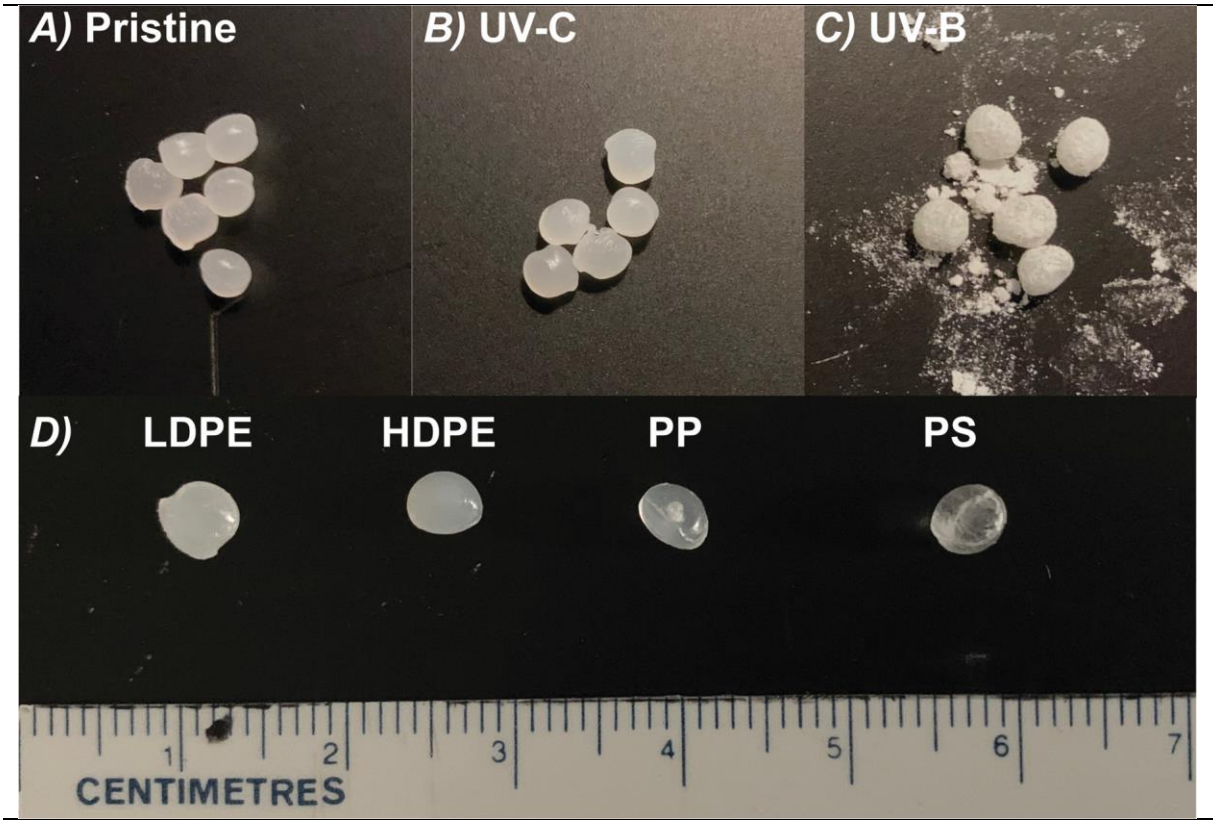

Figure 2.5.11. Photographs of LDPE pellets which were A) pristine B) aged beneath UV-C light for 8 days, and C) aged beneath UV-B light for 5.5 months. All pellets were stirred in solution for 21 days. Panel D shows all four pristine plastic nurdles (LDPE, HDPE, PP, and PS).

Table 2.5.1: Properties of plastic pellets

Plastic Type	Approximate Shape	Diameter (cm) [a] $\bar{x} \pm s$	Weight (g) [a] $\bar{x} \pm s$	Estimated Surface Area (cm^2)	Estimated Density (g mL^{-1}) [b] $\bar{x} \pm s$
Low-Density Polyethylene	Sphere	0.41 ± 0.18	0.03245 ± 0.002	0.54	0.927 ± 0.009
High-Density Polyethylene	Half-sphere	0.38 ± 0.11 0.17 ± 0.047	0.01394 ± 0.0006	0.16	0.94 ± 0.01
Polypropylene	Sphere	0.38 ± 0.010	0.02451 ± 0.0002	0.42	0.87 ± 0.01
Polystyrene	Sphere	0.38 ± 0.17	0.03288 ± 0.0003	0.45	1.049 ± 0.001

[a] n = 10 diameter, n = 3 weight, n = 3 density. Dimensions measured with a dial caliper (0.1 mm, Westward, Switzerland).
[b] density calculated gravimetrically by displacement of water. Manufacturer provided densities were 0.925 g mL^{-1} (0.9215–0.9255) for LDPE, and 0.9 g mL^{-1} for PP.

Table 2.5.2: Experiment details

Plastic Type	250 mL Short-Term Experiment [a]		40 mL Long-Term Experiment [a]	
	Pellets Used	Surface Area per Volume (cm^2 mL^{-1}) [b]	Pellets Used	Surface Area per Volume (cm^2 mL^{-1}) [b]
Low-Density Polyethylene	100	0.233	17	0.234
Polypropylene	127	0.232	22	0.237
Polystyrene	120	0.233	21	0.241
High-Density Polyethylene	170	0.233	28	0.226

[a] Solution volume in short and long-term experiments was 230 mL and 39 mL, respectively.
[b] e.g., 17 LDPE pellets and 39 mL of solution provided in an estimated 0.234 cm^2 mL^{-1} surface area per solution volume ratio, compared to a 0.233 cm^2 mL^{-1} ratio in the short-term experiment where 100 LDPE pellets were added to 230 mL of solution. This plastic/volume ratio was chosen based on the kinetic sorption experiments for LDPE.

Table 2.5.3: Operational parameters for the mass spectrometers [a]

Mass Spectrometer	Agilent Technologies 7010B GC/MS Triple Quad [b]	Agilent Technologies 5975 Inert Mass Selective Detector [b]
Gas Chromatograph [c]	Agilent Technologies 7890B GC System [b]	Agilent Technologies 6890N Network GC System [b]
Ion Source	High efficiency axial CI ion source [b]	EI inert 350 ion source [b]
Filament	Part number G3850-60021, utilizing a single coiled filament and the extractor plate removed [b]	Part number G7005-60061 [b]
Solvent Pump	Agilent 1100 series HPLC pump system [b]	Agilent 1100 series HPLC pump system [b]
Helium Flow (mL min^{-1})	0.5	1.0
Transfer Line Heater Temperature (°C)	400	350
Source Temperature (°C)	200	280
Quadrupole Temperature (°C)	Q1: 150, Q2: 150	150
Emission/Filament Current (μA)	50.0	34.6
Insertion Depth into Brass Nut (mm)	3	3
Capillary Liner Insertion Depth into Ion Source (mm)	2	2
Normal Operating Pressure (Torr)	1.40×10^{-4}	1.40×10^{-4}
Ionization Energy (eV)	70	70
Dwell Time (ms)	250 [d]	200
MS Mode	Multiple Reaction Monitoring (MRM)	Selective Ion Monitoring (SIM)

[a] For additional instrumental details see Vandergrift 2019.[48]
[b] Agilent Technologies Inc.; Santa Clara, CA, USA.
[c] Used to introduce helium (99.999% purity, Praxair, Mississauga, ON, CAN) and to heat the LEI/CI interface.
[d] Resolution of MS 1 and MS 2 set to 'wide'.

Table 2.5.4: Tandem mass spectrometry and analytical calibration data for the triple quad MS used for short-term sorption monitoring experiments [a]

Analyte	Precursor Ion → Progeny Ion [b] (*m/z*)	Collision Energy (eV)	Slope (µg L^{-1})	R^2	Concentration Range (µg L^{-1})		Detection Limit (µg L^{-1}) [c]
NAP	129 → 102	45	11.80	0.9845	10.96	58.64	1.0
	129 → 128	33	40.11	0.9828			0.49
ANT	179 → 152	50	18.53	0.9359	15.41	37.51	0.52
	179 → 178	37	81.85	0.9380			0.21
PYR	203 → 152	60	2.334	0.9861	17.54	99.90	2.1
	203 → 202	37	116.5	0.9859			0.40
NON	221 → 85	5	0.6722	0.9721	19.90	96.28	7.4
	221 → 71	5	1.210	0.9735			5.2

[a] 4 point calibration curve based on a multi-component solution in deionized water. 250 mL bottle, stirring at the 300 RPM on a CORNING PC-351 Hot Plate Stirrer.
[b] Molecular fragmentations depicted in bold were used here although no difference in the rate constants were observed using either transition.
[c] Detection Limit = 3 × standard deviation of blanks / calibration curve slope.

Table 2.5.5: Single quadrupole mass spectrometry and analytical calibration data for single quad MS used for long-term experiments [a]

Analyte	Selected Ion Monitoring (*m/z*)	Slope (μg L^{-1})	R^2	Concentration Range (μg L^{-1})		Detection Limit (μg L^{-1}) [b]
NAP	128	0.7902	0.9960	18.80	63.84	3.7
ANT	178	0.8784	0.9934	9.234	31.35	2.9
PYR	202	0.8978	0.9935	28.87	98.03	2.5
NON	107	0.1723	0.9935	31.44	106.7	19

[a] 5 point calibration curve based on a multi-component solution in deionized water. 40 mL vial, stirring at 500 RPM on Fisherbrand™ Ultra Thin Magnetic Stirrer (Fisher Scientific Cat #14-955-150). Long-term adsorption rates were stirred off line at 500 RPM on CORNING PC-351 Hot Plate Stirrer and Fisher Thermix® Stirring Hot Plate Model 210T stir plates.
[b] Detection Limit = 3 × standard deviation of blanks / calibration curve slope.

Table 2.5.6: Observed initial sorption rates (μM h^{-1}) over the first 10 minutes

Sorbate	0.1711 μM Naphthalene 129.0 → 102.0 *m/z*			0.1730 μM Anthracene 179.0 → 152.0 *m/z*			0.1735 μM Pyrene 203.0 → 152.0 *m/z*			0.1806 μM Nonylphenol 221.0 → 71.0 *m/z*		
Sorbent	Slope h^{-1}	Rate μM h^{-1}	RSD	Slope h^{-1}	Rate μM h^{-1}	RSD	Slope h^{-1}	Rate μM h^{-1}	RSD	Slope h^{-1}	Rate μM h^{-1}	RSD
LDPE (n = 4)	−0.96	0.16	3	−2.0	0.35	3	−2.2	0.38	4	−0.29	0.05	6
UV-C wLDPE (n = 3)	−0.98	0.17	10	−2.2	0.38	10	−2.2	0.38	22	−1.2	0.21	21
HDPE (n = 3)	−0.65	0.11	5	−1.7	0.29	9	−1.8	0.30	11	−0.19	0.03	7
PS (n = 3)	−0.35	0.06	5	−0.64	0.11	11	−1.0	0.18	10	−0.36	0.07	7
PP (n = 3)	−0.57	0.10	13	−0.61	0.11	15	−0.72	0.13	22	−0.61	0.11	30

Table 2.5.7: Observed pseudo-first order rate constants k'_{obs} (h^{-1})

Chemical Sorbate		0.1711 µM Naphthalene 129.0 → 102.0 *m/z*		0.1730 µM Anthracene 179.0 → 152.0 *m/z*		0.1735 µM Pyrene 203.0 → 152.0 *m/z*		0.1806 µM Nonylphenol 221.0 → 71.0 *m/z*	
Plastic Sorbent	n	Rate Constant (h^{-1})	RSD	Rate Constant (h^{-1})	RSD	Rate Constant (h^{-1})	RSD	Rate Constant (h^{-1})	RSD
Analyte Depletion (k_{loss})	3	0.23	29	0.22	38	0.21	36	0.13	69
LDPE (k_{obs})	4	0.69	19	2.2	10	2.4	11	0.25	84
UV-C wLDPE (k_{obs})	3	0.73	11	2.3	10	2.5	10	1.1	23
HDPE (k_{obs})	3	0.52	16	1.8	14	1.8	13	0.12	65
PS (k_{obs})	3	0.32	21	0.56	7	0.62	2	0.26	26
PP (k_{obs})	3	0.36	12	0.48	8	0.45	14	0.10	150

Table 2.5.8: Extent of chemical sorption to microplastics after three weeks [a]

Experiment		Percent of Analyte Sorbed to Pellets (%)			
Plastic Type	n	0.4776 µM Naphthalene	0.1693 µM Anthracene	0.4687 µM Pyrene	0.4716 µM Nonylphenol
		$\bar{x} \pm s$	$\bar{x} \pm s$	$\bar{x} \pm s$	$\bar{x} \pm s$
LDPE	8	87 ± 4	99 ± 1	100 ± 1	81 ± 5
UV-C wLDPE	3	89 ± 1	98 ± 2	100 ± 1	95 ± 5
HDPE	4	73 ± 5	96 ± 2	99 ± 1	60 ± 8
PP	3	56 ± 9	88 ± 1	92 ± 1	39 ± 3
PS	3	69 ± 14	95 ± 2	95 ± 3	87 ± 8

[a] Results represented as the mean and standard deviation of replicate experiments.

Table 2.5.9: Kinetic limit of analytes using the 8.0 cm membrane CP-MIMS J-Probe [a]

Analyte	Kinetic Limit (min^{-1}) $\bar{x} \pm s$	Kinetic Limit (h^{-1}) $\bar{x} \pm s$
Nonylphenol	0.65 ± 0.11	39 ± 6
Naphthalene	1.27 ± 0.05	76 ± 3
Anthracene	0.96 ± 0.20	58 ± 12
Pyrene	1.03 ± 0.04	62 ± 3

[a] Based on the natural rise time in response to a step function increase in aqueous concentration (n = 4). The kinetic limit was determined from the slope of the plot of $\ln(1 - S_t/S_\infty)$ between S_t/S_∞ = 0.1 to 0.9, where S_t and S_∞ are the MS signals at time t and at steady-state, respectively.[100]

Chapter 3: Physicochemical Properties of Contaminants Measured with Condensed Phase Membrane Introduction Mass Spectrometry (CP-MIMS)

This chapter represents a collection of unpublished work wherein Misha Zvekic was primarily responsible for investigation, conceptualization, methodology, validation, formal analysis, original draft writing, and visualization. This work was done in collaboration with Joseph Monaghan (conceptualization and methodology), Angelina Jaeger (investigation), Simon Maguire (investigation), and Erik T. Krogh (conceptualization, resources, project administration, funding acquisition, and supervision).

3.1 Introduction

Understanding the physicochemical properties of contaminants increases our ability to predict their environmental fate and distribution.[15] These properties also inform proper sample handling (e.g., chemical stability) with important implications for environmental monitoring campaigns and toxicity exposure studies. There are numerous physicochemical properties relevant to the fate of an aqueous chemical contaminant, such as solubility ($C_{\mathrm{w}}^{\mathrm{sat}}$), air-water partitioning (K_{aw}), acid dissociation constant (pK_{a}), and sorption partitioning to sediments (K_{D}).[6] Studying these properties for ultra-trace contaminants can be laborious and time-consuming. Prior to measurement, centrifugation and/or filtration is often required, and preconcentration steps (such as liquid-liquid or solid phase extraction) is typically needed to enrich trace contaminants.[101,102] Instead, predictive computational modelling is often used. However, *ab initio* calculations can be computationally expensive with limited user insight on their methods, whereas semi-empirical approaches often rely on empirical data for structurally related compounds. For emerging contaminants, a paucity of empirical data can result in low accuracy predictions, so experimental results are necessary.

An emerging contaminant of concern, *N*-(1,3-dimethylbutyl)-*N*'-phenyl-*p*-phenylenediamine-quinone (6PPD-quinone), was linked to salmon toxicity in 2020.[31] Subsequently, 6PPD-quinone (6PPDQ) and other structurally related *para*-phenylenediamine quinones (PPDQs, see **Figure 3.1.1**) have been detected in many environmental compartments including air, sediments, and biota.[32–36] These PPDQs are derived from the oxidation of *para*-phenylenediamines which are added to tires at 1–2% levels as anti-oxidants to preserve rubber integrity.[31] For PPDQs, the lack of physicochemical information or strong confidence in predictions has led to inconsistencies in sample handling.[34,101] There are also contradictions in literature between predicted and measured properties.[101,103] Hu *et al.* recently evaluated the aqueous solubility of 6PPDQ to be 38 ± 10 μg L^{-1}, whereas EPI Suite has been used to predict a value of 56.93 mg L^{-1}.[101] While software suites (e.g., EPI Suite and BIOVIA COSMOtherm) have been employed to predict properties for the analog PPDQs,[103–105] experimental values are necessary for these emerging contaminants.

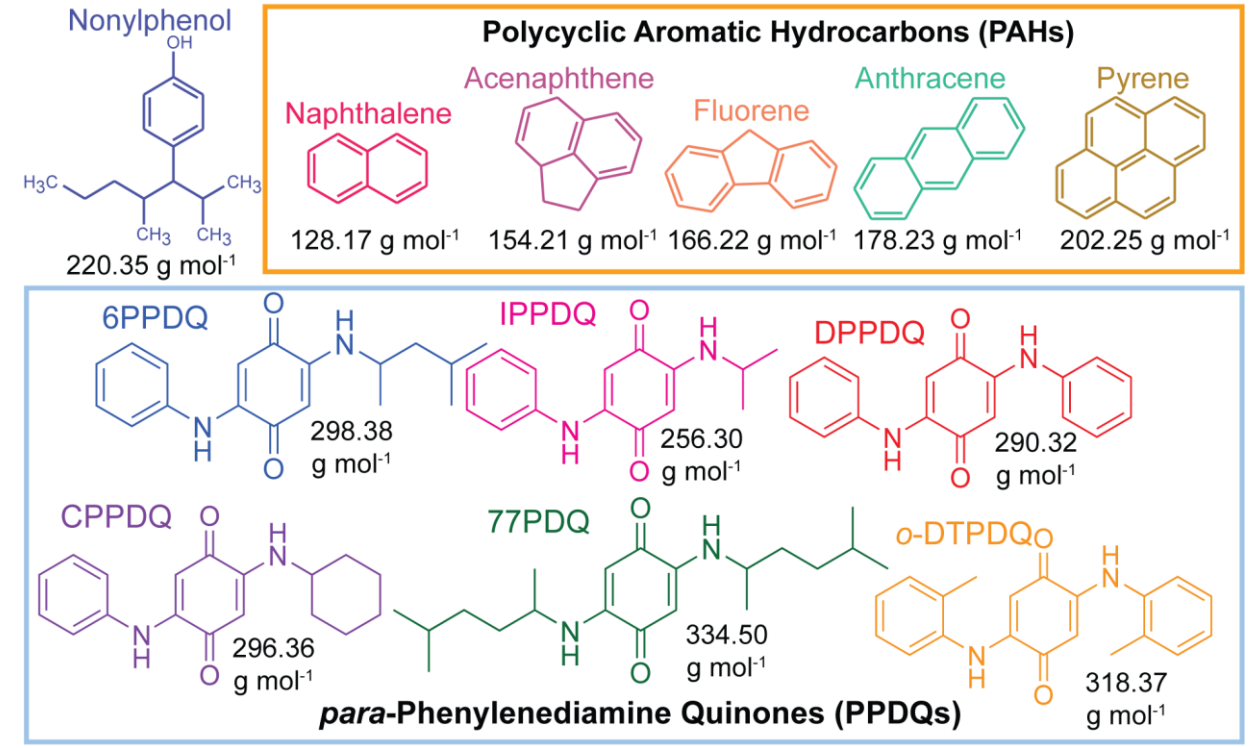

Figure 3.1.1. Analytes under study for their physicochemical properties including nonylphenol, polycyclic aromatic hydrocarbons (PAHs, yellow border), and *para*-phenylenediamine quinones (PPDQs, blue border).

DMS approaches may be suitable to overcome the challenges outlined above (long analysis time, extensive clean-up) for experimental evaluation of physicochemical properties. One such technique, condensed phase membrane introduction mass spectrometry (CP-MIMS) has already been used to directly measure these properties at trace-level concentrations.[34,79] The design and application of CP-MIMS is described in detail in **Chapter 2**. Neutral analytes free in solution permeate the polydimethylsiloxane (PDMS) membrane and are carried in the flowing solvent acceptor phase to the mass spectrometer for ionization and detection. Suspended solids and charged matrix components cannot cross the membrane, providing an online sample cleanup. Feehan *et al.* have previously used this technique to measure the pK_a of trace-organic contaminants directly in aqueous solution, even for complex mixtures (e.g., naphthenic acids derived from crude oil).[106] Termopoli *et al.* used CP-MIMS to directly measure the solubility limit of pyrene in water,[79] and several studies have used CP-MIMS to evaluate sorption of trace organic contaminants to various media (**Chapter 2**).[34,77,107]

Here, CP-MIMS was applied to characterize physicochemical properties of different classes of chemical contaminants, both legacy and emerging. Five polycyclic aromatic hydrocarbons (PAHs) and nonylphenol were analyzed for their chemical partitioning at equilibrium. PAHs are legacy contaminants which have been regulated for decades with (relatively) well-understood physicochemical properties.[108] Previous work with CP-MIMS has been undertaken to analyze their solubility and long-term sorption behaviour at non-

equilibrium conditions (**Chapter 2**).[107] Here, CP-MIMS was used to expand upon this earlier work to find sorption partition coefficients of PAHs, nonylphenol, and PPDQs at equilibrium/near-equilibrium conditions for a range of sorbents (including sediments and plastics) using high throughput automated analysis [34] and the aqueous solubility values for 6PPDQ and five structural analogs.

3.2 Materials and Methods

3.2.1 Chemicals and reagents

Deionized water (18 MΩ-cm, Facility Scale Reverse Osmosis/Ion Exchange Water Purification System, Applied Membranes Inc., Vista, CA, USA) was used to prepare samples and standards. The solvent acceptor phase was 15/85 (*v/v*) heptane/methanol solution. HPLC-grade solvents were purchased from Fisher Scientific (Ottawa, ON). Nonylphenol (97%), naphthalene (99%), pyrene (98%), acenaphthene (99%), and fluorene (98%) were purchased from Sigma Aldrich (Oakville, ON, CAN) and anthracene (99%) was purchased from Alfa Aesar (Ward Hill, MA, USA). 6PPDQ, IPPDQ, 77PDQ, DTPDQ, DPPDQ, and CPPDQ were obtained from HPC Standards Inc (Atlanta, GA, USA). Isotopically-labelled 6PPDQ ($^{13}C_6$-6PPDQ) was purchased from ACP Chemicals (Montreal, QC, CAN). For analysis of PPDQs, the acceptor phase solution included 20 ppb $^{13}C_6$-6PPDQ internal standard and was acidified with 0.03% formic acid (Fisher Chemical, Ottawa, ON). ≥99.8% tris(hydroxymethyl)aminomethane (Sigma-Aldrich, St. Louis, MO, USA) was used to buffer the sorbent donor phase solutions, and the pH was adjusted using hydrochloric acid (HCl) or sodium hydroxide (NaOH). Sorbents included various sediments including Ottawa Sand (f_{OC} = 0%; Chromatographic Specialties Inc.), Clean Sandy Loam (f_{OC} = 1.85%; Sigma-Aldrich), Clean Loam Soil (f_{OC} = 5.96%; Sigma-Aldrich), and both pristine and UV-weathered low-density polyethylene (LDPE, Sigma Aldrich). Surface areas were measured via N_2-BET isotherm and are listed in **Table 3.2.1**. LDPE pellets were rinsed with methanol, air-dried, and exposed to 254 nm light for 8.8 days. Surface functional group changes due to photochemical ageing were monitored and reported in detail elsewhere.[29,107]

Table 3.2.1: Surface area data measured and provided by Dr. Marzieh Baneshi from the Dr. Stephanie MacQuarrie lab at Cape Breton University

Sorbent	Identity	BET Surface Area ($m^2\ g^{-1}$)	Langmuir Surface Area ($m^2\ g^{-1}$)
Loam Soil	CLNSOIL3-100G; Sigma-Aldrich	10.6131	15.4847
Sandy Loam	CLNLOAM6-100G; Sigma-Aldrich	4.0130	5.8392
Weathered Low-Density Polyethylene	CAT # 428043; Sigma-Aldrich	1.5350	2.6262
Pristine Low-Density Polyethylene	CAT # 428043; Sigma-Aldrich	Not available	

3.2.2 Instrumentation

PAH and nonylphenol experiments. Analysis was conducted with a single quadrupole (5975, Agilent Technologies Inc., Santa Clara, CA, USA) mass spectrometer coupled to an LEI interface described in **Chapter 1**. The selected ion monitoring (SIM) *m/z* measured with LEI are listed in **Table 3.2.2** and the mass spectrometer settings were listed in **Table 2.5.3** from **Chapter 2**. The construction and dimensions of the CP-MIMS probe used have been described previously (**Chapter 2**).[107] Briefly, polydimethylsiloxane (PDMS) membrane (8.0 cm long, 170 µm thick, Silastic brand, Dow Corning, Midland, MI, USA) was mounted on 22-gauge stainless-steel tubing. The acceptor phase was flowed at 50 µL min^{-1} with an HPLC pump (1100 series, Agilent Technologies). This flow was reduced post-membrane to ~400 nL min^{-1} using a passive flow-splitter.

Table 3.2.2: Selected Ion Monitoring (SIM) channels followed with the 5975 MS

Analyte	Selected Ion Monitoring (*m/z*)
Nonylphenol	107
Naphthalene	128
Acenaphthene	153
Fluorene	166
Anthracene	178
Pyrene	202

PPDQ experiments. Analysis was conducted using electrospray ionization coupled to a triple quadrupole mass spectrometer (ESI-MS/MS; Perkin-Elmer QSight™ 220, Waltham, MA, USA). Instrument parameters and MS/MS transitions are listed in **Table 3.2.3**. The dimensions of the CP-MIMS probe used have been described elsewhere.[34] For solubility studies, the same probe dimensions described previously and in **Chapter 2** was used. For sorption studies, the PDMS membrane (7.6 cm long, 55 µm thick, Permselect, MedArray, Inc., Ann Arbor, MI, USA) was mounted on 31-gauge stainless steel min^{-1}

capillaries (Microgroup, Medway, MA, USA). The acceptor phase was delivered at 10 µL by a syringe pump (Chemyx Fusion 100, Stafford, TX, USA) and 10 mL gas-tight syringe (Hamilton 1000 series, Fisher Scientific).

Table 3.2.3: SRM scans mass spectrometric settings and MS/MS transitions for the Perkin-Elmer QSight 220 ESI-MS/MS

Analyte	$[M+H]^+ \rightarrow$ Fragment SRM *m/z* transitions	Entrance Voltage (V)	CC L2 (V)	Collision cell (V)
$^{13}C_6$-6PPDQ	305→221	10	−56	−25
6PPDQ	299→256	12	−56	−30
DTPDQ	319→212	10	−84	−31
DPPDQ	291→263	19	−52	−32
IPPDQ	257→215	15	−60	−23
CPPDQ	297→215	19	−64	−26
77PDQ	335→237	25	−92	−26

† Positive ion spray voltage: +4.0 kV, hot-surface induced desolvation (HSAID) source: 320 °C, nebulization gas: 120 psi

3.2.3 Thermodynamic sorption studies

Sorption of PAHs and Nonylphenol to LDPE. LDPE pellets (0.0314 ± 0.0008 g) were added to a blank vial and multi-component solution vials ranging from 30–100 ppb (nonylphenol, naphthalene, acenaphthene, fluorene, and pyrene) and 9–30 ppb (anthracene). Vials with no sorbent added, containing the same concentrations, were used as a negative control. The samples were left stirring at 240 RPM at ambient room temperatures for 11 days until measurement.

Sorption of PPDQs to LDPE and Sediments. For these solutions, the donor phase contained 50 mM tris(hydroxymethyl)aminomethane pH-adjusted to 8.08–8.10. Six sorbent series were created: 1) a blank treatment to which no sorbents were added, 2) pristine LDPE, 3) UV-aged LDPE, 4) Sandy Loam, 5) Loam Soil, and 6) Ottawa sand. For single-component sorption, a methanolic stock of 6PPDQ was used to create a series of aqueous solutions with concentrations ranging from 0–1000 ng L^{-1}. The mass of added sorbents were 0.50 ± 0.01 g for sediments and 0.53 ± 0.02 g for plastics (17 pellets). The solutions were agitated on a shaker table at 240 RPM for 34 days prior to measurement. For multi-component sorption isotherms, a methanolic stock (137.3–146.0 mg L^{-1}) was used to create aqueous solutions with concentrations ranging from 0–1170 ng L^{-1}. The mass of sorbents added to each vial were 0.50 ± 0.01 g for sediments and 0.30 ± 0.01 g for plastics. The samples were prepared and left to shake at 200 RPM until the time of measurement ~42 days later. Due to these experiments being equilibrated at different times of the year, there may have been as much as a 5 °C difference in the ambient room temperature, with the multi-component sorption series experiencing higher temperatures (~20 °C). For multi-component sorption, the sorbent series 1, 2, and 4 were created in

triplicate. All sorbent series were measured in triplicate, and the resulting K_D and associated uncertainty represents the mean and standard deviation.

Table 3.2.4: Percent of analyte remaining after 6 weeks across a series [a]

Analyte [b]	6PPDQ	IPPDQ	CPPDQ	77PDQ
Percent Remaining (%) $\bar{x}$ ± sd	94 ± 10	90 ± 5	97 ± 13	37 ± 21

[a] Calculated using the same-day calibration curve to quantify the no-sorbent control series (4 standard solutions) and dividing those values by their known, initial concentration.
[b] DTPDQ and DPPDQ were not calculated due to concentration differences in the stock solution used to build the calibration curve and the original control solutions.

Quantification. Quantification was carried out using 5-point calibration curves created the day of sample analysis. In the multi-component PPDQ sorption studies, the percent of 77PDQ remaining in solution after 6 weeks had poor recovery (**Table 3.2.4**) indicating poor stability over time for PPDQs, which has been observed previously in open vials especially for 77PDQ.[77] Additionally, DPPDQ and DTPDQ were not fully solubilized when building the same-day calibration curve. Thus, for the multi-component sorption experiments the control series was used for quantification instead of the same-day calibration curve. Both quantification models yielded comparable results for 6PPDQ (**Table 3.2.5**). An in-house constructed autosampler, described elsewhere,[34] was employed for analysis of PPDQ samples. After measuring each vial, the probe was submerged in methanol to prevent sample carry over and for the signal to reach baseline signal intensity. After every 5 samples, a calibration check solution and a DI water blank were measured to confirm stable instrument performance. For PPDQ quantification, all signal intensities were normalized to the acceptor phase isotopically-labelled 6PPDQ internal standard to compensate for ionization effects and signal drift. Because $^{13}C_6$-6PPDQ was used as internal standard, the poor performance for some PPDQs (77PDQ, DTPDQ, DPPDQ) may be attributable to poor compensation from the same internal standard used. Future work will test this hypothesis using recently acquired isotopically-labelled standards for DPPDQ and DTPDQ.

Table 3.2.5: Calculated K_D (L/g) for 6PPDQ with different quantification methods

Calibration Curve	Same-Day Calibration Series	Calibration using Control Series (no added sorbent)
Sandy Loam	0.18±0.04	0.13±0.04
Loam Soil	0.19±0.06	0.20±0.07
Pristine LDPE	1.87±0.08	1.54±0.07
Weathered LDPE	18.42±0.90	18.39±0.93
Ottawa Sand	0.47±0.38	0.39±0.13

Sorption isotherms and partition coefficients. When equilibrium conditions are followed at the limit of low concentrations, a linear isotherm can be applied.[109] To calculate partition coefficients (K_D), linear isotherm plots were constructed. The analyte

concentration in solution (µg L^{-1} or ng L^{-1}) was plotted on the x-axis and the mass amount of PPDQ on the mass of sorbent (µg g^{-1} or ng g^{-1}) was plotted on the y-axis for all solutions in a series at equilibrium. To calculate the mass of analyte on the sorbent, the mass of sorbate measured in solution was subtracted from the theoretical sorbate mass loading, and divided by the mass of sorbent. The slope of the resulting plot is equivalent to the sorption partition coefficient (K_D) (L g^{-1}). To convert K_D to K_{OC}, the fraction of organic carbon (f_{OC}) as used as illustrated in **Equation 3.1**:

$$K_{OC} = K_D / f_{OC} \qquad \textbf{(Equation 3.1)}$$

3.2.4 Aqueous solubility of PPDQ analogs

Solubility experiments were performed at 25.4 ± 0.2 °C in triplicate for 6PPDQ with anywhere from 13–16 additions of a 30 µL substock (6.9 mg L^{-1} in acetonitrile) into 37.0 mL of DI water (pH 5–6). Temperatures were controlled with a recirculating chiller (2095 Bath and Circulator, Forma Scientific, Marietta, OH, USA). A sample vial was placed inside a double-walled beaker and water from the chiller was circulated through the outer layer. The water temperature inside the beaker, equilibrated with the sample, was measured with a digital thermometer. This resulted in a final co-solvent concentration of 0.1% *v/v*. A control experiment evaluating the solubility of 6PPDQ at elevated methanol concentration (2% *v/v*) showed no significant change to the observed solubility (**Figure 3.2.1**). To examine the impact of temperature on 6PPDQ solubility, the experiment was repeated (n = 3) at 11.0 ± 0.3 °C and 41.0 ± 0.6 °C. The solubility of the PPDQ analogs were examined in a similar fashion using 10 µL spikes of stock solution (in methanol: 1.77 mg L^{-1} DTPDQ, 54.4 mg L^{-1} IPPDQ, 22.1 mg L^{-1} CPPDQ, 2.88 mg L^{-1} 77PDQ, and acetonitrile: 39.4 mg L^{-1} DPPDQ).

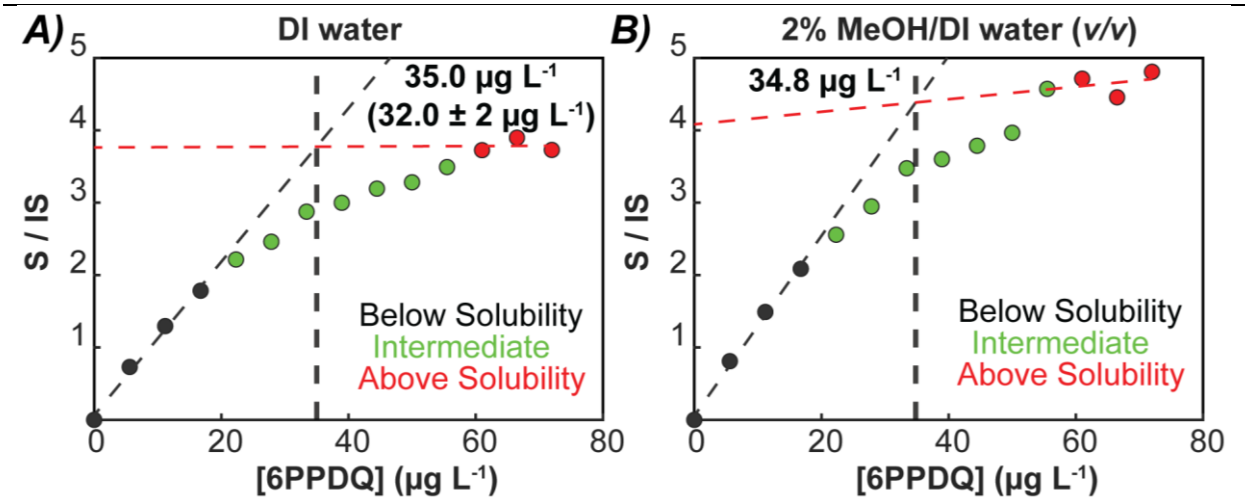

Figure 3.2.1. Comparison of 6PPDQ solubility in A) deionized water and B) deionized water with 2% methanol co-solvent.

3.3 Results and Discussion

3.3.1 Sorption studies for PAHs, PPDQs, and nonylphenol

The partitioning of chemical contaminants to both natural sediments and anthropogenic plastics was investigated. Characterizing sorption behaviour is necessary for predicting the free and available fraction of analytes in the environment, as well as understanding the potential for contaminant remobilization or the operation of engineered treatment systems. Here, linear isotherms were measured for low and high organic fraction (f_{OC}) sediments, and pristine and photochemically-aged low-density polyethylene plastic. Non-linear isotherms such as Freundlich and Langmuir models also describe sorption processes, but at the limit of low concentrations linear behaviour can be observed and modelled with the Henry isotherm.[109] The resulting slope of the linear isotherm (K_D) corresponds to the concentration on the solid sorbent (μg g^{-1}) over the concentration in aqueous solution (μg g^{-1}) at equilibrium. Sorption experiments were carried out by varying the concentration of chemical sorbates in solution while keeping the mass loading of sorbents constant.

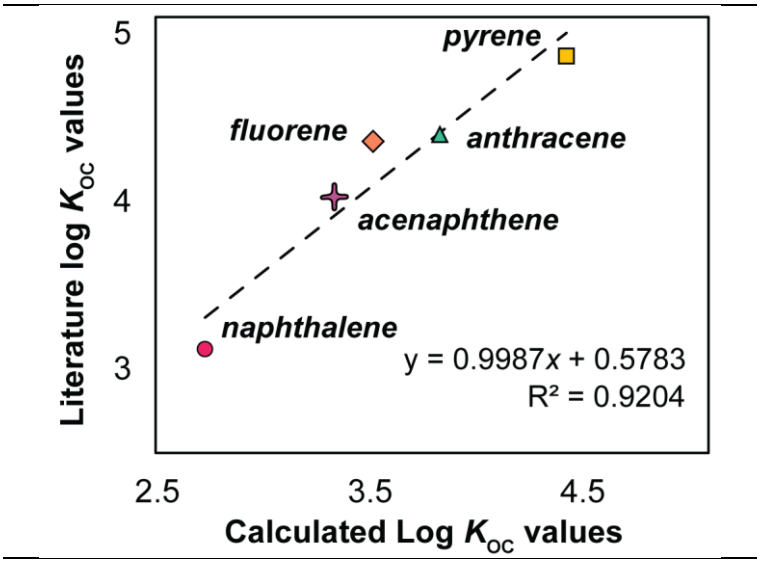

Figure 3.3.1. Comparison of literature log K_{OC} values from Jesus *et al.* [110] to the K_{OC} values calculate from our results (log K_{OC} = log(K_D / f_{OC}); wherein f_{OC} is assumed to be unity for LDPE plastics).

A proof-of-principle experiment was performed analyzing the sorption of the same PAHs and nonylphenol which were used to characterize sorption kinetics in **Chapter 2**. In previous work, equilibrium for LDPE and anthracene, pyrene, naphthalene, and nonylphenol was observed to occur within a week (see **Figure 2.3.3**).[107] Isotherm experiments were set up based on this equilibration time. Sorption data was collected and subsequently fit to a linear sorption isotherm, with good linearity for PAHs studied (R^2 on average was 0.91 for the PAHs, **Figure 3.3.2A**). K_D values for PAHs ranged from 0.5 ± 0.2 to 27 ± 6 L g^{-1} as listed in **Table 3.3.1.** This experiment was performed once, and the

uncertainties reported are based upon the uncertainty in the slope. Consistent with the kinetic and thermodynamic results discussed in **Chapter 2** (**Figure 2.3.2** and **Figure 2.3.4**), nonylphenol had the lowest sorption affinity (**Figure 3.3.2A**) and this compound was observed to have the lowest R^2 value (0.55) and hence largest uncertainty on K_D value (0.2 ± 1 L g^{-1}). The K_D values for the structurally related series of PAHs were found to scale linearly (R^2 = 0.986) with their hydrophobicity as depicted in the linear free energy relationship (**Figure 3.3.2B**). Partition coefficients for PAHs have been previously analyzed,[9] typically being converted to log K_{OC} (L kg^{-1}).[110] Assuming 100% organic carbon content (f_{OC} ~ 1), the calculated log K_{OC} values were in very good agreement with literature values with a slope of log-log plot of 0.998 (see **Figure 3.3.1**).[110] It should be noted that log K_{OC} values are not typically determined on plastics which may explain small discrepancies between literature values and those reported here.

Table 3.3.1: Partition coefficients and log K_{OC} for nonylphenol and PAHs to LDPE [a]

Analyte	R^2	K_D (L g^{-1})	log K_{OC} (L kg^{-1})
Nonylphenol	0.55	0.2±0.1	2±1
Naphthalene	0.79	0.5±0.2	2.7±0.8
Acenaphthene	0.90	2.2±0.3	3.3±0.5
Fluorene	0.96	3.3±0.4	3.5±0.4
Anthracene	0.96	6.9±0.9	3.8±0.5
Pyrene	0.89	27±6	4.4±0.9

[a] Measurement and experiment were performed once (n = 1). The uncertainty represented here is the uncertainty of the linear regression.

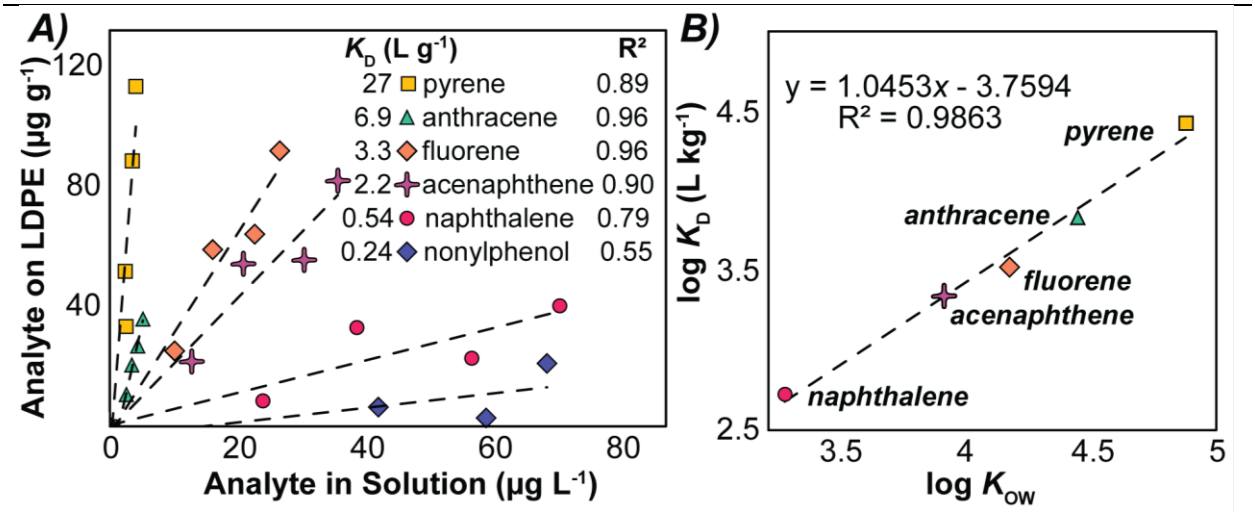

Figure 3.3.2. A) Linear sorption isotherms for 5 polycyclic aromatic hydrocarbons (PAHs; pyrene, anthracene, fluorene, naphthalene, and acenaphthene) and nonylphenol. Partition coefficients (L g^{-1}) and R^2 are included in the legend. B) Log-log plot of the partition coefficients over the hydrophobicity (K_{OW}) for the PAHs.

It is apparent that CP-MIMS can be applied to rapidly and directly screen complex heterogeneous sorption solutions to yield meaningful isotherms without filtration,

centrifugation, or pre-concentration steps. Similar sorption isotherm experiments were subsequently set up for six PPDQ analogs (6PPDQ, IPPDQ, 77PDQ, DTPDQ, DPPDQ, and CPPDQ) on five sorbents (pristine and UV-weathered LDPE, low and high f_{OC} sediments, and a negative control (Ottawa sand)). After 6 weeks of room temperature equilibration on a shaker table, the PPDQ samples were analyzed for the remaining solution phase concentrations using CP-MIMS with ESI and tandem mass spectrometry. Sorption of 6PPDQ was analyzed by itself and in the presence of the five PPDQ analogs. The percent of each analyte remaining in solution after six weeks are listed in **Table 3.2.4**. Analyzing these samples would be incredibly difficult without the use of automated CP-MIMS, as the sorption series require multiple experimental samples to find one K_D value. 150 samples were required for multi-component sorption analysis and these vials were all measured in triplicate. In total, >270 samples were required for single- and multi-component sorption analysis. This translates to >480 analyses when including calibration, quality assurance and control, and replicate measurement.

Table 3.3.2: Partition coefficients (K_D (L/g)) for the PPDQ analogs to different sorbents. [a]

	Sandy Loam	Loam Soil	Pristine LDPE	Weathered LDPE	Ottawa Sand
6PPDQ	0.13±0.04	0.20±0.07	1.54±0.07	18.3±0.9	0.39±0.13
DTPDQ	1.6±0.9	0.21±0.06	3.4±1.1	18±15	nd
DPPDQ	nd	1.2±0.1	1.3±0.5	6.6±3.1	nd
IPPDQ	nd	nd	nd	0.56±0.35	nd
CPPDQ	0.34±0.04	0.24±0.05	1.8±1.0	13±1	0.59±0.20
77PDQ	nd	1.59±0.32	13.1±4.9	nd	nd

[a] When the standard deviation was larger than the mean, K_D value is stated as a non-detect by this methodology.

The sorption of 6PPDQ on the two LDPE sorbents was significantly higher than that observed on the two sediments and the sand, which were difficult to distinguish from one another as seen in **Figure 3.3.3.A** and summarized in **Table 3.3.2**. This is likely due to the considerably lower fraction of organic carbon in these samples. Ottawa sand, high f_{OC} sandy loam, and low f_{OC} loam soil had low partition coefficients ranging from 0.13 ± 0.04 L g^{-1} (sandy loam) to 0.39 ± 0.13 L g^{-1} (Ottawa sand). The partition coefficient for pristine LDPE was 1.54 ± 0.07 L g^{-1}, 4× greater than the largest sediment K_D. The highest K_D for 6PPDQ was on weathered LDPE (18 ± 1 L g^{-1}), 12× greater than pristine LDPE. Comparing the sorption partition coefficients of different PPDQs to pristine LDPE (**Figure 3.3.3.B**), the trends were 77PDQ (13 ± 5 L g^{-1}) >> DTPDQ (3.4 ± 1 L g^{-1}) > 6PPDQ (1.54 ± 0.07 L g^{-1}) = CPPDQ (1.81 ± 1.04 L g^{-1}) > DPPDQ (1.3 ± 0.5 L g^{-1}) > IPPDQ (**Table 3.3.2**). IPPDQ did not sorb significantly under the conditions employed in this study.

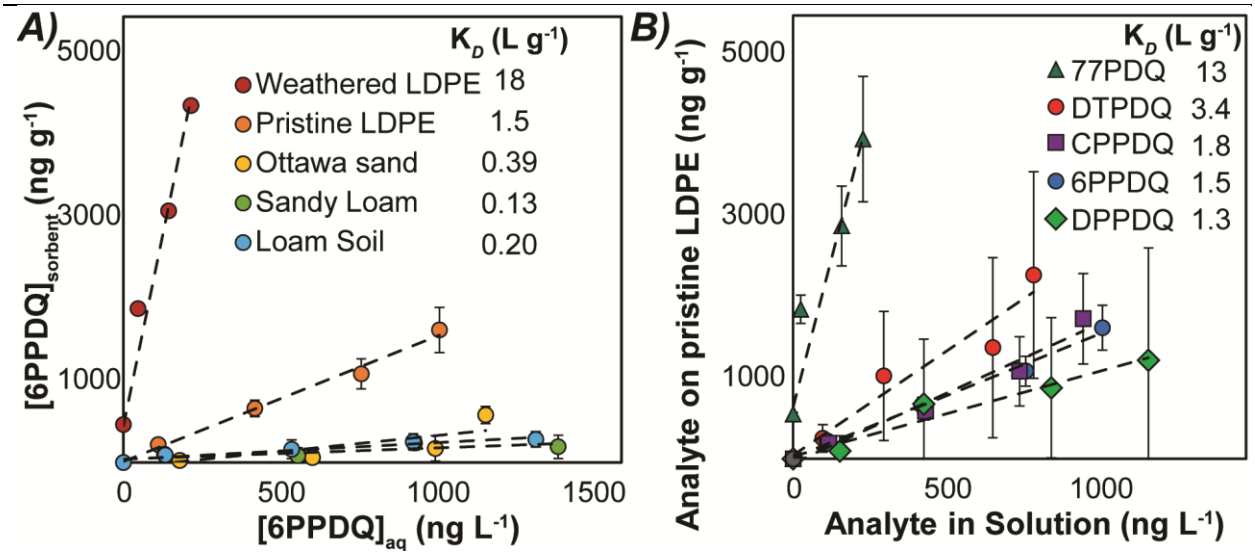

Figure 3.3.3. Linear sorption isotherms for A) 6PPDQ to five sorbents and B) the six PPDQ analogs to pristine low-density polyethylene (LDPE).

Examining overall sorption trends (**Figure 3.3.4A** and **Table 3.3.2**) showed variation depending on the compound. Generally, the greatest sorption occurred to weathered LDPE, followed by pristine LDPE, with sediments demonstrating the least sorption. There was little sorption to IPPDQ and 77PDQ, and higher K_D values were observed generally for CPPDQ, 6PPDQ, DTPDQ, and DPPDQ. CPPDQ and DTPDQ showed similar trends as 6PPDQ, albeit with slightly higher partition coefficients. DPPDQ also showed the same relative order of K_D as 6PPDQ, with lower relative partition coefficients, while showing no detectable sorption to sandy loam or Ottawa sand. On 77PDQ, only sorption to loam soil (1.6 ± 0.3 L g^{-1}) and pristine LDPE (13 ± 5 L g^{-1}) was detectable (**Table 3.3.2**), and all other partition coefficients were too small to be measured with confidence. The high K_D for 77PDQ on pristine LDPE, coupled to the large relative error, indicates potential loss that was not completely accounted for when using the control solutions to quantify aqueous concentrations. The only measurable K_D for IPPDQ occurred to weathered LDPE (0.6 ± 0.4 L g^{-1}).

Typically, microplastic-organic contaminant sorption is driven by hydrophobic interactions. This explains why there was greater sorption for plastic compared to sediments in this study, despite sandy loam and loam soil having larger surface areas than the plastics (**Table 3.2.1**). However, increased sorption to weathered LDPE compared to pristine LDPE was consistently observed for the PPDQs (**Figure 3.3.4B**). This phenomenon has been previously observed for compounds that contain polar functional groups (such as the PPDQs) and attributed to the process of plastic weathering resulting in an addition of surface polar functional groups capable of participating in hydrogen-bonding interactions (**Figure 2.5.10**).[107] The exception was 77PDQ which showed more sorption to pristine than weathered plastic (**Figure 3.3.4A**). This compound's bulky alkyl sidechains (**Figure 3.1.1**) may potentially sterically hinder hydrogen-bonding interactions.

Table 3.3.3: K_{OC} for the PPDQ analogs to different sorbents.

	Sediment Sorbents	Sandy Loam	Loam Soil
	Fraction Organic Matter (%)	5.96	1.85
K_{OC} (L g^{-1}) (log K_{OC}, L kg^{-1})	6PPDQ	2.2±1 (3.3±2.8)	11±4 (4.0±3.6)
	DTPDQ	27±15 (4.4±4.2)	11±3 (4.1±0.5)
	DPPDQ	5.8±6 (3.8±3.8)	63±6 (4.8±0.8)
	CPPDQ	5.8±1 (3.8±2.8)	13±3 (4.1±0.4)
	77PDQ	30±33 (4.5±4.5)	86±17 (4.9±1.2)

The results (**Table 3.3.3**) are in reasonable agreement with recent work performed by others. Partitioning coefficients between organic carbon and water (log K_{OC}, L kg^{-1}) for 6PPDQ have been found to be 3.2–3.5 [32] for road dust and 2.8–3.6 for sediments.[34] For 6PPDQ, the range of values found was between 3.3–4.0 for different sediments (**Table 3.3.3**). Work in our group found a trend between low and high organic fraction sediment [34] after two days of sorption, but any difference was less obvious after weeks of equilibration (**Figure 3.3.3.** and **Figure 3.3.5**), suggesting that sorption on complex sorbents may have different kinetic regimes including initial sorption to surfaces exposed to the surrounding solution and a slower diffusion-limited process into the bulk sediment.[66,67] These results would indicate that equilibration time, agitation, and temperature may play a more central role and should therefore be closely monitored. Recently, Zhu *et al.* claimed to report values for log K_{OC} values 6PPDQ, 77PDQ, CPPDQ, and IPPDQ to real-world sediment but their results were internally inconsistent making it difficult to compare to our results.[33] However, their reported predicted log K_{OC} values (EPI Suite) were found to be in a similar range (3.2–4.5 for the different PPDQs) to the experimental values calculated here.[33]

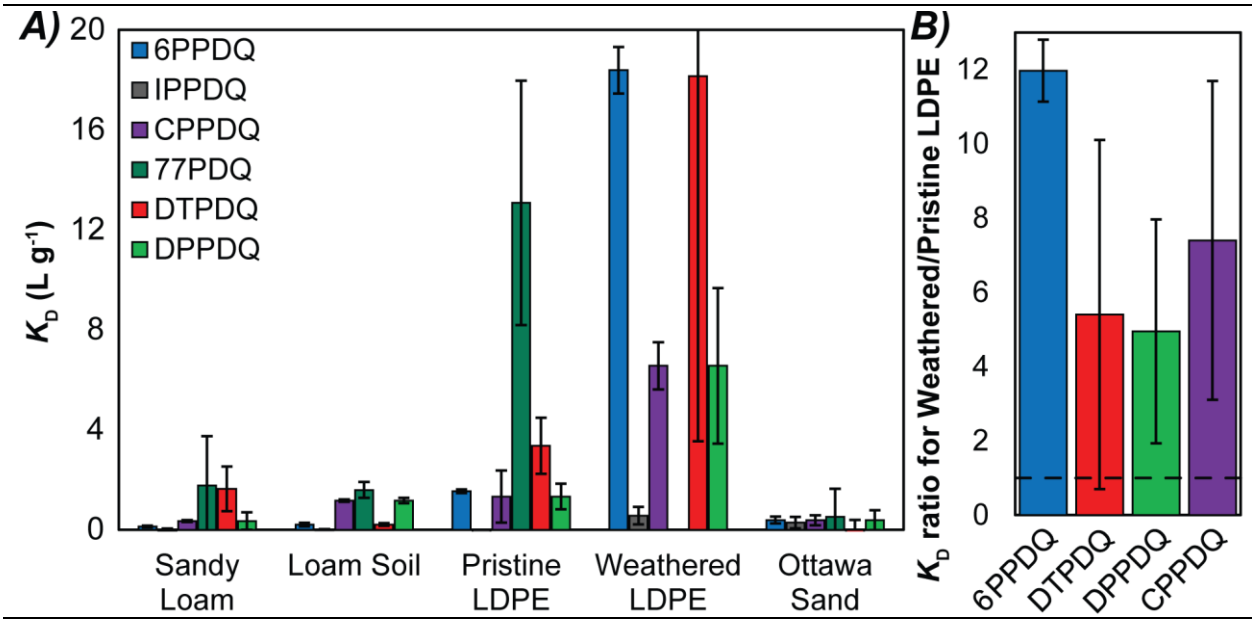

Figure 3.3.4. Summary of A) partition coefficients of the six PPDQ analogs to five sorbents and B) the ratio of the partition coefficients for weathered and pristine low-density polyethylene (LDPE) for the six sorbents.

Comparing sorption trends of 6PPDQ, by itself and in the presence of five other analogs, to five sorbents demonstrated the same sorption trends (**Figure 3.3.5**). The partition coefficients for 6PPDQ alone in solution were observed to have similar values for the sediments, though the K_D for the plastics appeared greater when 6PPDQ was sorbing alone (**Figure 3.3.5**). This is potentially due to small competitive sorption effects even at the very trace sorbate concentrations (~1 ppb 6PPDQ vs ~7 ppb PPDQs) used in these studies. It may also be due to increased sorption at slightly lower room temperatures for the solo sorption compared to the multi-component sorption experiments.

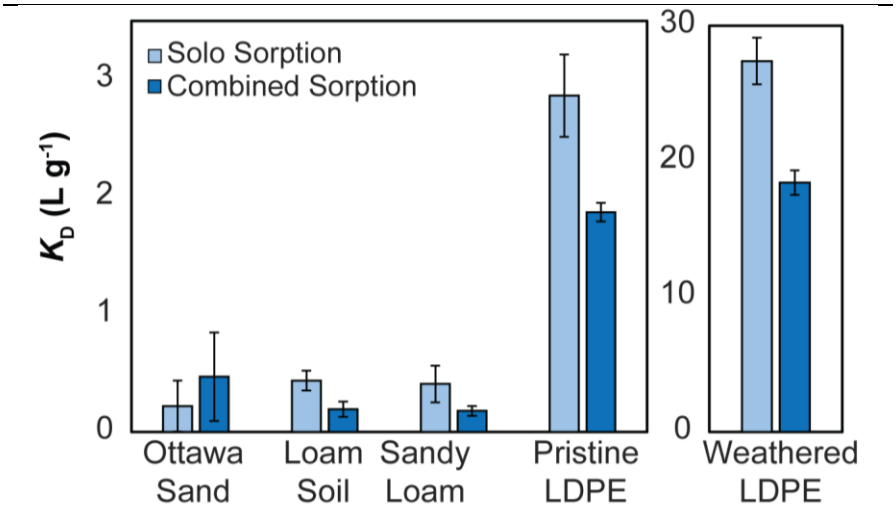

Figure 3.3.5. Comparison of 6PPDQ partition coefficients to five different sorbents alone (light blue) and in the presence of five other sorbates (dark blue). The solo sorption experiment was run from January-February, while the multi-component sorption was run from April-May. The temperatures were slightly (~2–5 °C) lower in the winter months.

3.3.2 Aqueous solubility limits for PPDQs

6PPDQ and analogs leach from tire wear particles (TWPs),[101] leading to high contaminant levels in stream water after the compounds dissolve and are carried into streams during rain events.[34] The degree to which this occurs is to some extent limited by the aqueous solubility limits of these compounds, a temperature-dependent property. The solubility of an analyte governs its behaviour in the aquatic environment, biological systems, and may provide challenges when constructing aqueous standards or toxicity studies if the solubility limits are exceeded. Various structural and thermodynamic factors influence solubility (C_w^{sat}) including the intermolecular forces between solute and solvent (6PPDQ can act as both an H-bond donor and acceptor) and the size (molar volume) of the compound. Solubility is an equilibrium (**Equation 3.2**) wherein the processes of solute dissolution and precipitation occur at equivalent rates. $\Delta G°$ can be defined in terms of K_{eq} (**Equation 3.3**) which can be related to the entropy change (ΔS) in a system when a solute dissolves, and the enthalpies (ΔH) of the solvent, solute, and solution.[9]

$$PPDQ_{(s)} \overset{\Delta G^\circ}{\rightleftharpoons} PPDQ_{(aq)} \quad \textbf{(Equation 3.2)}$$

$$\Delta G^\circ = -\mathrm{RT}\ln K_{eq} \quad \textbf{(Equation 3.3)}$$

Figure 3.3.6A shows the chronogram representing the signal over time as spike additions of a PPDQ are added to aqueous solution. The CP-MIMS probe is impermeable to undissolved compounds, enabling us to monitor a saturated solution *in situ*, measuring only the free concentration in solution without introducing solute to the instrument. This was demonstrated previously in our group, showing good agreement between experimental (135 µg L^{-1}) and literature (135 µg L^{-1}) solubility values for the PAH pyrene.[79] **Figure 3.3.6B** shows the resulting data wherein the signal is plotted over the concentration added to solution. The intersection of linear portion of the calibration curve (below the solubility limit, black data points) and the data points above the solubility limit (red data points) corresponds to the solubility limit.

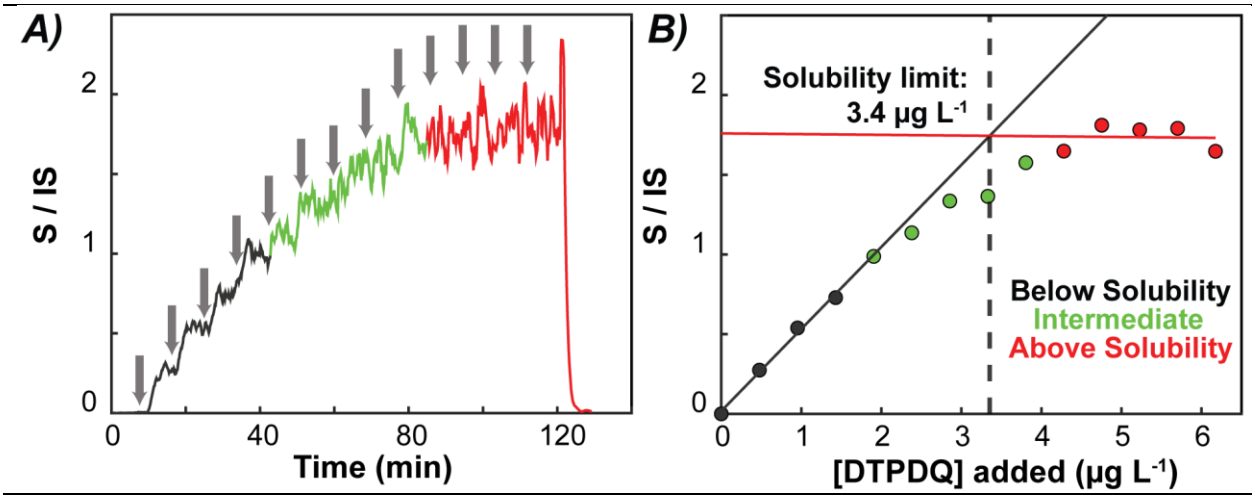

Figure 3.3.6. Sample solubility experiment for DTPDQ: A) sample chronogram of internal standard-corrected signal changing over time as spike additions (indicated with grey arrows) of DTPDQ are added to solution, and B) the resulting normalized signal response at concentrations below (black data), above (red data), and at intermediate (green data) solubility.

The solubility of PPDQ analogs (**Figure 3.3.7A**) at 25 °C were, in increasing order: DTPDQ (3.4 µg L^{-1}) < 77PDQ (5.9 µg L^{-1}) << 6PPDQ (31 ± 3 µg L^{-1}) = CPPDQ (31.5 µg L^{-1}) < IPPDQ (109.7 µg L^{-1}) << DPPDQ (160 µg L^{-1}). 6PPDQ's solubility was measured in triplicate, and the series of PPDQs had a clear trend spanning two orders of magnitude. DTPDQ and 77PDQ were observed to have the lowest solubility in aqueous solution, with 6PPDQ and CPPDQ at about the same intermediate solubility limit (9-fold greater than DTPDQ), with IPPDQ (32-fold greater than DTPDQ) and DPPDQ (47-fold greater than DTPDQ) having the highest solubility limits.

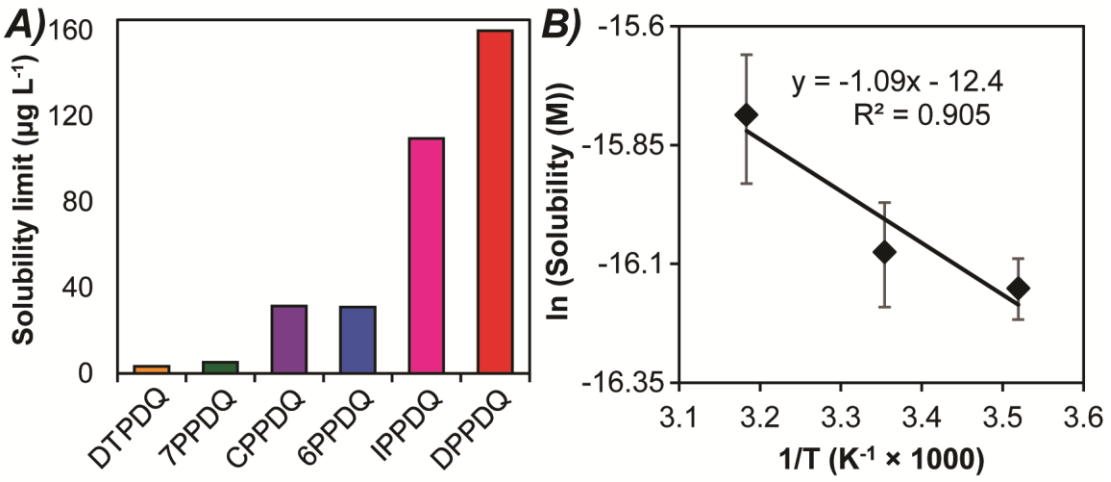

Figure 3.3.7. A) Solubility limits of the PPDQs in increasing order, and B) the resulting Van't Hoff plot of the solubility limit (M) 6PPDQ at three different temperatures (11, 25, and 41 °C)

The solubility limit of 6PPDQ (31 ± 3 µg L^{-1}) agreed with the experimental value previously found by Hu *et al.* (38 ± 10 µg L^{-1}).[101] Molar volumes of the PPDQ analogs considered here were estimated using the molar volume occupied by each atom and the number of bonds.[9,111] As expected for a structurally related series, a linear free energy relationship was observed between aqueous solubility and estimated molar volume (**Figure 3.3.8**) with the exception of DTPDQ. The larger an organic contaminant is, the more water-water solvent interactions need to be disrupted to create this hydrophobic cavity. This raises its free energy of solution, consequently lowering its solubility.[9] Accordingly, 77PDQ had the second lowest solubility limit, attributable to its relatively large ($-C_7H_{15}$) alkyl side chains. CPPDQ and 6PPDQ had similar solubility limits and estimated molar volumes, each with a $-C_6H_{13}$ sidechain, in cyclic and alkyl forms, respectively. IPPDQ was the smallest PPDQ analyzed here (**Table 3.2.3**) and had one of the largest solubilities, following DPPDQ which had a similar estimated molar volume (**Figure 3.3.8**). It was unexpected that the solubilities of DTPDQ and DPPDQ were on either extreme, given that the compounds are similar outside of the methyl groups present on the aromatic rings on DTPDQ (**Figure 3.1.1**). DTPDQ was a clear outlier (**Figure 3.3.8**) and this may indicate that another factor is influencing the solubility or molar volume of DTPDQ in solution, such as dimerization. Generally, DTPDQ and DPPDQ exhibit anomalous behaviour in aqueous solution (e.g. inconsistent signal intensity in calibration standards). The reasons for this are still under investigation, but caution should be exercised interpreting results for these two compounds.

For 6PPDQ, the impact of temperature on water solubility was also investigated. The solubility increased slightly with temperature, ranging from 29 ± 2 to 42 ± 6 µg L^{-1}. A van't Hoff plot was created by plotting the natural logarithm of the solubility against the reciprocal of the absolute temperature (**Figure 3.3.7B**). A linearized form of the Van't Hoff equation (**Equation 3.4**) was used to find the enthalpy (ΔH) of dissolution from the slope.[9]

$$\ln C_{\mathrm{w}}^{\mathrm{sat}} = -\frac{\Delta H}{\mathrm{RT}} + \text{constant} \qquad \textbf{(Equation 3.4)}$$

In the case of the dissolution for a solid, the enthalpy term consists of the excess enthalpy of the solution as well as the enthalpy (ΔH_{fusion}) of the process of the structured intermolecular forces of the solid breaking in a process alike melting during dissolution.[9] The enthalpy change calculated from **Figure 3.3.7B** was 9 ± 3 kJ mol^{-1}, where the uncertainty was calculated from the standard error of the slope. The dissolution of 6PPDQ is an endothermic process, as evidenced by positive calculated enthalpy change.

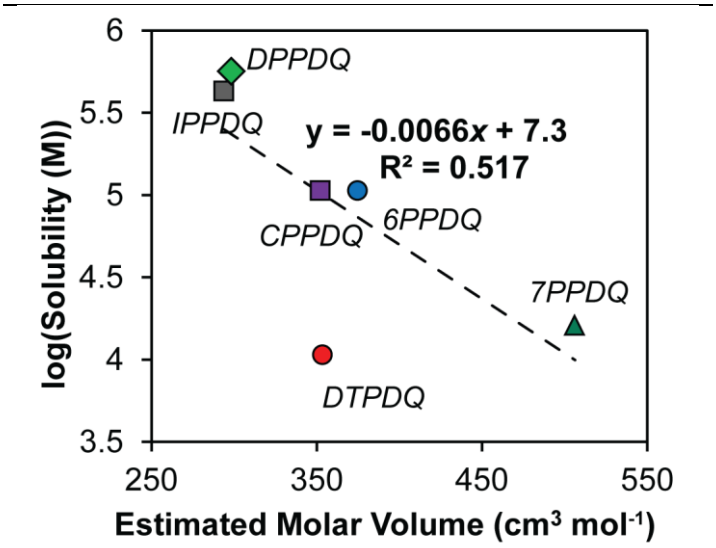

Figure 3.3.8. Aqueous solubility against estimated molar volume using the atomic volume approach (V_{ix}) outlined by Abraham and McGowan which is based on characteristic atomic volumes and subtracted bond volumes.[9,111]

3.4 Conclusion

The environmental fate and distribution of contaminants are governed by their physicochemical properties. Knowing these properties can ensure proper sample handling, assist treatment and mitigation strategies, and increase the accuracy of predictive modelling. Here, condensed phase membrane introduction mass spectrometry (CP-MIMS) was applied as a direct and high throughput approach to measure select physicochemical properties (aqueous solubility and partitioning). The solubility limits at 25 °C for six *para*-phenylenediamine quinones (PPDQs), and for 6PPDQ at 11, 25, and 41 °C, are reported. Solubility scaled with the estimated molar volume for the PPDQs, and to our knowledge report the enthalpy of dissolution of 6PPDQ for the first time. Here six PPDQs, nonylphenol, and five polycyclic aromatic hydrocarbons (PAHs) were analyzed for their chemical partitioning (K_D) to pristine, low-density polyethylene microplastic pellets. The calculated K_D values for the PAHs matched literature values and were seen to scale linearly with their literature hydrophobicity (log K_{OW}). For PPDQs, chemical partitioning was additionally

studied for weathered plastic and three sediments. Higher sorption consistently occurred for plastics over sediments, and to weathered plastics over non-weathered, pristine plastics. Plastic-PPDQ interactions are significant, particularly when plastics become weathered in the environment. Physicochemical properties at environmentally relevant concentrations for both legacy and emerging contaminants are provided here. Future work will proceed to characterize PPDQ desorption from sorbents such as sediments, plastics, and tire wear particles.

Chapter 4: Unique hepatic maternal transfer pattern of trace metals and perfluoroalkyl substances (PFAS) in a bluntnose sixgill shark (*Hexanchus griseus*)

In 2019, a pregnant bluntnose sixgill shark specimen washed ashore in Coles Bay on Vancouver Island, British Columbia and liver samples were collected. Preliminary work to analyze the livers for persistent organic pollutants (POPs) applied condensed phase membrane introduction mass spectrometry (CP-MIMS) using a triple quadrupole mass spectrometer (Agilent Technologies Inc. 7010B GC/MS/MS, Santa Clara, CA, USA) with a chemical ionization source. The instrumental workflow was identical to that detailed in **Chapter 2** with the following differences: 1) the solvent acceptor phase consisted of methanol (HPLC-grade, Fisher Chemical, Ottawa, ON, CAN), and 2) the MRM signals followed included an extended list of polycyclic aromatic hydrocarbon (PAH), phthalate, and polychlorinated biphenyl (PCB) compounds.

Subsamples of liver tissue (1.0 g) were homogenized and suspended in 40 mL of solvent. Both 2-propanol and methanol were used as extraction solvents, resulting in two sets of samples. The CP-MIMS probe was submerged in a sample solution until a steady-state signal was measured. The sample measurement was preceded and followed with a measurement of a pure solvent blank to collect signal baseline before and after sample analysis. When the 2-propanol experiment was analyzed, preliminary evidence of contaminants was observed. When the CP-MIMS probe was immersed in the sample solution, MRM transition signals corresponding with analytes which were present in solution increased, and the signal subsequently decreasing when the probe was returned to a pure 2-propanol solution (see **Figure 3.4.1A**). Despite this initial success, analysis with CP-MIMS proved challenging.

When comparing the rise time of analytes in the sample solution versus calibration standards prepared in the same solvent, a significant difference was observed. This is illustrated in **Figure 3.4.1A** for the MRM transition corresponding to $C_{14}H_{10}$ PAHs (e.g., anthracene, 179.0 → 178.0 *m/z*). Here, the signal rise time in the sample was 6× longer compared to anthracene standard solutions in 2-propanol which were measured in the same experimental run (**Figure 3.4.1A**). Similarly, the washout period for the anthracene signal was longer in the sample solution than in pure 2-propanol. Similar experiments run using methanol as the extraction solvent showed evidence of the same analytes, but fats from the sample were visually observed to bind to the PDMS membrane and once the CP-MIMS probe was submerged in pure methanol the signals did not return back to baseline (see **Figure 3.4.1B**). This was likely because, rather than analyzing the free concentration of analytes in solution, analytes were being extracted from the fats directly. The fats were more soluble in 2-propanol, but there were still larger rise times and washout periods. This could be due to interactions of lipids with the PDMS membrane, forming a fat-based polymer inclusion membrane,[112] or due to lower analyte partitioning between PDMS and the solvent/lipids mixture compared to PDMS and pure solvent.

Additionally, membrane extracts collected off-line showed potential evidence that the membrane is permeable to matrix components in the shark liver tissue. The CP-MIMS probe was submerged in a sample extract for an hour, during which the acceptor phase was collected. Examination of the collected acceptor phase revealed what appeared to be droplets of fat. This indicated that fats or proteins could cross the membrane which could be problematic for the instrument in the long-term. This observation in combination with the long rise times made rapid analysis of the tissue extracts untenable.

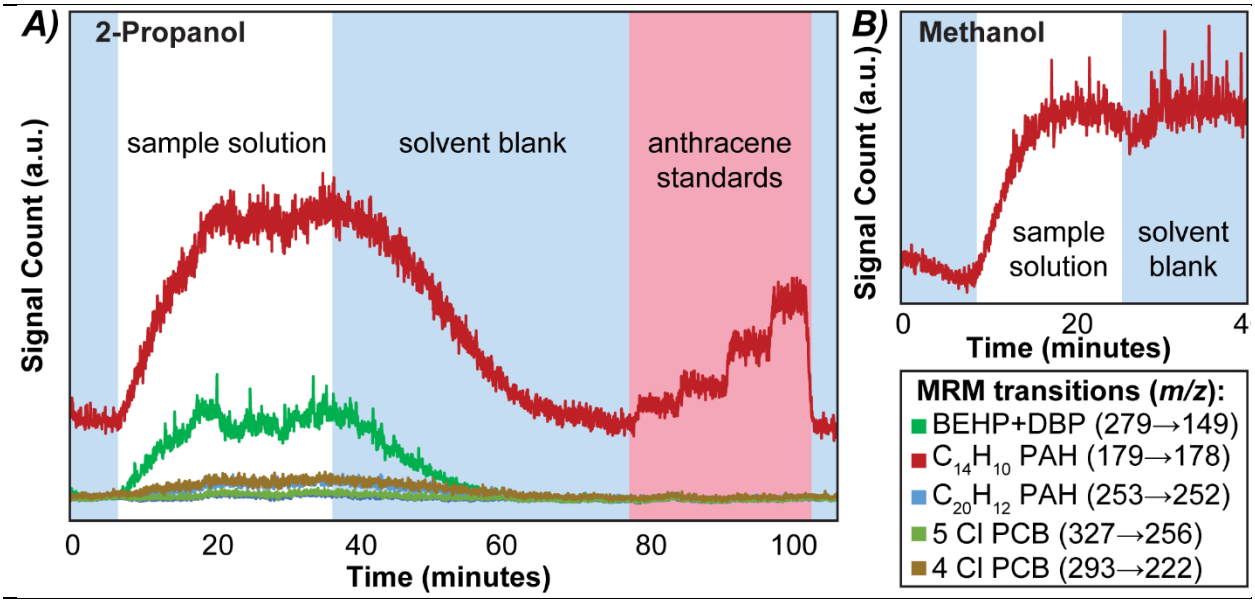

Figure 3.4.1. Chronogram of select MRM transitions in A) blank 2-propanol (IPA), switched to shark liver sample in IPA at *ca.* 5 min, switched to pure IPA solution to which four successive spikes of anthracene ($C_{14}H_{10}$, red) stock solution were added (*ca.* 80, 85, 90, 95 min), then switched to pure IPA (*ca*. 100 min), and B) blank methanol (MeOH) switched to shark liver sample in MeOH at *ca.* 7 min, and switched to pure MeOH at *ca.* 27 min. The MRM transitions followed included those associated with bis(2-ethylhexyl) phthalate (BEHP) and DBP (dibutyl phthalate*)*, the $C_{14}H_{10}$ PAH class (e.g., anthracene), the $C_{20}H_{12}$ PAH class (e.g., benzo[*a*]pyrene), and 4- and 5-chlorine polychlorinated biphenyls (PCBs).

This preliminary effort provided evidence of persistent organic pollutants in the liver of the sixgill shark, but it was clear that the analytes needed to be separated from the complicated liver matrix as much as possible. Additionally, persistent organic pollutants, such as PAH isomers, may be isobaric interferences while having different toxicities.[47] There is no chromatographic separation in CP-MIMS, so the specificity of isomer information is lost when using this technique without utilizing additional strategies such as selective chemical ionization.[47] Going forward, more conventional approaches to quantify contaminants, such as liquid chromatography mass spectrometry (LC-MS), were used. Analytes which did not have high affinities for lipids and consequently showed good recoveries after sample extraction were also prioritized.

The subsequent work is in the form that was submitted after revisions to Chemosphere and is included here with minor changes and permission from Misha Zvekic (conceptualization, methodology, validation, formal analysis, investigation, original draft writing, review and editing, and visualization), Holly V. Barrett (methodology, validation, review and editing, and investigation), Peter Diamente (methodology, resources, and supervision), Hui Peng (review and editing, resources, funding acquisition, and supervision), and Erik T. Krogh (conceptualization, review and editing, resources, project administration, funding acquisition, and supervision).

4.1 Introduction

Sharks are an ancient class of fish with diverse reproductive strategies.[113] Bluntnose sixgill sharks (*Hexanchus griseus*) are a yolk-sac viviparous species, growing eggs which then hatch internally with the resulting young undergoing live birth. No placental feeding occurs for sixgills which are fed via yolk sac, and thus the yolk is the only course of maternal provisioning.[114] Sixgills from the Mediterranean region were found to take up metal contamination,[115,116] which can have a negative impact on fish health.[117] Several classes of persistent organic pollutants (POPs) including polycyclic aromatic hydrocarbons (PAHs) and polychlorinated biphenyls (PCBs) have also previously been detected in the liver of a sixgill caught from the central Mediterranean Sea.[115] Additionally, polybrominated diphenyl ethers (PBDEs) were found in sixgills captured alive in Suruga Bay, Japan.[118] Bluntnose sixgill sharks have been classified as threatened or severely depleted in certain regions, near-threatened in the IUCN Red List of Threatened Species,[119] and a species of special concern in Canada under the Species at Risk Act (SARA) in 2009.[120] Quantifying a broader spectrum of contaminant concentrations in sixgills would increase our understanding of the potential risks of pollution to this species.

The metabolic function of the liver makes it a target for the accumulation of many contaminants including toxic metals,[121] which can then potentially be transferred from mother to offspring through maternal offloading processes.[122] Maternal transfer efficiencies of inorganic contaminants in yolk-sac fed viviparous sharks have been found to vary based on metal.[121] Maternal transfer is concerning as early life-stage animals are typically more sensitive to contaminants. However, the maternal transfer efficiencies of inorganic and organic contaminants in sixgills remain unknown.

Organic contaminants are bioaccumulated from the environment and transferred via different mechanisms compared to inorganic contaminants. In fish, perfluoroalkyl substances (PFAS) have been observed to accumulate in the liver relative to other organs,[123] possibly due to interactions with liver fatty acid binding proteins [8,124] and polar lipids.[125] PFAS are a diverse class of xenobiotic contaminants which have been linked to negative ecological and health impacts.[20,21] Despite regulations on PFAS production, these contaminants continue to persist in environmental compartments such as surface water and sediment,[123] as well as a wide variety of marine organisms.[126–129] The impacts of PFAS as a contaminant class and of individual PFAS compounds have not yet been fully characterized. However, PFAS are thought to interfere with evolutionarily conserved metabolic pathways,[123] which could result in toxicity effects in fish. Further, marine

organisms which accumulate PFAS could serve as an additional concentrated source to other organisms [130] and can reveal information about the presence of bioavailable PFAS in the region. Previous findings indicate that maternal transfer of PFAS in marine mammals is possible through placental and lactational routes.[127,129] Additionally, the muscle-muscle maternal transfer of POPs such as PFAS including perfluorocarboxylic acids (PFCAs) and perfluorosulfonic acids (PFSAs) was recently reported for yolk-sac viviparous tiger sharks collected from the Southwest Indian Ocean.[131] Briefly, PFCAs were found to accumulate to a greater extent than PFSAs in the muscle tissue of the embryos, increasing with carbon chain length. Sharks have very diverse physiological requirements and behaviours as well as reproductive strategies, consequently more work is required to understand maternal transfer trends in different shark species.

In February 2019, a bluntnose sixgill shark washed ashore dead from the Strait of Georgia in the Salish Sea (British Columbia, Canada), carrying 72 unborn full-term offspring. This specimen provided a unique opportunity to examine the fate and distribution of contaminants (both organic and inorganic) in a sexually mature sixgill shark inhabiting the deep waters of the Salish Sea, and to investigate the difference in contaminant load between mother and offspring. Based on previous studies on maternal transfer in other shark species,[131] it was hypothesized that maternal transfer of contaminant PFAS and metals could occur. However, the types of reproductive strategies in sharks are diverse, and sixgills provide maternal nutrition solely via a yolk-sac which potentially limits maternal transfer opportunities. Here, the concentration of 18 targeted inorganic elements and 21 targeted PFAS were analyzed in liver samples from the mother and offspring. To these authors' knowledge, contaminant loads in sixgills from the Salish Sea have not been previously reported. This work represents the first analysis of PFAS concentrations and mother-offspring maternal transmission in sixgill sharks.

4.2 Material and Methods

4.2.1 Sample Collection and Extraction

A deceased bluntnose sixgill shark was discovered in Coles Bay, Vancouver Island, BC, Canada on February 5th, 2019 (48.63028, −123.46635, **Figure 4.5.1**)**.** The specimen was 4 m long and pregnant with 72 offspring, one of which was found in the cloaca. A smaller subset of offspring (n = 8) was available for analysis. Samples of the maternal and offspring liver tissues were excised with a stainless-steel knife and stored in individual plastic bags at −20 °C until the time of analysis. When collecting subsamples of the livers, care was taken to excise tissue from the center of large (3 kg) subsections of the organ (mother) or the whole organ (offspring), discarding tissue that had been in contact with plastic. Extraction methods and subsampling strategies are summarized in more detail below and in the supporting information (**Figure 4.5.2**).

4.2.2 Chemicals and Reagents

Acid digestions for elemental analysis were carried out using 69.0–70.0% nitric acid (HNO_3) (Nitric Acid for Trace Metal Analysis, Thermo Scientific, Fisher, Ottawa, ON, CAN)

and 30% (w/w) hydrogen peroxide (H_2O_2) (Sigma Aldrich, St. Louis, MO, USA). Multi-element standard solution V for ICP (TraceCERT®, Fluka, Sigma Aldrich) was used for standard additions, direct calibration curves, and for quality control (**Table 4.5.1**). Dogfish liver Certified Reference Material DOLT-5 (National Research Council Canada, Ottawa, ON, CAN) was used as a certified reference material (CRM) for method validation (**Table 4.5.2**). For the defatting step described in the supporting information, ACS-grade dichloromethane (VWR, Mississauga, ON, CAN) was used. Ultra-pure water (18 MΩ cm, Facility Scale Reverse Osmosis/Ion Exchange Water Purification System, Applied Membranes Inc., Vista, CA, USA) was used for dilutions. For PFAS analysis, 21 native PFAS (PFAC-MXC) and 13 isotopically-labeled standards (MPFAC-MXA) were purchased from Wellington Laboratories (Guelph, ON, CAN; **Table 4.5.3** and **Table 4.5.4**). HPLC-grade methanol and acetonitrile were obtained from Fisher Scientific.

4.2.3 Quality Assurance/Quality Control

For elemental analysis, deionized (DI) water was run before and after calibration curves and samples to flush out the lines and to monitor for any carryover effects. Procedural digestion blanks were used to background subtract the samples. The 7–8-point standard additions used for quantification had a concentration range from 6–310 μg L^{-1} or 60–3100 μg L^{-1}, depending on the element. The same concentration ranges were used to build direct calibration curves in DI water to estimate the sample detection limits (**Table 4.5.1**). The percent bias for the method (**Table 4.5.2**) was found by digesting 0.5 g of CRM. Spiked (50 or 500 μg L^{-1}) and unspiked digests were used to calculate percent recoveries. Only analytes and wavelengths which behaved reproducibly, provided linear response within standard additions, and had good recoveries (80–120%) were reported (**Table 4.5.1**). The measurement relative standard deviation (RSD) from the ICP was *ca*. 1% for all elements reported here. To investigate variation in the extraction method versus variation due to sample heterogeneity, the same offspring specimen (n = 1) was digested and analyzed in triplicate. The resulting concentrations detected (**Table 4.5.5**) had lower relative standard deviations (3× smaller RSD on average) compared to when all (n = 8) offspring sharks were compared. This indicates that variance in concentration was predominantly due to heterogeneity between samples.

An 8-point multi-component methanolic calibration curve of the native PFAS at concentrations ranging from 1–64 μg L^{-1} was used for quantification. The relative response of each native PFAS against their corresponding isotopically-labeled internal standard (10 μg L^{-1}) was plotted against the concentration. Strong linearity ($R^2 > 0.984$ (**Table 4.5.3**) was observed for all PFAS. Mean recoveries across samples were determined using isotopically-labeled PFAS, which ranged from 104 ± 21% ($^{13}C_4$-PFBA) to 160 ± 31% ($^{13}C_2$-PFDA) (**Table 4.5.4**). To monitor carryover, methanol injections occurred after every 5 samples. To monitor stability, 8 μg L^{-1} of combined standards were injected every 5 samples.

4.2.4 Instrumental Analysis

Sample extraction of inorganic elements and subsequent analysis with an inductively coupled plasma optical emission spectroscopy (ICP-OES) instrument is detailed in the supporting information. Four separate subsections of the mother's liver and eight individual offspring livers were digested and quantified by standard additions (**Figure 4.5.3**). Details on how metal concentrations were quantified are summarized in the supporting information and are reported in dry weight. Each standard addition analysis was done once per offspring or mother sample.

Sample extraction of PFAS and subsequent analysis with liquid chromatography-electrospray ionization-high resolution mass spectrometry (LC-ESI-Orbitrap) is detailed in the supporting information. Each of the five offspring sharks were extracted in triplicate. Two separate subsections of the adult female shark were each extracted in triplicate, along with a composite sample wherein three separate subsections were mixed in equal mass portions prior to homogenization. The concentration of PFOS was found to be an outlier via the Grubb's test for one replicate of one of the adult female subsections. That replicate was thus rejected and not included in the analysis. Details on how the PFAS concentrations were quantified are summarized in the supporting information and reported in wet weight.

4.2.5 Bioconcentration and Maternal Transfer

To compare the concentrations in the organism and in the environment, bioconcentration factors (BCFs) were estimated using **Equation 4.1** [132] and historical water concentrations of the Strait of Georgia obtained from literature [133] (**Table 4.5.6**):

$$BCF = \frac{[Contaminant]_{organism}}{[Contaminant]_{aquatic\ environment}} \qquad \textbf{(Equation 4.1)}$$

The maternal transfer ratio (MTR) was calculated by dividing the mean concentration of contaminants in the offspring's liver by the mean concentration of contaminants in the mother's liver (**Equation 4.2**). In the event where a contaminant was not detected in the mother, the limit of detection concentration is used to calculate the lower bound of maternal transfer. Information on uncertainty estimates is detailed in the supporting information.

$$MTR = \frac{[Contaminant]_{offspring}}{[Contaminant]_{mother}} \qquad \textbf{(Equation 4.2)}$$

4.3 Results and Discussion

4.3.1 Inorganic elements with ICP-OES

The distribution of metals in the Strait of Georgia differs from other water bodies due to both the natural variation of metal abundances as well as potential anthropogenic inputs from adjacent mining and other activities in the area.[133] The Strait of Georgia receives input from nutrient-rich Pacific waters upwelling, the bulk of which remains in the deep waters (>200 m) where sixgills dwell.[134] The levels to which elements accumulate in

an organism is related to diet, physiology, and metabolic behaviour as well as the element's environmental abundance and intrinsic chemical properties.[6] Some elements (e.g., calcium, magnesium) are biologically necessary,[135] whereas many other elements are essential at trace levels and toxic at elevated concentrations (e.g., copper, zinc),[117] or non-essential and harmful at any concentration (e.g., cadmium, lead).[132] The distribution and concentration of different inorganic elements, both essential and toxic, can vary over an organism's lifespan.[136] The concentration of macro- and microelements were analyzed in a sixgill which dwelled in the Strait of Georgia as well as the offspring, allowing us to use the sixgill to probe the bio-concentration of contaminants in the region as well as maternal-offspring transfer.

In the adult shark, elemental concentrations ranged from high (>400 mg kg^{-1} dw) to low (<1 mg kg^{-1} dw) levels within the sample. Eighteen elements were analyzed in four sub-sections of maternal liver and one liver subsection in eight separate offspring. Of these, four elements (Ag, Ba, Be, Bi, and V, **Table 4.5.1**) were below our detection limits in all samples. The concentrations of the remaining 14 elements are represented as boxplots in **Figure 4.3.1** and as mean values in **Table 4.5.7**. Iron had the highest concentration in the maternal liver and was sixteen times more concentrated than calcium, which was the second most concentrated element measured. Copper, zinc, magnesium, zinc, and calcium ranged from concentrations of 11–25 mg kg^{-1} dw. The elements present at the lowest detectable levels (1–10 mg kg^{-1} dw) included manganese, chromium, cobalt nickel, molybdenum, cadmium, and lead. In the offspring, most metals were detected at lower concentrations compared to the mother (see **Figure 4.3.1**), with manganese being below detectable limits. Most elements were present at low (*ca.* ≤5 mg kg^{-1} dw) levels, including iron, zinc, lead, molybdenum, chromium, cobalt, nickel, and cadmium. Levels of copper, magnesium, and calcium in the offspring ranged from 10–34 mg kg^{-1} dw and were similar to the mid-range concentrations detected in the adult shark.

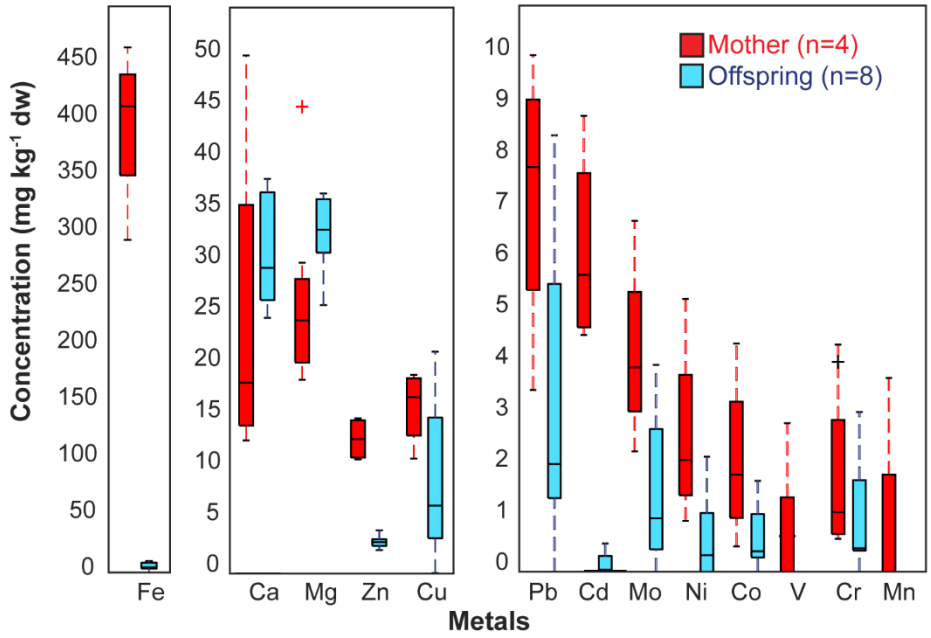

Figure 4.3.1. Boxplots representing metal concentrations (in mg kg^{-1} dry weight (dw)) in four subsections of the mother's liver (dark red) and in eight separate pup livers (light blue) boxplots. Detection limits are reported in **Table 4.5.1**.

Bioconcentration of both essential and toxic elements occurs in the liver tissue of marine organisms.[121] Limited information exists on the concentrations of metals available at the depths that the sixgill and its prey items dwell. However, when comparing our specimen to the average metal concentrations in the Strait of Georgia recorded in a 1983 review paper,[133] the calculated bioconcentration factors (BCFs) revealed that the concentration of elements in the liver were orders of magnitude (10^2–10^6) greater relative to the water column (**Table 4.5.6**). The calculations here are based on one specimen and historical concentration data, so these authors caution against generalizing these preliminary findings.

Few studies have examined elemental concentrations in adult sixgill sharks, and the findings suggest that elemental variation is influenced by the region that the sharks were found. In 2019, a deceased mature sixgill was found in the central Mediterranean Sea (Strait of Messina).[115] Comparing the concentrations detected in our sample from the Strait of Georgia (SoG) to the shark collected from the Strait of Messina (SoM) revealed some variation in elemental concentrations (**Table 4.3.1**). The mean concentrations of some elements were comparable in both specimens (Ca, Mn, Cu) while others were lower (Zn, Mg) or higher (Fe, Cr, Cd, Pb, Co, Ni, Mo) in the SoG shark compared to the SoM specimen. For toxic metals, greater concentrations in the SoG shark were observed compared to the SoM shark, with cadmium and lead being 5–10-fold greater, respectively. Cadmium is present at naturally elevated levels in the Strait of Georgia due to upwelling from the

Pacific Ocean, and anthropogenic inputs are thought to be minimal.[137] Nonetheless, this metal has historically contaminated marine organisms such as oysters in the region.[138]

Comparing sixgill specimens found in similar regions indicates that sixgills have some natural variation in elemental concentrations (**Table 4.3.1**). Concentrations of cadmium and iron and were similar in Mediterranean sixgills analyzed in 2019 [115] and 1993,[116] while the concentrations of copper and zinc were 2–3-fold greater in the 2019 specimen. The comparisons made here are limited due to paucity of available data and variations between different sixgills including diet, age, and sex of the specimen.[131] While both the 2019 SoG and SoM sharks were determined to be sexually mature, neither shark was aged and the SoM sharks were not sexed. Further research expanding the dataset is required to draw more generalized conclusions about elemental bioaccumulation trends and differences between regions, time periods, and individual sixgill specimens.

The inter-sample variation in metal concentration was observed in **Figure 4.3.1** in multiple liver subsections of the adult and between the liver samples of different offspring. Intra- and inter-sample variation for metal concentrations was further quantified for the offspring in **Table 4.5.5**. The heterogeneity in the adult was likely due to the size of the liver, and this variation was captured by digesting and extracting separate subsections of the liver sample.

Table 4.3.1: Summary of metal concentrations in sixgill sharks

Location	Mediterranean Sea		Strait of Georgia
Substrate	Adult Sixgill Liver (mg kg^{-1} ww)	Adult Sixgill Liver (mg kg^{-1} dw)	Adult Sixgill Liver (mg kg^{-1} dw) [a]
Year	1993 [116]	2019 [115]	2019 Present Study
Ca	—	24.1 ± 0.7	25 ± 17
Mn	1.21	0.67 ± 0.05	0.9 ± 1.9
Fe	79.3	70 ± 4	395 ± 72
Zn	15	26.5 ± 1.0	13.1 ± 2.1
Cr	—	0.068 ± 0.01	1.8 ± 1.8
Co	—	0.057 ± 0.007	2.2 ± 1.7
Ni	—	0.28 ± 0.02	2.7 ± 1.9
Cu	4.38	11.7 ± 0.8	16.2 ± 3.7
Mo	—	1.6 ± 0.3	4.3 ± 1.9
Cd	1.06	1.14 ± 0.09	6.3 ± 2.0
Pb	—	0.68 ± 0.07	7.3 ± 2.8

[a] Uncertainty estimates based on heterogeneity of results from different liver subsamples.

4.3.2 PFAS with LC-ESI-Orbitrap

The North Pacific Ocean was reported to have a diverse PFAS profile and the second greatest summed PFAS concentration after the Indian Ocean.[123] PFAS detected in North Pacific water, sediment, and plankton include perfluorocarboxylic acids (PFCAs; C_4–C_{11} with notably high levels of PFOA) and perfluorosulfonic acids (PFSA; C_4, C_6–C_8).[123,139] It has been proposed that fatty acid binding proteins enable PFAS to concentrate in liver tissue,[8] and recently PFAS was detected in the livers of aquatic species.[123,126,129] The hepatic PFAS concentrations in the mother and offspring were measured and the results are represented as boxplots in **Figure 4.3.2** and summarized in **Table 4.5.8**.

The only PFAS present above detectable limits in the adult sixgill liver was a PFSA, perfluorooctanesulfonic acid (PFOS) at 13 ± 9 ng g^{-1} ww (median 7 ng g^{-1} ww). The carboxylated PFCAs being below the limit of detection in the adult shark was unexpected. There are greater concentrations of PFOA than PFOS in the North Pacific Ocean,[123] but PFOA was not detected in any of our specimens. PFSAs have been found to demonstrate greater protein [123] and phospholipid [125] binding affinities than PFCAs of the same chain length. However, the few studies measuring PFAS in sharks performed to date differ from our findings – measuring PFCAs, albeit at lower concentrations than our detection limits, at higher levels than PFOS.[131,140] These studies indicate larger bioaccumulation of PFCAs relative to PFOS in adult sharks. These studies were performed on tiger sharks (*Galeocerdo cuvier)* and bull sharks (*Carcharhinus leucas*) collected off the West coast of Reunion Island in the Indian Ocean,[131] and blue sharks (*Prionace glauca*) in the North Atlantic Ocean.[140] Analysis revealed that there were lower concentrations of PFAS in the aplacental viviparous tiger sharks (Σ_7PFAS 0.144 ± 0.053 ng g^{-1} ww) relative to placental viviparous bull sharks [131] and blue sharks.[140] The highest concentrations of PFAS in shark liver was detected in the North Atlantic blue shark study (Σ_7PFAS 12 ± 6 ng g^{-1} lipid weight (lw) (PFOS, PFHxA, PFOA, PFNA, PFDA, PFUnDA, and PFDoDA)) [140] with a similar magnitude as our sixgill specimen (Σ_7PFAS 13 ± 9 ng g^{-1} ww (PFOS, all others were below LOD)). These levels were considerably greater than those found in the muscle tissue of the Indian Ocean specimens (Σ_7PFAS 0.5 ng g^{-1} ww (PFOS, PFNA PFDA, PFUnDA, PFDoDA, PFTrDA, and PFTeDA)).[131] Comparatively, the loadings in the adult shark analyzed in the present study appear relatively high. The non-detectable levels of PFCAs in our adult specimen indicates that PFSAs and PFCAs either do not bioaccumulate in the liver with the same efficiency, or that the behaviour and fate of these compounds in sixgill sharks differs, particularly in the event of maternal transfer.

In contrast to the adult, the number and concentration of PFAS compounds detected in the offspring sixgills were significantly greater. Seven of the PFAS compounds were present above the limit of detection (**Table 4.5.8**) and were predominantly perfluorocarboxylic acids (PFCAs) ranging from C_9–C_{14} chain length. Mean values of PFCAs in the offspring as ng g^{-1} ww were 1.3 ± 0.4 PFNA (C_9), 2.7 ± 0.4 PFDA (C_{10}), 20 ± 3 PFUnDA (C_{11}), 2.8 ± 0.7 PFDoDA (C_{12}), 26 ± 4 PFTrDA (C_{13}), and 3.2 ± 0.9 PFTeDA (C_{14}). The only detected PFSA was PFOS (C_8), present at 16 ± 2 ng g^{-1} ww (median 16 ng g^{-1} ww) in the

offspring. As seen in **Figure 4.3.2**, the total summed PFAS median concentration in the five offspring was roughly ten-fold greater than in the mother.

Examining the properties of the PFCAs accumulated in the offspring, there was a prevalence of long fluorocarbon chain length (≥C_9) PFCAs at concentrations ranging from 1.5 ± 0.5 ng g^{-1} ww PFNA (C_9) to 26 ± 4 ng g^{-1} ww PFTrDA (C_{13}) (**Figure 4.3.2**). This was consistent with previous results finding stronger affinity of longer-chain PFCAs to tissue proteins and lipids.[8] In general, odd-chain length PFCAs [PFUnDA (C_{11}), PFTrDA (C_{13})] were observed to be present at greater concentrations ($\sum_2$PFAS 46 ± 7 ng g^{-1} ww) compared to even-chain length PFCAs [PFDA (C_{10}), PFDoDa (C_{12}), PFTeDa (C_{14})] ($\sum_3$PFAS 9 ± 2 ng g^{-1} ww). This phenomenon has previously been observed in marine fish, including sharks, and is attributed to the greater atmospheric and microbial degradation and metabolism of even-chain length PFCAs to fluorotelomer alcohols.[123,131] In the offspring, there was lower levels of PFOS than ∑PFCAs, consistent with trends observed in adult sharks in previous studies.[131,140] This may be due to efficient maternal transfer of different types of PFAS, and not necessarily the efficiency of bioaccumulation. Due to the more similar structure of PFCAs to fatty acids, an unknown active transport mechanism for endogenous fatty acids might be employed to transport PFCAs. Future studies are warranted to clarify the exact biochemical mechanism of PFCAs accumulation and transfer in sixgill sharks.

Shark species previously analyzed have had PFAS levels which exceed the levels detected in our adult specimen, but not the levels accumulated in the offspring.[131,140] The contaminants become concentrated in the offspring's liver which had a volume many times smaller than the adult's liver until the offspring finishes maturing. However, the high PFAS concentrations measured in the sixgill offspring relative to offspring from previous studies are especially notable due to the vulnerability of young organisms.[131,141] The same PFAS were detected in tiger shark and bull shark embryos from the Chynel *et al*. study as were detected in the offspring sixgill in our present study (Σ_6PFCAs = 56 ± 9 ng g^{-1} ww sixgill sharks), but at much lower levels (Σ_6PFCAs = 1.3 ± 0.3 ng g^{-1} ww tiger sharks, 0.177 ± 0.02 ng g^{-1} ww bull sharks).[131] The only PFSA above LOD in the these studies was PFOS, which was also present at lower levels in sharks analyzed in previous studies [131,140] compared to the adult and offspring sixgill here. Our findings indicate our sixgill accumulated significant amounts of PFOS, along with six PFCAs, which it subsequently transferred to its offspring.

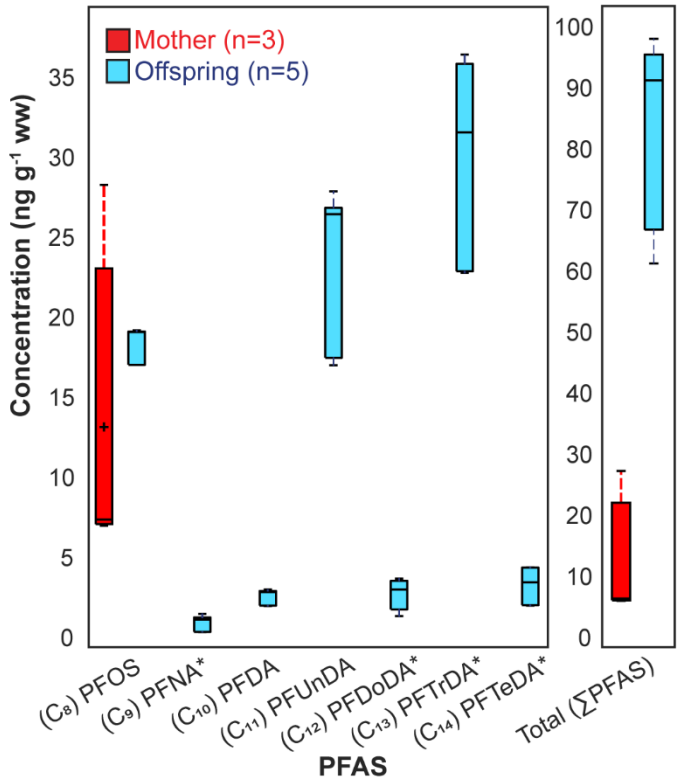

Figure 4.3.2. Boxplots representing the concentrations (ng g^{-1} wet weight (ww)) of PFSAs (PFOS) and PFCAs (PFNA, PFDA, PFUnDA, PFDoDA, PFTrDA, and PFTeDA) in order of increasing chain length along with the summed total of PFAS in the mother (dark red, n = 2 separate liver extracts and 1 composite sample of 3 separate liver extracts) and offspring (light blue, n = 5). Detection limits are reported in **Table 4.5.8**.

4.3.3 Maternal transfer

Maternal transfer is the process whereby substances including contaminants are passed to offspring. In mammals, this is generally associated with transfer through the placenta or the high lipid and protein content of breast milk.[127,128] While shark reproduction strategies are diverse, some sharks have been found to passively transfer contaminants to their offspring.[122] The mobilization of lipids from the liver to the developing yolk sac in vitellogenesis is thought to transfer concentrated lipophilic POPs in sharks.[122] In contrast to typical POPs, PFAS and inorganic elements are not thought to have high affinity for most fats.[121,142] However, they both have been observed to concentrate in liver tissue.[121,126] Here, the liver lipid content was determined to be similar in both mother and offspring (57 ± 8% and 55 ± 3%, respectively, **Table 4.5.8**), so the concentrations were not normalized by lipid content when estimating the maternal transfer ratios. While this single specimen gave us a unique opportunity to study maternal transfer, these authors caution against overgeneralization.

To characterize maternal transfer, the ratio of the mean concentration values in the subset of the offspring analyzed relative to that in the mother were calculated (**Figure 4.3.3**). With the exception of the macronutrients calcium and magnesium, the metals were observed to be higher in the mother than the offspring, leading to maternal transfer ratios (MTRs) of less than 1. Despite the relatively large variation within mother and offspring samples suggesting heterogeneity within these samples, several trends emerge. Copper and chromium had MTRs ~0.6 ± 0.1, and molybdenum, lead, and strontium had MTRs ~0.4 ± 0.1, while cobalt, nickel, and zinc had MTRs ~0.3 ± 0.1. Interestingly, the MTRs for cadmium and iron were well below 0.1 indicating minimal maternal transfer. Manganese was not detected in the offspring samples, so the MTR reported represents an upper limit. Some elements (Ag, Ba, Be, Bi, and V) were not detected in either mother or offspring.

Previous studies comparing maternal transfer of metals in placental viviparous sharks have found the concentration of metals such as iron, zinc, cobalt, and copper to be higher in concentration in the offspring than the mother,[141,143] which was not observed in our aplacental, yolk-sac viviparous sixgill specimen. These elements, which are all biologically necessary at certain levels,[117] had MTRs of less than 1 in the current study. MTRs ≥1 were observed for calcium and magnesium (**Figure 4.3.3**), which is different than the MTRs observed in a placental viviparous shark.[143] Low maternal transfer efficiency was also observed for toxic elements. Lead and cadmium are both toxic to fish, causing immunotoxicity and neurotoxicity as well as oxidative stress, respectively.[144,145] The MTR of lead was < 0.5 and cadmium had one of the lowest MTRs of the elements investigated here (0.025). Despite the low MTRs for metals, it is likely that the mass of toxic elements offloaded from the mother to the offspring is significant given the relatively high fecundity of this species. However, the low MTRs for essential elements may pose a challenge for the young sharks. While metal homeostasis in the liver is predominantly governed by metal-binding proteins (e.g., metallothionein),[146] these proteins were not analyzed here.

Concentrations of the essential element iron [132] in the mother was observed to be 70-fold higher than the offspring, resulting in an MTR of 0.014 ± 0.009 (**Figure 4.3.3**). The vast difference in the concentration of iron between mother and offspring may indicate that the unborn sixgills were deficient, but confirmation would require knowledge of the baseline embryonic levels of this species. One previous study on an yolk-sac viviparous ray [147] showed a similar, low MTR (0.09 ± 0.08) for iron. All other previous studies performed on related species have found the MTR of iron to be equal to or greater than 1, including in placental viviparous sharks,[141,143,148] an aplacental viviparous shark which employs oophagy,[135] a yolk-sac viviparous ray employing histotrophy,[149] and a yolk-sac viviparous dogfish.[150] These studies predominantly compared muscle-muscle maternal transfer. Comparing yolk-sac viviparous sharks to placental viviparous sharks, there are limited studies on and fewer opportunities for maternal transfer. In the sixgill, the only route of maternal transfer is via the yolk sac, whereas other sharks may have additional elemental inputs via the development of a placenta. In yolk-sac viviparous sharks, some essential elements will not significantly accumulate until they are born and begin consuming other organisms. Overall, the level of iron and other essential elements varies drastically among

different species of sharks and rays, and due to the diversity of reproductive strategies the maternal transfer ratio also varies.[113]

In contrast to the inorganic elements, PFAS were efficiently transferred from the mother's liver to the offspring. The ∑PFAS quantified in this study was on average ~70 ng g^{-1} in the offspring and ~13 ng g^{-1} in the adult, leading to an overall MTR of at least 6. Predominantly, the PFAS compounds detected in the offspring were perfluorocarboxylic acids which were not detected in the mother. Using the LOD values in **Equation 4.2**, the lower bound for the maternal transfer ratios ranged from 1.3 ± 0.4 to 89 ± 15 for PFNA (C_9) and PFUnDA (C_{11}), respectively. It should be noted that given the concentration of PFCAs may have been lower than the LOD, the MTRs may actually be considerably higher. The only PFAS which was detected in both mother and offspring was PFOS which had an MTR of 1.3 ± 1.0. Other than PFOS, there were no PFSAs detected in the mother or offspring liver. Overall, the maternal transfer of PFCAs appear to be significantly greater compared to the maternal transfer of PFSAs.

When comparing the maternal transfer efficiencies of the species reported by Chynel *et al.* and our sixgill in **Table 4.5.9**, it is evident that aplacental yolk-sac viviparous species (tiger shark and sixgill shark) have greater maternal contaminant transfer efficiency (∑PFCAs MTR is 23 and 13, respectively) than the placental viviparous bull shark (∑PFCAs MTR 0.7).[131] The only exception was PFOS which had an MTR of 2.9 in the bull shark and ~1 in the sixgill and the tiger shark (**Table 4.5.9**). Notably, tiger sharks were recently determined to have an additional maternal nutrition input by consuming nutrient-rich uterine fluid produced by the mother.[151] The differing maternal transfer efficiencies for PFAS between sharks that demonstrate different embryonic nutritional strategies suggests a possible difference in the maternal transfer mechanism. Overall, there were higher concentrations of PFAS in our sixgill (∑PFAS ~70 ng g^{-1} offspring, ~13 ng g^{-1} adult) compared to the tiger sharks (∑PFAS <2 ng g^{-1} offspring, <0.3 ng g^{-1} adult).[131]

Previous studies found that MTRs for metals and PFAS in placental viviparous sharks were ≥1. This stands in contrast to the yolk-sac viviparous sixgill which had MTRs that were predominantly less than 1 for metals and greater than 1 for PFAS, especially for PFCAs. It is likely that the transfer mechanism of metals and PFAS differ, with PFAS likely being transported with a more active mechanism such as mobilization of proteins during vitellogenesis.[8] The protein vitellogenin, a key component of the yolk, is synthesized in the liver.[152] Here, the maternal transfer potential of PFAS is much greater than the transfer of inorganic contaminants, however the absolute amount of PFAS being transferred is much lower (μg kg^{-1} PFAS, mg kg^{-1} metals). There is some evidence of maternal transfer of PFAS and inorganic elements in humans.[153,154] Understanding specific transport mechanisms in different organisms continues to be an active area of research.

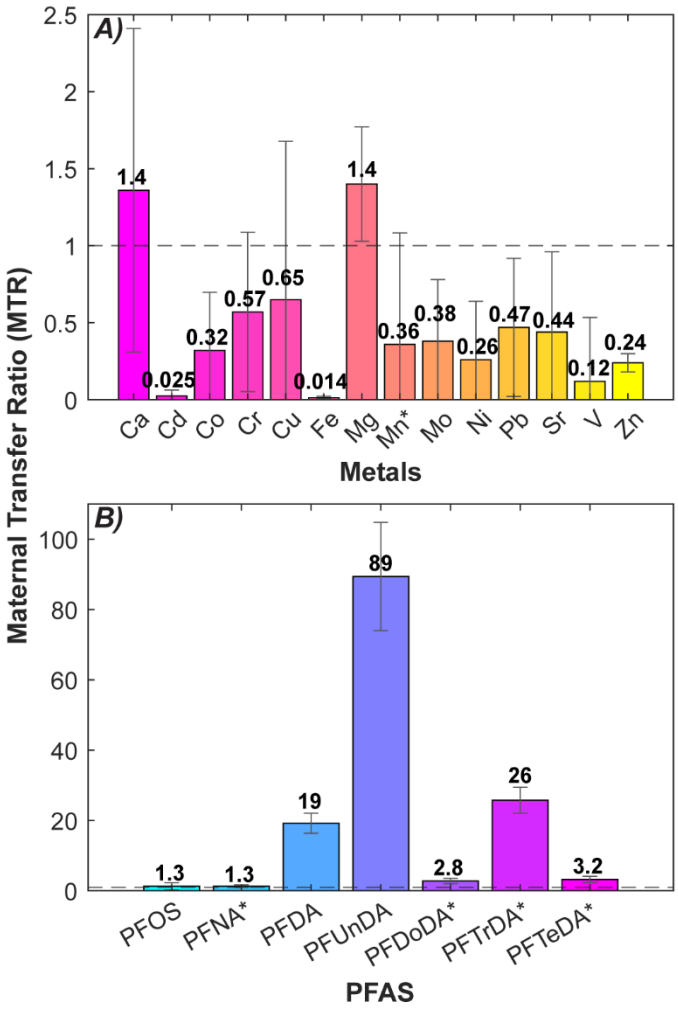

Figure 4.3.3. Maternal transfer ratio (MTR) comparing the mean concentration of A) inorganic elements and B) PFAS between the offspring and the mother. The dashed line represents an MTR of 1. Values greater than 1 indicate maternal transfer, while values below 1 indicate that the concentration is higher in the mother than the offspring. MTRs for PFAS not detected in the mother (denoted by *) are represented as a lower limit using the method detection limit concentration. Error bars represent the propagated absolute error.

4.4 Conclusion

The concentration and maternal transfer ratios of select metals and perfluoroalkyl substances are reported in liver samples from a pregnant bluntnose sixgill shark specimen from the Pacific Coast of British Columbia, Canada. The concentrations of toxic metals such as lead (7 ± 3 mg kg^{-1} dw) and cadmium (6 ± 2 mg kg^{-1} dw) were higher in the mother than the unborn offspring. In contrast, PFAS appear to have been offloaded to the offspring ($\sum_7$ PFAS 71 ± 9 ng g^{-1} ww) and were dominated by perfluorocarboxylic acids over perfluorosulfonic acids. These findings suggest that there are unique maternal contaminant transfer mechanisms through the yolk sac of the sixgill shark.

4.5 Supporting Information

4.5.1 Analysis of inorganic elements with ICP-OES

Liver subsamples were homogenized with a ceramic knife on a plastic cutting board, transferred to a plastic weigh boat and dried in an oven (Isotemp 100L Oven Gravty, Thermo Fisher Scientific, Pittsburgh, PA, USA) at 55 °C for three days. The dried tissue was crushed into a paste with a ceramic mortar and pestle, and 1 g of sample was transferred to a 75 mL glass digestion tube. 10 mL of concentrated nitric acid was added and the digest tube was covered with a watch glass. The acid and sample were allowed to equilibrate at ambient temperature (~20 °C) for one hour, then samples were placed on a heating block (AD-4020 Pulse Instrumentation Ltd, Saskatoon, SA, CAN) and digested at 100 °C for 120 minutes. Samples were cooled to room temperature, then 4 mL of hydrogen peroxide was added, and left to equilibrate for one hour at ambient conditions, before being placed on the heating block at 95 °C for an additional hour. Afterwards, the samples were cooled to room temperature, diluted with DI water to 75.0 mL, and transferred to 125 mL plastic Nalgene® bottles and stored at 4 °C. Prior to analysis, a liquid-liquid defatting step with 1/3 *v/v* dichloromethane/digest sample was performed. The resulting acidic aqueous layer was analyzed using a 7–8-point gravimetric multi-component standard addition calibration. Multi-component standard additions were spiked on top of 5 g of the aqueous sample digest and each standard solution was diluted to a total of 6 g with deionized (DI) water.

An Inductively Coupled Plasma Optical Emission Spectrometer (iCAP6200, Serial Number IC2D20120715, Thermo Scientific, England, UK) coupled to an ASX-520 Autosampler (CETAC Technologies, Omaha, NE, USA) was used for analysis. The nebulizer gas was argon (99.999% purity, Praxair, Mississauga, ON, CAN) flowing at 1.0 mL min^{-1} at a pressure of 20 PSI (138 kPa). Analysis was run in duplicate in axial and radial mode with an analysis integration time of 5 seconds each and a 30 second flush time between samples. The high fat content in the digest samples was found to cause sample line clogging which resulted in inconsistent nebulization. An additional defatting step was thus employed to separate the lipids from the aqueous solution to be analyzed. Additionally, a rinse solution consisting of 0.01 % Triton X-100 (Sigma-Aldrich, St. Louis, MO, USA) and 0.5 % HNO_3 was used between samples. After each run on the ICP-OES, the ICP torch was extinguished and 10 mL of warm 2-propanol (ACS Grade, Anachemia, VWR, Mississauga, ON, CAN) and hot DI water (heated for 60 seconds in a commercial microwave oven), were flushed through the instrument lines and nebulizer to wash out any organic matter that may have been deposited in the system.

4.5.2 Analysis of PFAS with LC-ESI-Orbitrap

Approximately 1 g of shark liver tissue was homogenized in a 15 mL Falcon tube (FroggaBio, Concord, Ontario, CAN) with stainless-steel scissors and extracted based on a previously established method.[129] Scissors were rinsed with methanol and DI water between samples. A suite of 13 isotopically-labelled PFAS standards (20 µL of 500 µg L^{-1}) were added to the liver samples and procedural blanks. Briefly, 5 mL of acetonitrile was added to the Falcon tubes which were then capped and vortexed (Vortex Genie 2®, Fisher

Scientific, Ottawa, Ontario, CAN) for 60 s, sonicated (Bransonic® Ultrasonic Cleaner, Branson Ultrasonics Corporation, Danbury, Connecticut, USA) for 30 min, and centrifuged (Sorvall Legend XTR centrifuge, Thermo Scientific, Waltham, Massachusetts, United States) at 4,000 × g for 10 min. The acetonitrile extraction was repeated a second time, and the supernatants were combined in a new Falcon tube and evaporated to dryness under nitrogen gas. The remaining lipid residue was weighed to gravimetrically determine the total lipid content of the sample. To remove the lipids, an acetonitrile freeze-out was employed whereby 2 mL of acetonitrile was added to the lipid layer which was then vortexed for 60 s to create a pseudo-emulsion. The mixture was then placed in a −20 °C freezer for the lipids to freeze-out overnight. The following day, the supernatant was decanted into a new Falcon tube. This process was repeated using another 2 mL aliquot of acetonitrile, vortex mixing, and 1 h in a −20 °C freezer before decanting the supernatant. The supernatants were combined and dried under nitrogen gas, and ultimately reconstituted in 1 mL of methanol.

1 µL of each liver extract was injected onto a C18 column (Hypersil GOLD, 1.5 µm, 2.1 × 50 mm; Thermo Fisher Scientific) and analyzed with a Vanquish ultrahigh-performance liquid chromatography (UHPLC) system coupled to a Q-Exactive high-resolution mass spectrometer (Thermo Fisher Scientific). A guard column (Halo® C18 3.0 × 100 mm, 2.7 µm; Advanced Materials Technology) was employed before the injection loop to minimize interference from PFAS in the background of the instrument (i.e., PFOS and PFOA). The autosampler and column compartments were maintained at 10 and 40 °C, respectively. The mobile phases were A) 5 mM ammonium acetate and 0.1% formic acid in DI water and B) 5 mM ammonium acetate and 0.1% formic acid in methanol. A 15-minute gradient elution was as follows: B was increased from 20% to 80% from 0 to 3 min, then to 100% between 3 and 5 min, and decreased from 100% to 20% across 9 to 10 min, and remained at 20% for the remaining 5 min to ensure mobile phase equilibration before beginning the next chromatographic run. Data were collected in negative mode ESI. The mass spectrometric settings were as follows: spray voltage 2.7 kV, sheath gas flow rate 30 L h^{-1}, auxiliary gas flow rate 6 L h^{-1}, auxiliary gas heater temperature 300 °C, and capillary temperature 300 °C. Targeted analysis used the peak areas corresponding with the retention times and exact masses of analytes (listed in **Table 4.5.3**).

4.5.3 Data analysis and uncertainties

To quantify analyte concentrations, the sample signal was first background subtracted using the procedural digest blank signal. The concentration of metals in the shark liver was found using the method of standard additions, adjusting for the volume of dilution and mass of sample digested (see **Equation 4.3**). The concentration of PFAS was found using a direct calibration curve and adjusting for the mass of liver extracted and the volume of methanol that the extract was reconstituted in (see **Equation 4.4**).

$$Conc_{metals} = \frac{y_{0_{standard\ additions}}}{m_{standard\ additions}\left(\frac{kg}{\mu g}\right)} \times \frac{mass_{digest\ subsample\ +\ DI}\ (g)}{mass_{digest\ subsample}\ (g)} \times \frac{volume_{digest}\ (75.0\ g)}{mass_{liver\ extracted}\ (g)} \times \frac{1\ mg}{1000\ \mu g}$$

(**Equation 4.3**)

$$Conc_{PFAS} = \frac{signal - y_{0_{calibration\ curve}}}{m_{calibration\ curve}\ (ppb^{-1})} \times \frac{volume_{methanol}}{mass_{liver\ extracted}} \quad \textbf{(Equation 4.4)}$$

Detection limits were calculated based on 3 × standard deviation of sample blanks / slope of a 7–8-point direct calibration curve. For LC-MS analysis, there was no signal present in the blanks for some analytes. In this case, the limit of detection (LOD) was measured as the lowest calibration standard concentration (1 ng g^{-1}). The signals at 1 ng g^{-1} were all significantly above baseline counts of 0, with PFTeDA having the lowest measured signal count (1.5×10^4) and all other analytes were greater (3.7×10^5 on average).

Uncertainties for the maternal transfer ratio (MTR) were calculated by propagating the relative standard deviations (see **Equation 4.5**). In instances where the contaminant concentration in either the mother or offspring was not detected, the limit of the MTR was estimated using the LOD. In these cases, the uncertainty in the MTR limits were determined by using the relative standard deviation (RSD) in the measured concentrations.

$$MTR\ Uncertainties = MTR \times \sqrt{\left(\frac{Standard\ Deviation_{Mother}}{Mean_{Mother}}\right)^2 + \left(\frac{Standard\ Deviation_{Offspring}}{Mean_{Offspring}}\right)^2} \quad \textbf{(Equation 4.5)}$$

Percent bias was calculated using **Equation 4.6.** For elemental analysis, samples were spiked with known concentrations of the multi-component standard and the resulting signal was background-subtracted with the same sample which had not been spiked. For PFAS analysis, the samples were spiked with known concentrations of isotopically-labelled standards.

$$Percent\ Bias = \frac{Experimental\ Concentration - Theoretical\ Concentration}{Theoretical\ Concentration} \times 100\% \quad \textbf{(Equation 4.6)}$$

Table 4.5.1: Information on the baseline-corrected linear regression curve of 18 metals. Footnotes include associated stock solution concentrations. [a]

Elements	Wavelength (nm)	R^2	Slope (mg kg^{-1})	Intercept	LOD [b] (mg kg^{-1})	Method Recovery (%)
Ag	328.0	0.997	1.34	8.61	0.53	64
Ba	233.5	0.995	5.83	34.5	0.096	99
Be	234.8	0.997	11.8	25.9	0.030	100
Bi	223.0	0.996	1.06	−11.9	1.3	100
Ca	184.0	0.995	12.5	−60.3	0.056	98
Cd	214.4	0.997	31.5	9.80	0.014	95
Co	228.6	0.997	11.4	32.1	0.19	97
Cr	205.5	0.997	6.57	20.7	0.16	105
Cu	204.3	0.997	0.954	3.54	0.55	91
Fe	274.9	0.997	1.99	−2.29	0.33	95
Mg	279.5	0.997	44.8	−2.32	0.059	90
Mn	260.5	0.998	4.5	1.40	0.34	93
Mo	204.5	0.998	1.61	−0.768	0.34	92
Ni	231.6	0.998	8.80	8.07	0.17	93
Pb	220.3	0.998	1.72	2.65	0.67	83
Sr	216.5	0.997	3.35	−0.0475	0.46	96
V	309.3	0.997	3.20	11	0.56	96
Zn	206.2	0.997	17.0	21	0.11	93

[a] This solution contains 27 metals at either 10 mg L^{-1} [Silver (Ag), Aluminum (Al), Barium (Ba), Beryllium (Be), Bismuth (Bi), Cadmium (Cd), Cesium (Cs), Cobalt (Co), Chromium (Cr), Copper (Cu), Gallium (Ga), Indium (In), Lead (Pb), Lithium (Li), Magnesium (Mg), Manganese (Mn), Molybdenum (Mo), Nickel (Ni), Rubidium (Rb), Strontium (Sr), Thallium (Tl), Vanadium (V), and Zinc (Zn)] or 100 mg L^{-1} [Calcium (Ca), Iron (Fe), Potassium (K), and Sodium (Na)] concentration in 10% (w/w) HNO_3.

[b] LOD calculated by 3 × standard deviation of sample blanks / slope of an 8-point calibration curve.

Table 4.5.2: Accuracy of the method using the DOLT-5 Certified Reference Material (CRM) dogfish liver tissue. [a]

Elements	Concentration of DOLT-5 CRM (mg kg^{-1})			Percent Bias (n = 4)
Arsenic	34.6	±	2.4	
Cadmium (Cd)	14.5	±	0.6	23
Calcium (Ca)	550	±	80	26
Cobalt (Co)	0.267	±	0.026	<LOD
Copper (Cu)	35	±	2.4	−14
Chromium (Cr)	2.35	±	0.58	<LOD
Iron (Fe)	1070	±	80	13
Lead (Pb)	0.162	±	0.032	<LOD
Magnesium (Mg)	940	±	100	23
Manganese (Mn)	8.91	±	0.70	28
Mercury	0.44	±	0.18	
Molybdenum (Mo)	1.41	±	0.22	<LOD
Nickel (Ni)	1.71	±	0.56	<LOD
Potassium (K)	14400	±	3000	<LOD
Selenium	8.3	±	1.8	
Silver (Ag)	2.05	±	0.08	<LOD
Sodium	9900	±	1600	
Strontium (Sr)	3.73	±	0.26	−8
Tin	0.069	±	0.036	
Vanadium (V)	0.51	±	0.06	22
Zinc (Zn)	105.3	±	5.4	19
Arsenobetaine	24.2	±	0.8	
Aluminum	31.7	±	4.2	
Methylmercury (as Hg)	0.119	±	0.058	
Antimony	0.013			
Phosphorous	11500			
Thallium	0.013			
Uranium	0.082			

[a] Percent bias calculation based on 0.5 g digest of Dogfish liver Certified Reference Material DOLT-5 (National Research Council Canada, Ottawa, ON, CAN)

Table 4.5.3: Information on the baseline-corrected and internal-standard normalized linear regression curve for native PFSAs and PFCAs and their retention times.

Compound [a]	Formula (Exact Mass (u))	RT (min)	Internal Standard	Slope (ng g^{-1})	Intercept	R^2
Perfluorobutanoic acid (PFBA)	$C_4HF_7O_2$ (213.9865)	3.13	$^{13}C_4$-PFBA	0.096	0.061	0.997
Perfluoropentanoate (PFPeA)	$C_5HF_9O_2$ (263.9833)	6.25	$^{13}C_2$-PFHxA	0.095	0.10	0.996
Perfluorohexanoate (PFHxA)	$C_6HF_{11}O_2$ (313.9801)	6.88	$^{13}C_2$-PFHxA	0.090	0.10	0.995
Perfluoroheptanoate (PFHpA)	$C_7HF_{13}O_2$ (363.9769)	7.25	$^{13}C_4$-PFOA	0.10	0.11	0.995
Perfluorooctanoate (PFOA)	$C_8HF_{15}O_2$ (413.9737)	7.51	$^{13}C_4$-PFOA	0.091	0.092	0.997
Perfluorononanoate (PFNA)	$C_9HF_{17}O_2$ (463.9705)	7.76	$^{13}C_5$-PFNA	0.086	0.082	0.996
Perfluorodecanoate (PFDA)	$C_{10}HF_{19}O_2$ (513.9673)	7.98	$^{13}C_2$-PFDA	0.092	0.053	0.999
Perfluoroundecanoate (PFUnDA)	$C_{11}HF_{21}O_2$ (563.9641)	8.22	$^{13}C_2$-PFUnDA	0.083	0.11	0.995
Perfluorododecanoate (PFDoDA)	$C_{12}HF_{23}O_2$ (613.9609)	8.41	$^{13}C_2$-PFDoDA	0.085	0.14	0.988
Perfluorotridecanoate (PFTrDA)	$C_{13}HF_{25}O2$ (663.9577)	8.58	$^{13}C_2$-PFDoDA	0.060	0.11	0.984
Perfluorotetradecanoate (PFTeDA)	$C_{14}HF_{27}O_2$ (713.9545)	8.75	$^{13}C_2$-PFDoDA	0.050	0.022	0.999
Perfluorohexadecanoate (PFHxDA)	$C_{16}HF_{31}O_2$ (813.9481)	9.04	$^{13}C_2$-PFDoDA	0.042	0.060	0.988
Perfluorooctadecanoate (PFOcDA)	$C_{18}HF_{35}O_2$ (913.9418)	9.32	$^{18}O_2$-PFHxS	0.18	0.29	0.986
Perfluorobutane sulfonate (PFBS)	$C_4HF_9O_3S$ (299.9503)	6.42	$^{18}O_2$-PFHxS	0.18	0.37	0.984
Perfluoropentane sulfonate (PFPeS)	$C_5HF_{11}O_3S$ (349.9471)	6.93	$^{18}O_2$-PFHxS	0.13	0.094	0.998
Perfluorohexane sulfonate (PFHxS)	$C_6HF_{13}O_3S$ (399.9439)	7.25	$^{18}O_2$-PFHxS	0.11	0.078	0.999
Perfluoroheptane sulfonate (PFHpS)	$C_7HF_{15}O_3S$ (449.9407)	7.51	$^{13}C_4$-PFOS	0.13	0.12	0.998
Perfluorooctane sulfonate (PFOS)	$C_8HF_{17}O_3S$ (499.9375)	7.72	$^{13}C_4$-PFOS	0.091	-0.065	0.996
Perfluorononane sulfonate (PFNS)	$C_9HF_{19}O_3S$ (549.9343)	7.98	$^{13}C_4$-PFOS	0.072	0.064	0.997
Perfluorodecane sulfonate (PFDS)	$C_{10}HF_{21}O_3S$ (599.9311)	8.19	$^{13}C_4$-PFOS	0.58	0.044	0.998
Perfluorododecane sulfonate (PFDoS)	$C_{12}HF_{25}O_3S$ (699.9247)	8.56	$^{13}C_4$-PFOS	0.033	0.025	0.999

[a] The native PFAS stock solution consisted of (PFAC-MXC) PFBA, PFPeA, PFHxA, PFHpA, PFOA, PFNA, PFDA, PFUnDA, PFDoDA, PFTrDA, PFTeDA, PFHxDA, PFOcDA, L-PFBS, L-PFPeS, L-PFHxS, L-PFHpS, L-PFOS, L-PFNS, L-PFDS, and L-PFDoS.

Table 4.5.4: Retention time and the mean ± standard deviation of the percent recovery of isotopically-labelled standards. [a]

Compound	Exact Mass (u)	RT (min)	Percent Recovery (%) Blanks (n = 3)	Mother (n = 9)	Offspring (n = 15)
$^{13}C_4$-PFBA	216.9923	3.08	89 ± 4	104 ± 21	100 ± 15
$^{13}C_2$-PFHxA	314.9791	6.87	96 ± 2	126 ± 69	152 ± 15
$^{13}C_4$-PFOA	416.9795	7.51	96 ± 1	157 ± 25	127 ± 17
$^{13}C_5$-PFNA	467.9797	7.74	88 ± 3	155 ± 31	132 ± 16
$^{13}C_2$-PFDA	514.9663	7.96	89 ± 4	160 ± 31	156 ± 23
$^{13}C_2$-PFUnDA	564.9631	8.17	90 ± 2	140 ± 25	142 ± 21
$^{13}C_2$-PFDoDA	614.9599	8.36	89 ± 3	153 ± 21	142 ± 23
$^{18}O_2$-PFHxS	402.9445	7.23	95 ± 3	104 ± 11	120 ± 11
$^{13}C_4$-PFOS	502.9433	7.72	75 ± 5	113 ± 21	106 ± 15

[a] The isotopically-labelled PFAS stock solution (MPFAC-MXA) $^{13}C_4$-PFBA, $^{13}C_5$-PFPeA, $^{13}C_5$-PFHxA, $^{13}C_4$-PFHpA, $^{13}C_8$-PFOA, $^{13}C_9$-PFNA, $^{13}C_6$-PFDA, $^{13}C_7$-PFUnDA, $^{13}C_2$-PFDoDA, $^{13}C_2$-PFTeDA, $^{13}C_3$-PFBS, $^{13}C_3$-PFHxS, and $^{13}C_8$-PFOS.

Table 4.5.5: Intra-sample and inter-sample variation in inorganic element digestions.

Elements	Concentration (mg kg^{-1}) Sample Replicates of Same Pup (n = 3) Mean	±	SD	RSD (%)	Individual Pup Samples (n = 8) Mean	±	SD	RSD (%)
Silver (Ag)	<LOD				<LOD			
Barium (Ba)	<LOD				0.252	±	0.468	186
Beryllium (Be)	<LOD				0.0470	±	0.0903	192
Bismuth (Bi)	4.93	±	2.23	45	5.48	±	4.74	86
Calcium (Ca)	28.5	±	5.6	20	34.2	±	12.1	35
Cadmium (Cd)	0.0933	±	0.0638	68	0.156	±	0.234	150
Cobalt (Co)	0.625	±	0.259	41	0.696	±	0.626	90
Copper (Cu)	7.71	±	1.98	26	9.24	±	8.10	88
Chromium (Cr)	0.629	±	0.165	26	1.19	±	1.51	127
Iron (Fe)	5.48	±	0.43	8	5.46	±	3.52	64
Magnesium (Mg)	37.6	±	1.6	4	34.4	±	5.7	17
Manganese (Mn)	<LOD				<LOD			
Molybdenum (Mo)	1.42	±	0.39	28	1.61	±	1.56	97
Nickel (Ni)	0.695	±	0.363	52	0.68	±	0.89	130
Lead (Pb)	2.95	±	1.17	40	3.46	±	3.01	87
Strontium (Sr)	0.901	±	0.271	30	1.03	±	0.96	94
Vanadium (V)	<LOD				<LOD			
Zinc (Zn)	3.28	±	0.32	10	3.10	±	0.59	19

Table 4.5.6: Summary of metal concentrations in the sixgill specimen and in the Strait of Georgia and example resulting bioconcentration factors (BCFs)

Location	Strait of Georgia		
Substrate	Adult Sixgill Liver (mg kg^{-1})	Average Concentration in Water (ng L^{-1})	BCF (SoG Sixgill / SoG Water)
Year	2019 Present Study	1983 [133]	2019/1983
Mn	0.9 ± 1.9	550 ± 280	2×10^{3}
Fe	395 ± 72	350 ± 71	1×10^{6}
Zn	13.1 ± 2.1	4550 ± 5590	3×10^{3}
Co	2.2 ± 1.7	26	8×10^{3}
Ni	2.7 ± 1.9	325 ± 35	8×10^{2}
Cu	16.2 ± 3.7	1750 ± 1770	9×10^{3}
Cd	6.3 ± 2.0	75 ± 7	8×10^{4}
Pb	7.3 ± 2.8	173 ± 136	4×10^{4}

Table 4.5.7: Concentrations (mg kg^{-1} dry weight) of 18 metals in bluntnose sixgill shark liver tissue samples as found by the method of standard additions.

	Mother (n = 4 samples) (mg kg^{-1} dw)			Offspring (n = 8 samples) (mg kg^{-1} dw)		
Elements	Mean ± SD	Median	Min–Max	Mean ± SD	Median	Min–Max
Ag	<0.53			<0.53		
Ba	<0.096			<0.096		
Be	<0.030			<0.030		
Bi	<1.2			<1.28		
Ca	25.1 ± 17.2	18.6	12.9–50.3	34.2 ± 12.1	29.7	24.9–61.8
Cd	6.25 ± 1.96	5.77	4.60–8.86	0.16 ± 0.23	0.05	<0.014–0.55
Co	2.17 ± 1.66	1.89	0.49–4.43	0.70 ± 0.63	0.51	<0.19–1.76
Cr	1.84 ± 1.75	1.16	0.64–4.41	1.19 ± 1.51	0.45	<0.16–4.07
Cu	16.2 ± 3.70	17.1	11.2–19.3	9.24 ± 8.10	7.21	0.050–21.6
Fe	395 ± 72	412	63.9–294	5.46 ± 3.52	4.64	<0.33–10.19
Mg	24.6 ± 5.1	24.6	18.8–30.2	34.4 ± 5.74	33.4	26.1–45.4
Mn	0.94 ± 1.88	<0.34	<0.34–3.76	<0.34		
Mo	4.27 ± 1.86	3.97	2.34–6.82	1.61 ± 1.56	1.23	<0.34–4.02
Ni	2.66 ± 1.85	2.17	0.98–5.30	0.68 ± 0.89	0.32	<0.17–2.24
Pb	7.32 ± 2.75	7.86	3.53–10.0	3.46 ± 3.01	2.59	<0.67–8.48
Sr	2.36 ± 1.74	1.82	0.90–4.89	1.03 ± 0.96	0.81	<0.46–2.67
V	<0.56			<0.56		
Zn	13.1 ± 2.1	13.1	11.1–15.1	3.10 ± 0.59	3.10	2.29–4.20
Dry Weight (%)	90.0 ± 0.2			76 ± 2		

Table 4.5.8: Concentrations (ng g^{-1} wet weight) of PFAS in bluntnose sixgill shark (*Hexanchus griseus*) liver tissue samples.

		Mother Liver (n = 3 subsections) (ng g^{-1} ww)			Pup Liver (n = 5 samples) (ng g^{-1} ww)		
Compound	LOD (ng g^{-1} liver)	Min–Max	Median	Mean ± SD	Min–Max	Median	Mean ± SD
PFBA [a]	1	<LOD			<LOD		
PFPeA [a]	1	<LOD			<LOD		
PFHxA [a]	1	<LOD			<LOD		
PFHpA [a]	1	<LOD			<LOD		
PFOA	0.42	<LOD			<LOD		
PFNA [a]	1	<LOD			1–1.9	1.2	1.3 ± 0.4
PFDA	0.14	<LOD			2.3–3.2	2.6	2.7 ± 0.4
PFUnDA	0.22	<LOD			16–25	19	20 ± 3
PFDoDA [a]	1	<LOD			1.9–3.8	2.9	2.8 ± 0.7
PFTrDA [a]	1	<LOD			21–30	25	26 ± 4
PFTeDA [a]	1	<LOD			2.3–4.6	3.2	3.2 ± 0.9
PFHxDA [a]	1	<LOD			<LOD		
PFOcDA	0.14	<LOD			<LOD		
PFBS	0.11	<LOD			<LOD		
PFPeS	0.12	0	0	0	<LOD		
PFHxS	0.020	0–0.35	0	0.12 ± 0.20	<LOD		
PFHpS [a]	1	0	0	0	<LOD		
PFOS	0.88	6–24	7	13 ± 9	13–18	16	16 ± 2
PFNS [a]	1	<LOD			<LOD		
PFDS [a]	1	<LOD			<LOD		
PFDoS [a]	1	<LOD			<LOD		
Lipid (% Weight)		45–66	60	57 ± 8	51–60	54	55 ± 3

[a] LOD based on lowest measured concentration (1 ng g^{-1}), and these were the values used for these analytes in the MTR calculations. The measured signal was 1.5×10^{4} (PFTeDA) or greater (the average of all of the other analytes was 3.7×10^{5}), well above a baseline count of zero at the same retention time.

Table 4.5.9: Comparing the Maternal Transfer Ratio (MTR) for PFAS in the Chynel *et al*. paper to the sixgill analyzed here.[131]

Species	Concentration in Mother (pg g^{-1} ww)		Concentration in Offspring (pg g^{-1} ww)		MTR	
	∑PFCAs [a]	PFOS	∑PFCAs [a]	PFOS	∑PFCAs	PFOS
Bull Shark Muscle Offspring n = 4 pools of 2 individuals	269	27	177	77	0.66	2.9
Tiger Shark Muscle Offspring n = 4 pools of 2 individuals and 2 individuals	61	19–29	1,382	below LOD (19 pg g^{-1})	23	1.3 [b]
Sixgill Liver Offspring n = 5	below LOD (∑LOD 4,363 pg g^{-1})	12,508	55,643	15,736	13 [c]	1.3

[a] ∑PFCAs were PFOS, PFNA PFDA, PFUnDA, PFDoDA, PFTrDA, PFTeDA
[b] Using PFOS maternal concentration to be LOD = 19 pg g^{-1}. Note that PFOS concentration was near detection limit for both mother and offspring.
[c] This value is a lower limit estimation for the MTR as $\sum LOD_{PFCAs}$ is used as the maternal concentration.

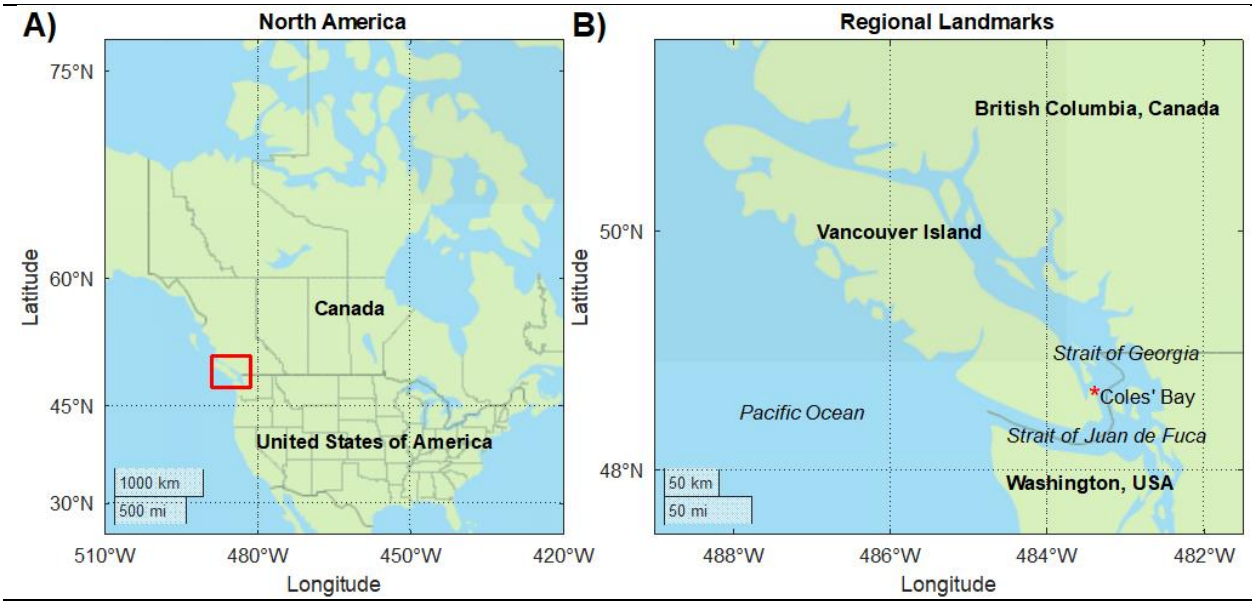

Figure 4.5.1. Simplified map of the region from where the deceased shark was collected.

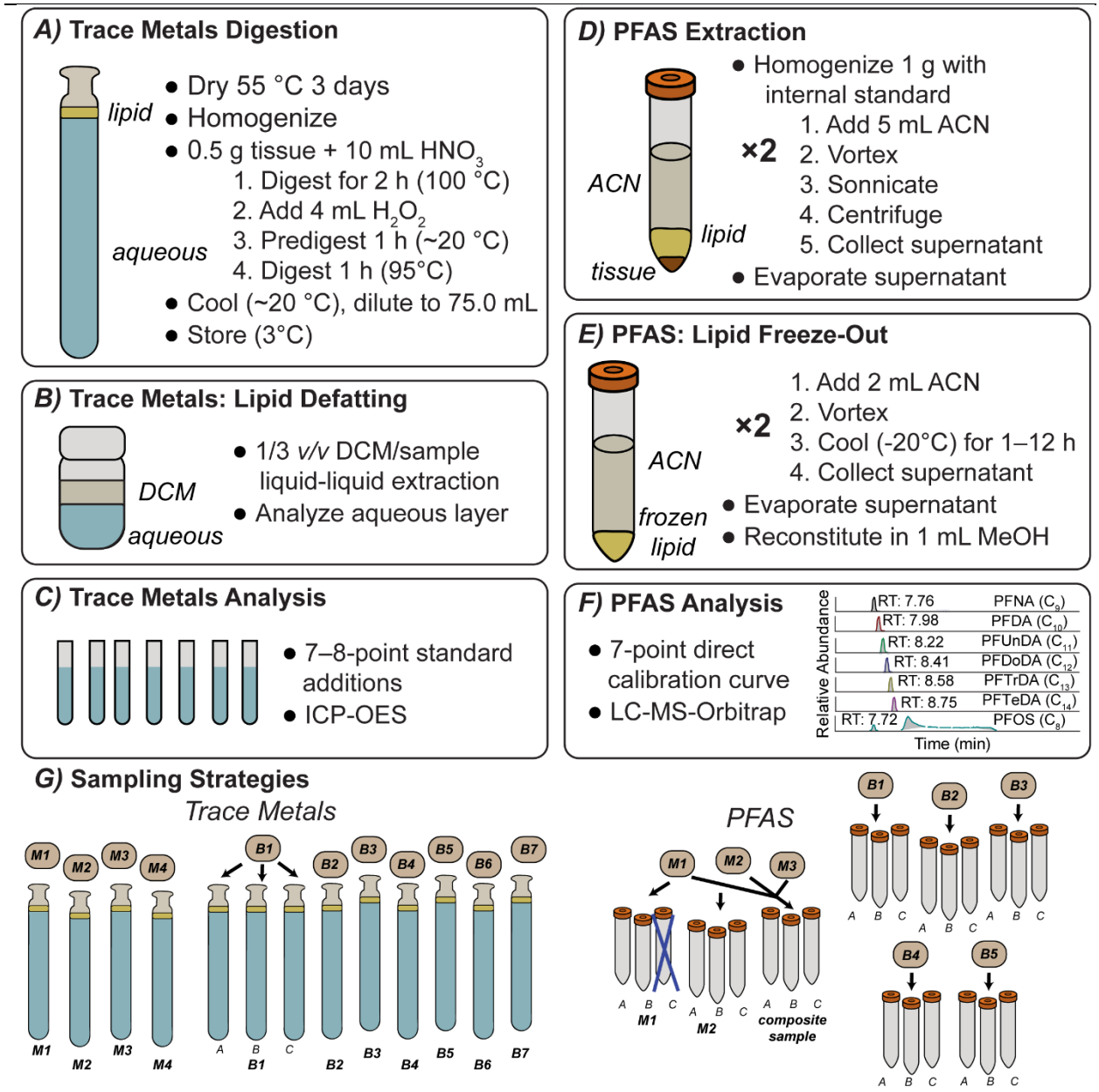

Figure 4.5.2. Sample preparation workflow for trace metals (left: A, B, C) and PFAS (right: D, E, F) and the corresponding sampling strategies (G).

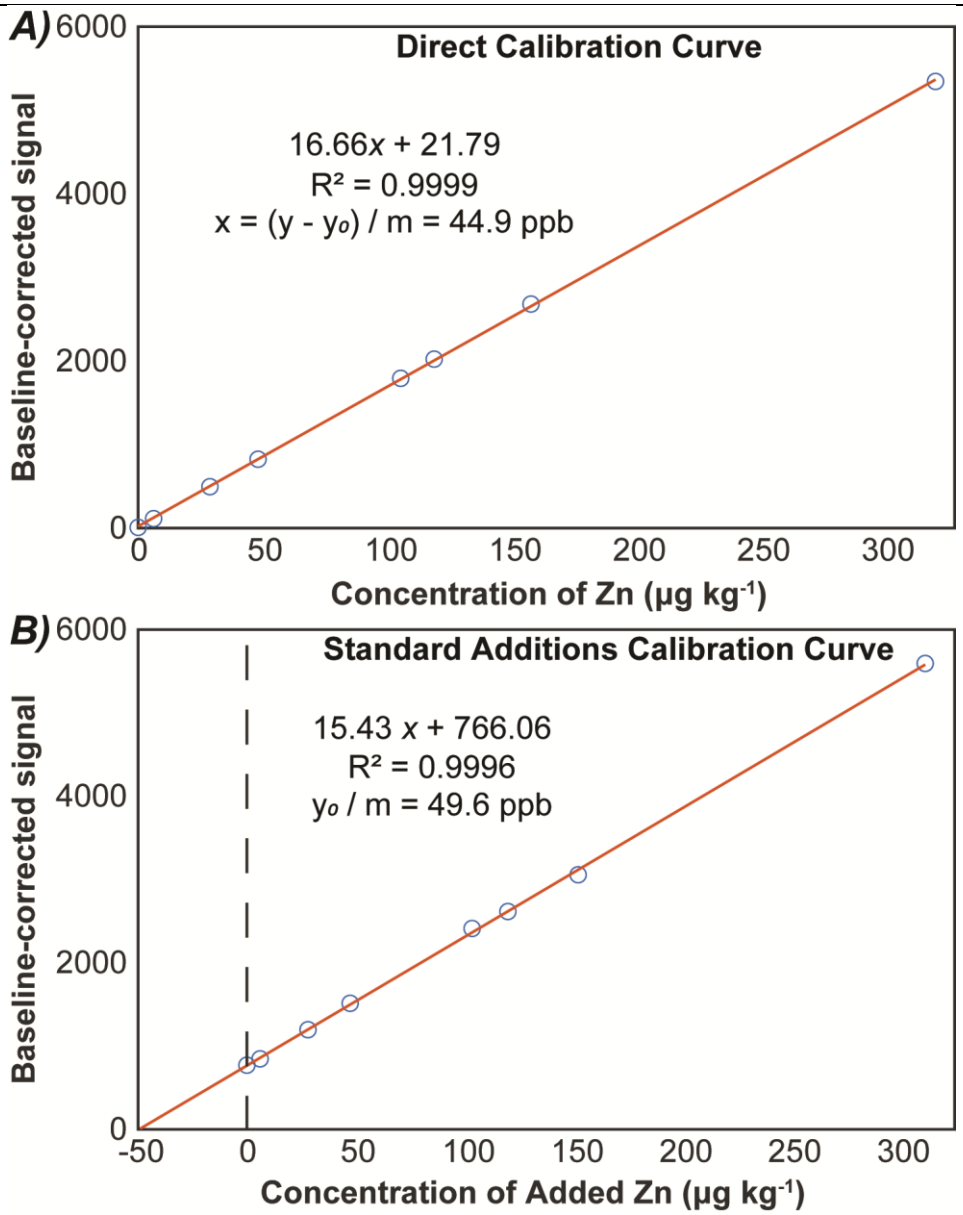

Figure 4.5.3. Representative calibration curves for quantifying inorganic elements in the aqueous sample (prior to correcting for dilution and the mass of shark sample digested) by A) a direct calibration curve and B) the method of standard additions.

Chapter 5: Conclusion

5.1 Summary of work

Condensed phase membrane introduction mass spectrometry (CP-MIMS) was applied in **Chapter 2** and **Chapter 3** to determine behaviour and physicochemical properties of a diverse suite of chemical contaminants. This included legacy pollutants such as polycyclic aromatic hydrocarbons (PAHs) and emerging pollutants including microplastics and chemicals known to leach from commercial plastics and rubbers: nonylphenol and *para*-phenylenediamine quinones (PPDQs). The work undertaken in **Chapter 2** monitored sorption processes in real-time for an hour, and intermittently up to three weeks later. In **Chapter 3**, the list of physicochemical properties, chemical sorbates, and sorbents investigated were expanded. The chemical partitioning of PPDQs to microplastics and sediments, PPDQs solubilities at 25 °C, and the enthalpy of 6PPD-quinone dissolution were reported. CP-MIMS proved a powerful experimental platform to achieve results with reasonable accuracy at environmentally relevant concentrations in complex heterogeneous samples.

The fate and distribution of environmental contaminants includes bioaccumulation within marine organisms and potentially the transmission from mother to offspring through the process of maternal transfer. In **Chapter 4**, conventional techniques were applied such as inductively coupled plasma optical emission spectroscopy (ICP-OES) for metals analysis, and liquid chromatography-electrospray ionization-high resolution mass spectrometry (LC-ESI-Orbitrap MS) for analysis of perfluoroalkyl substances (PFAS) in sixgill shark liver tissue. There is limited [106] to no permeability of the PDMS membrane for these analyte classes, making conventional analysis a requirement for these analytes. The maternal transfer between the adult and unborn offspring was analyzed for both contaminant classes, and bioconcentration was examined for select elements. The maternal transfer of PFAS was highly efficient, with almost all detectable PFAS going to the offspring, while metals were present at higher concentrations in the mother relative to the offspring and the water column. These findings highlight this species' unique, chemical-dependent maternal transfer mechanisms.

Elucidating physicochemical behaviour of pollutants, especially emerging contaminants, is key to understand their partitioning, fate, biological mechanisms of toxicity and accumulation, and how to treat environmental samples. Here, legacy pollutants such as PAHs and metals were studied. This provided additional confidence in applications of CP-MIMS to obtain physicochemical properties and context with which to compare the behaviour of emerging organic pollutants. There is great demand to resolve currently unanswered questions for emerging pollutants such as microplastics, PPDQs, and PFAS. For example, it is known that microplastics and nanoplastics have negative physical impacts on organisms,[25,28] but there is the potential that subtle toxicity effects are occurring due to the chemical load microplastics can carry.[28] 6PPD-quinone was discovered in 2020 to be the cause of mass die-offs of coho salmon,[31] affecting the fishing industry in the Pacific Northwest. Some contaminants cause subtle, sublethal toxicity effects, while others impact

ecosystems, and subsequently the human economics and politics based within and upon them, in ignorable ways.

Scientists are concerned with the fate and distribution of contaminants because, regardless of technological advances, humans as a species live in direct relation to the world. Due to improper disposal of materials and chemicals, a lack of a deliberate circular economy,[155] and ignorance of the potential harms of transformation products, we introduce harmful contaminants to ecosystems.[31] Many of these contaminants bioaccumulate through food webs and enter our lives again in the organisms we consume, the water we drink, the air we breathe. The negative impacts of pollution are felt most harshly upon those in the third world due to the developing world often shouldering the burden of both the manufacture [156] and disposal of chemicals and materials.[157] To minimize future pollution while remediating past inputs, chemical analysis must be applied to elucidate the behaviour of pollutants. In this thesis, different instrumental techniques were applied to this end.

5.2 Future Directions

Going forward, it is worth taking advantage of the unique insights that are possible with direct analysis with mass spectrometry (DMS). Measuring kinetics of sorption for multiple contaminants simultaneously at trace concentrations is made feasible with CP-MIMS. Additionally, the labour of conventional techniques used to quantify samples can be avoided with CP-MIMS and answers can be reached more efficiently. The CP-MIMS approach is particularly appropriate for analyzing complex environmental samples and for elucidating certain physicochemical properties.

There is much more about the behaviour of microplastics and their interaction with chemical contaminants that can and should be studied with CP-MIMS. Predominantly plastic pellets were studied in this thesis. Future work should be applied to currently understudied sorbent plastics including nanoplastics, clothing fibers, recycled plastics, 'green' plastics (such as polylactic acid),[155] and rubbers such as tire wear particles (TWPs). Notably, when examining plastic powders with CP-MIMS, the plastic flakes were observed to adhere to the membrane. Thus, to study powdered and nanosized plastics it may be necessary to construct a barrier around the membrane to prevent the signal from becoming smothered. Additionally, CP-MIMS would be well-suited to analyze the kinetics (speed) and thermodynamics (completion) of remediation and filtration for inexpensive sorbents such as sawdust, plants, charcoal, and even recycled plastics.

DMS approaches can be applied to characterize the surface and bulk properties of plastics, as sorption encompasses both adsorption and absorption processes. Early work began characterizing how surface changes impact adsorption processes by studying sorption to weathered plastics in **Chapter 2**. Natural weathering processes take much longer than artificial, accelerated photooxidative weathering [29] but it is important to study sorption on plastics which were weathered with different light sources as there are appears to be distinctions in sorption behaviour (see **Figure 2.3.3**).[107] Future work should also examine whether biofilm formation impedes or increases the kinetics or

thermodynamics of sorption for a diverse suite of contaminants (polar, nonpolar, neutral, charged) under different conditions. Finally, absorption processes into the bulk plastic should be characterized. The extent to which absorption occurs is dependent on the permeability and crystallinity of the plastic.[107] DMS imaging techniques such as nanospray desorption electrospray MS (nano-DESI-MS) [158] or matrix assisted laser desorption ionization MS (MALDI-MS) [43] would be uniquely suited to answer to what extent and over what time periods contaminant absorption occurs for different plastics, both pristine and weathered.

In this thesis, all aqueous samples were constructed using deionized water, but as the PDMS membrane serves as an on-line filter CP-MIMS can be applied to complex, real-world aqueous samples. Future work can and should study if the conditions of the system (pH, salinity, and the presence of dissolved organic material in constructed and natural water systems) influence sorption in a negative or positive way. Relatedly, measuring the kinetics of desorption for co-occurring sorbed contaminants or the leaching of additives and plasticizers, in different systems can be especially useful. Namely, does altering the pH, salinity, dissolved organic material content in a sample solution encourage leaching? Does mimicking conditions of the digestive system with low pH, salt, bile, and digestive enzymes encourage desorption of contaminants? This would help clarify whether chemical desorption is increased under certain environmental or biological conditions.

As seen in **Chapter 1** and **Chapter 2**, CP-MIMS is very well-suited to study many physicochemical properties as it is a direct approach. Real-time processes and complicated samples can be measured *in situ* and at higher throughput because of the circumvention of chromatography and sample cleanup. There are other physicochemical properties that would be well-suited to this technique, other than finding the organic carbon-water partition coefficients (K_{OC}) and aqueous solubility limits of contaminants. Because the PDMS membrane is impermeable to charged compounds, CP-MIMS can be applied to find the pK_a of different analytes.[106] Additionally, because CP-MIMS is a real time technique it can be used to characterize air-water partitioning (K_{AW}). Future work should focus on quantifying these physicochemical properties for emerging contaminants including the PPDQs. Additionally, desorption isotherms should be built for sediments, plastics, and tire wear particles (TWPs) to quantify the leaching of PPDQs from these sorbents.

Lastly, there are cases where an application of both conventional and direct mass spectrometry approaches provides the best of both worlds. For example, CP-MIMS is highly suited for instances where many samples need to be screened, particularly when the samples contain complex matrices. CP-MIMS can be applied to provide rapid evidence of contaminants in a sample, albeit without chromatographic resolution. Conventional techniques can then be applied with confidence that the investment in time and cost for sample preparation, chromatographic separation, and potentially the use of HRMS will be rewarded. **Chapter 4** is an example of one such use case, wherein preliminary CP-MIMS results indicated that the liver tissue of the adult sixgill shark contained persistent organic pollutants which informed future action with conventional analysis. The sampling simplicity of CP-MIMS can and should be coupled to more complex analysis approaches to understand real-world samples. The sample clean-up provided by CP-MIM is often faster

and less expensive than typical approaches. In such a way, CP-MIMS can be coupled to high resolution mass spectrometry, and extracts can ultimately be applied to a liquid chromatography column. Multivariate analysis can be applied to mass spectral data acquired with CP-MIMS to perform source apportionment or environmental forensics.[159,160] All research in this thesis has been applied using targeted analysis, but non-targeted analysis and such as Data Independent Acquisition (DIA) approaches [161] can be applied to HRMS mass spectral data to identify new and emerging contaminants.

References

(1) Yuan, T.; Vadde, K. K.; Tonkin, J. D.; Wang, J.; Lu, J.; Zhang, Z.; Zhang, Y.; McCarthy, A. J.; Sekar, R. Urbanization Impacts the Physicochemical Characteristics and Abundance of Fecal Markers and Bacterial Pathogens in Surface Water. *Int. J. Environ. Res. Public. Health* **2019**, *16* (10), 1739. https://doi.org/10.3390/ijerph16101739.

(2) Strokal, M.; Bai, Z.; Franssen, W.; Hofstra, N.; Koelmans, A. A.; Ludwig, F.; Ma, L.; Van Puijenbroek, P.; Spanier, J. E.; Vermeulen, L. C.; Van Vliet, M. T. H.; Van Wijnen, J.; Kroeze, C. Urbanization: An Increasing Source of Multiple Pollutants to Rivers in the 21st Century. *Npj Urban Sustain.* **2021**, *1* (1), 24. https://doi.org/10.1038/s42949-021-00026-w.

(3) Nipen, M.; Vogt, R. D.; Bohlin-Nizzetto, P.; Borgå, K.; Mwakalapa, E. B.; Borgen, A. R.; Schlabach, M.; Christensen, G.; Mmochi, A. J.; Breivik, K. Increasing Trends of Legacy and Emerging Organic Contaminants in a Dated Sediment Core From East-Africa. *Front. Environ. Sci.* **2022**, *9*, 805544. https://doi.org/10.3389/fenvs.2021.805544.

(4) Chapman, P. M. Determining When Contamination Is Pollution — Weight of Evidence Determinations for Sediments and Effluents. *Environ. Int.* **2007**, *33* (4), 492–501. https://doi.org/10.1016/j.envint.2006.09.001.

(5) Bayabil, H. K.; Teshome, F. T.; Li, Y. C. Emerging Contaminants in Soil and Water. *Front. Environ. Sci.* **2022**, *10*, 873499. https://doi.org/10.3389/fenvs.2022.873499.

(6) VanLoon, G. W.; Duffy, S. J. *Environmental Chemistry: A Global Perspective*, Fourth edition.; Oxford University Press: Oxford, United Kingdom, 2017.

(7) Bashir, I.; Lone, F. A.; Bhat, R. A.; Mir, S. A.; Dar, Z. A.; Dar, S. A. Concerns and Threats of Contamination on Aquatic Ecosystems. In *Bioremediation and Biotechnology*; Hakeem, K. R., Bhat, R. A., Qadri, H., Eds.; Springer International Publishing: Cham, 2020; pp 1–26. https://doi.org/10.1007/978-3-030-35691-0_1.

(8) Lewis, A. J.; Yun, X.; Spooner, D. E.; Kurz, M. J.; McKenzie, E. R.; Sales, C. M. Exposure Pathways and Bioaccumulation of Per- and Polyfluoroalkyl Substances in Freshwater Aquatic Ecosystems: Key Considerations. *Sci. Total Environ.* **2022**, *822*, 153561. https://doi.org/10.1016/j.scitotenv.2022.153561.

(9) Schwarzenbach, R. P.; Gschwend, P. M.; Imboden, D. M. *Environmental Organic Chemistry*, 1st ed.; Wiley, 2002. https://doi.org/10.1002/0471649643.

(10) Fries, E.; Grewal, T.; Sühring, R. Persistent, Mobile, and Toxic Plastic Additives in Canada: Properties and Prioritization. *Environ. Sci. Process. Impacts* **2022**, *24* (10), 1945–1956. https://doi.org/10.1039/D2EM00097K.

(11) Tian, Z.; Gonzalez, M.; Rideout, C. A.; Zhao, H. N.; Hu, X.; Wetzel, J.; Mudrock, E.; James, C. A.; McIntyre, J. K.; Kolodziej, E. P. 6PPD-Quinone: Revised Toxicity Assessment and

Quantification with a Commercial Standard. *Environ. Sci. Technol. Lett.* **2022**, *9* (2), 140–146. https://doi.org/10.1021/acs.estlett.1c00910.

(12) Desforges, J.-P.; Hall, A.; McConnell, B.; Rosing-Asvid, A.; Barber, J. L.; Brownlow, A.; De Guise, S.; Eulaers, I.; Jepson, P. D.; Letcher, R. J.; Levin, M.; Ross, P. S.; Samarra, F.; Víkingson, G.; Sonne, C.; Dietz, R. Predicting Global Killer Whale Population Collapse from PCB Pollution. *Science* **2018**, *361* (6409), 1373–1376. https://doi.org/10.1126/science.aat1953.

(13) Xie, J.; Bian, Z.; Lin, T.; Tao, L.; Wu, Q.; Chu, M. Global Occurrence, Bioaccumulation Factors and Toxic Effects of Polychlorinated Biphenyls in Tuna: A Review. *Emerg. Contam.* **2020**, *6*, 388–395. https://doi.org/10.1016/j.emcon.2020.11.003.

(14) Schanne, F. A.; Dowd, T. L.; Gupta, R. K.; Rosen, J. F. Lead Increases Free Ca2+ Concentration in Cultured Osteoblastic Bone Cells: Simultaneous Detection of Intracellular Free Pb2+ by 19F NMR. *Proc. Natl. Acad. Sci.* **1989**, *86* (13), 5133–5135. https://doi.org/10.1073/pnas.86.13.5133.

(15) National Research Council (U. S.). *A Framework to Guide Selection of Chemical Alternatives*; The National Academies Press: Washington, D.C, 2014.

(16) Vasseghian, Y.; Hosseinzadeh, S.; Khataee, A.; Dragoi, E.-N. The Concentration of Persistent Organic Pollutants in Water Resources: A Global Systematic Review, Meta-Analysis and Probabilistic Risk Assessment. *Sci. Total Environ.* **2021**, *796*, 149000. https://doi.org/10.1016/j.scitotenv.2021.149000.

(17) Sauvé, S.; Desrosiers, M. A Review of What Is an Emerging Contaminant. *Chem. Cent. J.* **2014**, *8* (1), 15. https://doi.org/10.1186/1752-153X-8-15.

(18) Farrington, J.; Takada, H. Persistent Organic Pollutants (POPs), Polycyclic Aromatic Hydrocarbons (PAHs), and Plastics: Examples of the Status, Trend, and Cycling of Organic Chemicals of Environmental Concern in the Ocean. *Oceanography* **2014**, *27* (1), 196–213. https://doi.org/10.5670/oceanog.2014.23.

(19) Tansel, B.; Fuentes, C.; Sanchez, M.; Predoi, K.; Acevedo, M. Persistence Profile of Polyaromatic Hydrocarbons in Shallow and Deep Gulf Waters and Sediments: Effect of Water Temperature and Sediment–Water Partitioning Characteristics. *Mar. Pollut. Bull.* **2011**, *62* (12), 2659–2665. https://doi.org/10.1016/j.marpolbul.2011.09.026.

(20) Fenton, S. E.; Ducatman, A.; Boobis, A.; DeWitt, J. C.; Lau, C.; Ng, C.; Smith, J. S.; Roberts, S. M. Per- and Polyfluoroalkyl Substance Toxicity and Human Health Review: Current State of Knowledge and Strategies for Informing Future Research. *Environ. Toxicol. Chem.* **2021**, *40* (3), 606–630. https://doi.org/10.1002/etc.4890.

(21) Lee, J. W.; Choi, K.; Park, K.; Seong, C.; Yu, S. D.; Kim, P. Adverse Effects of Perfluoroalkyl Acids on Fish and Other Aquatic Organisms: A Review. *Sci. Total Environ.* **2020**, *707*, 135334. https://doi.org/10.1016/j.scitotenv.2019.135334.

(22) Bhandari, G.; Bagheri, A. R.; Bhatt, P.; Bilal, M. Occurrence, Potential Ecological Risks, and Degradation of Endocrine Disrupter, Nonylphenol, from the Aqueous Environment. *Chemosphere* **2021**, *275*, 130013. https://doi.org/10.1016/j.chemosphere.2021.130013.

(23) De La Parra-Guerra, A. C.; Acevedo-Barrios, R. Studies of Endocrine Disruptors: Nonylphenol and Isomers in Biological Models. *Environ. Toxicol. Chem.* **2023**, *42* (7), 1439–1450. https://doi.org/10.1002/etc.5633.

(24) Mato, Y.; Isobe, T.; Takada, H.; Kanehiro, H.; Ohtake, C.; Kaminuma, T. Plastic Resin Pellets as a Transport Medium for Toxic Chemicals in the Marine Environment. *Environ. Sci. Technol.* **2001**, *35* (2), 318–324. https://doi.org/10.1021/es0010498.

(25) Wright, S. L.; Thompson, R. C.; Galloway, T. S. The Physical Impacts of Microplastics on Marine Organisms: A Review. *Environ. Pollut.* **2013**, *178*, 483–492. https://doi.org/10.1016/j.envpol.2013.02.031.

(26) Cole, M.; Lindeque, P.; Halsband, C.; Galloway, T. S. Microplastics as Contaminants in the Marine Environment: A Review. *Mar. Pollut. Bull.* **2011**, *62* (12), 2588–2597. https://doi.org/10.1016/j.marpolbul.2011.09.025.

(27) Thompson, R. C.; Olsen, Y.; Mitchell, R. P.; Davis, A.; Rowland, S. J.; John, A. W. G.; McGonigle, D.; Russell, A. E. Lost at Sea: Where Is All the Plastic? *Science* **2004**, *304* (5672), 838–838. https://doi.org/10.1126/science.1094559.

(28) Yu, Y.; Mo, W. Y.; Luukkonen, T. Adsorption Behaviour and Interaction of Organic Micropollutants with Nano and Microplastics – A Review. *Sci. Total Environ.* **2021**, *797*, 149140. https://doi.org/10.1016/j.scitotenv.2021.149140.

(29) Zvekic, M.; Richards, L. C.; Tong, C. C.; Krogh, E. T. Characterizing Photochemical Ageing Processes of Microplastic Materials Using Multivariate Analysis of Infrared Spectra. *Environ. Sci. Process. Impacts* **2022**, *24* (1), 52–61. https://doi.org/10.1039/D1EM00392E.

(30) Lambert, S.; Wagner, M. Microplastics Are Contaminants of Emerging Concern in Freshwater Environments: An Overview. In *Freshwater Microplastics*; Wagner, M., Lambert, S., Eds.; The Handbook of Environmental Chemistry; Springer International Publishing: Cham, 2018; Vol. 58, pp 1–23. https://doi.org/10.1007/978-3-319-61615-5_1.

(31) Tian, Z.; Zhao, H.; Peter, K. T.; Gonzalez, M.; Wetzel, J.; Wu, C.; Hu, X.; Prat, J.; Mudrock, E.; Hettinger, R.; Cortina, A. E.; Biswas, R. G.; Kock, F. V. C.; Soong, R.; Jenne, A.; Du, B.; Hou, F.; He, H.; Lundeen, R.; Gilbreath, A.; Sutton, R.; Scholz, N. L.; Davis, J. W.; Dodd, M. C.; Simpson, A.; McIntyre, J. K.; Kolodziej, E. P. A Ubiquitous Tire Rubber–Derived Chemical Induces Acute Mortality in Coho Salmon. *Science* **2021**, *371* (6525), 185–189. https://doi.org/10.1126/science.abd6951.

(32) Hiki, K.; Yamamoto, H. Concentration and Leachability of N-(1,3-Dimethylbutyl)-N′-Phenyl-p-Phenylenediamine (6PPD) and Its Quinone Transformation Product (6PPD-Q) in Road Dust Collected in Tokyo, Japan. *Environ. Pollut.* **2022**, *302*, 119082. https://doi.org/10.1016/j.envpol.2022.119082.

(33) Zhu, J.; Guo, R.; Ren, F.; Jiang, S.; Jin, H. Occurrence and Partitioning of P-Phenylenediamine Antioxidants and Their Quinone Derivatives in Water and Sediment. *Sci. Total Environ.* **2024**, *914*, 170046. https://doi.org/10.1016/j.scitotenv.2024.170046.

(34) Monaghan, J.; Jaeger, A.; Jai, J. K.; Tomlin, H.; Atkinson, J.; Brown, T. M.; Gill, C. G.; Krogh, E. T. Automated, High-Throughput Analysis of Tire-Derived *p* -Phenylenediamine Quinones (PPDQs) in Water by Online Membrane Sampling Coupled to MS/MS. *ACS EST Water* **2023**, *3* (10), 3293–3304. https://doi.org/10.1021/acsestwater.3c00275.

(35) Nair, P.; Sun, J.; Xie, L.; Kennedy, L.; Kozakiewicz, D.; Kleywegt, S.; Hao, C.; Byun, H.; Barrett, H.; Baker, J.; Monaghan, J.; Krogh, E.; Song, D.; Peng, H. *Synthesis and Toxicity Evaluation of Tire Rubber-Derived Quinones*; preprint; Chemistry, 2023. https://doi.org/10.26434/chemrxiv-2023-pmxvc.

(36) Zhao, H. N.; Hu, X.; Gonzalez, M.; Rideout, C. A.; Hobby, G. C.; Fisher, M. F.; McCormick, C. J.; Dodd, M. C.; Kim, K. E.; Tian, Z.; Kolodziej, E. P. Screening *p* -Phenylenediamine Antioxidants, Their Transformation Products, and Industrial Chemical Additives in Crumb Rubber and Elastomeric Consumer Products. *Environ. Sci. Technol.* **2023**, *57* (7), 2779–2791. https://doi.org/10.1021/acs.est.2c07014.

(37) Brinkmann, M.; Montgomery, D.; Selinger, S.; Miller, J. G. P.; Stock, E.; Alcaraz, A. J.; Challis, J. K.; Weber, L.; Janz, D.; Hecker, M.; Wiseman, S. Acute Toxicity of the Tire Rubber-Derived Chemical 6PPD-Quinone to Four Fishes of Commercial, Cultural, and Ecological Importance. *Environ. Sci. Technol. Lett.* **2022**, *9* (4), 333–338. https://doi.org/10.1021/acs.estlett.2c00050.

(38) Montgomery, D.; Ji, X.; Cantin, J.; Philibert, D.; Foster, G.; Selinger, S.; Jain, N.; Miller, J.; McIntyre, J.; De Jourdan, B.; Wiseman, S.; Hecker, M.; Brinkmann, M. Interspecies Differences in 6PPD-Quinone Toxicity Across Seven Fish Species: Metabolite Identification and Semiquantification. *Environ. Sci. Technol.* **2023**, *57* (50), 21071–21079. https://doi.org/10.1021/acs.est.3c06891.

(39) Di Guardo, A.; Gouin, T.; MacLeod, M.; Scheringer, M. Environmental Fate and Exposure Models: Advances and Challenges in 21 st Century Chemical Risk Assessment. *Environ. Sci. Process. Impacts* **2018**, *20* (1), 58–71. https://doi.org/10.1039/C7EM00568G.

(40) Engkvist, O.; Norrby, P.-O.; Selmi, N.; Lam, Y.; Peng, Z.; Sherer, E. C.; Amberg, W.; Erhard, T.; Smyth, L. A. Computational Prediction of Chemical Reactions: Current Status and Outlook. *Drug Discov. Today* **2018**, *23* (6), 1203–1218. https://doi.org/10.1016/j.drudis.2018.02.014.

(41) Borden, S. A.; Mercer, S. R.; Saatchi, A.; Wong, E.; Stefan, C. M.; Wiebe, H.; Hore, D. K.; Wallace, B.; Gill, C. G. Carfentanil Structural Analogs Found in Street Drugs by Paper Spray Mass Spectrometry and Their Characterization by High-resolution Mass Spectrometry. *Drug Test. Anal.* **2023**, *15* (5), 484–494. https://doi.org/10.1002/dta.3431.

(42) Skoog, D. A.; Holler, F. J.; Crouch, S. R. *Principles of Instrumental Analysis*, Seventh edition.; Cengage Learning: Australia, 2018.

(43) Gross, J. H. *Mass Spectrometry*; Springer International Publishing: Cham, 2017. https://doi.org/10.1007/978-3-319-54398-7.

(44) Wilschefski, S.; Baxter, M. Inductively Coupled Plasma Mass Spectrometry: Introduction to Analytical Aspects. *Clin. Biochem. Rev.* **2019**, *40* (3), 115–133. https://doi.org/10.33176/AACB-19-00024.

(45) Termopoli, V.; Famiglini, G.; Palma, P.; Piergiovanni, M.; Rocio-Bautista, P.; Ottaviani, M. F.; Cappiello, A.; Saeed, M.; Perry, S. Evaluation of a Liquid Electron Ionization Liquid Chromatography–Mass Spectrometry Interface. *J. Chromatogr. A* **2019**, *1591*, 120–130. https://doi.org/10.1016/j.chroma.2019.01.034.

(46) Vandergrift, G. W.; Monaghan, J.; Krogh, E. T.; Gill, C. G. Direct Analysis of Polyaromatic Hydrocarbons in Soil and Aqueous Samples Using Condensed Phase Membrane Introduction Tandem Mass Spectrometry with Low-Energy Liquid Electron Ionization. *Anal. Chem.* **2019**, *91* (2), 1587–1594. https://doi.org/10.1021/acs.analchem.8b04949.

(47) Vandergrift, G. W.; Krogh, E. T.; Gill, C. G. Direct, Isomer-Specific Quantitation of Polycyclic Aromatic Hydrocarbons in Soils Using Membrane Introduction Mass Spectrometry and Chemical Ionization. *Anal. Chem.* **2020**, *92* (23), 15480–15488. https://doi.org/10.1021/acs.analchem.0c03259.

(48) Vandergrift, G. W.; Lattanzio-Battle, W.; Krogh, E. T.; Gill, C. G. Condensed Phase Membrane Introduction Mass Spectrometry with *In Situ* Liquid Reagent Chemical Ionization in a Liquid Electron Ionization Source (CP-MIMS-LEI/CI). *J. Am. Soc. Mass Spectrom.* **2020**, *31* (4), 908–916. https://doi.org/10.1021/jasms.9b00143.

(49) Konermann, L.; Ahadi, E.; Rodriguez, A. D.; Vahidi, S. Unraveling the Mechanism of Electrospray Ionization. *Anal. Chem.* **2013**, *85* (1), 2–9. https://doi.org/10.1021/ac302789c.

(50) Termopoli, V.; Torrisi, E.; Famiglini, G.; Palma, P.; Zappia, G.; Cappiello, A.; Vandergrift, G. W.; Zvekic, M.; Krogh, E. T.; Gill, C. G. Mass Spectrometry Based Approach for Organic Synthesis Monitoring. *Anal. Chem.* **2019**, *91* (18), 11916–11922. https://doi.org/10.1021/acs.analchem.9b02681.

(51) Cao, Y.; Zhao, M.; Ma, X.; Song, Y.; Zuo, S.; Li, H.; Deng, W. A Critical Review on the Interactions of Microplastics with Heavy Metals: Mechanism and Their Combined Effect on Organisms and Humans. *Sci. Total Environ.* **2021**, *788*, 147620. https://doi.org/10.1016/j.scitotenv.2021.147620.

(52) Brahney, J.; Mahowald, N.; Prank, M.; Cornwell, G.; Klimont, Z.; Matsui, H.; Prather, K. A. Constraining the Atmospheric Limb of the Plastic Cycle. *Proc. Natl. Acad. Sci.* **2021**, *118* (16), e2020719118. https://doi.org/10.1073/pnas.2020719118.

(53) Kwon, J.; Chang, S.; Hong, S. H.; Shim, W. J. Microplastics as a Vector of Hydrophobic Contaminants: Importance of Hydrophobic Additives. *Integr. Environ. Assess. Manag.* **2017**, *13* (3), 494–499. https://doi.org/10.1002/ieam.1906.

(54) Koelmans, A. A.; Bakir, A.; Burton, G. A.; Janssen, C. R. Microplastic as a Vector for Chemicals in the Aquatic Environment: Critical Review and Model-Supported Reinterpretation of Empirical Studies. *Environ. Sci. Technol.* **2016**, *50* (7), 3315–3326. https://doi.org/10.1021/acs.est.5b06069.

(55) Song, Y. K.; Hong, S. H.; Jang, M.; Han, G. M.; Jung, S. W.; Shim, W. J. Combined Effects of UV Exposure Duration and Mechanical Abrasion on Microplastic Fragmentation by Polymer Type. *Environ. Sci. Technol.* **2017**, *51* (8), 4368–4376. https://doi.org/10.1021/acs.est.6b06155.

(56) Sørensen, L.; Rogers, E.; Altin, D.; Salaberria, I.; Booth, A. M. Sorption of PAHs to Microplastic and Their Bioavailability and Toxicity to Marine Copepods under Co-Exposure Conditions. *Environ. Pollut.* **2020**, *258*, 113844. https://doi.org/10.1016/j.envpol.2019.113844.

(57) Bucci, K.; Bikker, J.; Stevack, K.; Watson-Leung, T.; Rochman, C. Impacts to Larval Fathead Minnows Vary between Preconsumer and Environmental Microplastics. *Environ. Toxicol. Chem.* **2022**, *41* (4), 858–868. https://doi.org/10.1002/etc.5036.

(58) Li, J.; Zhang, K.; Zhang, H. Adsorption of Antibiotics on Microplastics. *Environ. Pollut.* **2018**, *237*, 460–467. https://doi.org/10.1016/j.envpol.2018.02.050.

(59) Razanajatovo, R. M.; Ding, J.; Zhang, S.; Jiang, H.; Zou, H. Sorption and Desorption of Selected Pharmaceuticals by Polyethylene Microplastics. *Mar. Pollut. Bull.* **2018**, *136*, 516–523. https://doi.org/10.1016/j.marpolbul.2018.09.048.

(60) Guo, X.; Wang, X.; Zhou, X.; Kong, X.; Tao, S.; Xing, B. Sorption of Four Hydrophobic Organic Compounds by Three Chemically Distinct Polymers: Role of Chemical and Physical Composition. *Environ. Sci. Technol.* **2012**, *46* (13), 7252–7259. https://doi.org/10.1021/es301386z.

(61) Joo, S. H.; Liang, Y.; Kim, M.; Byun, J.; Choi, H. Microplastics with Adsorbed Contaminants: Mechanisms and Treatment. *Environ. Chall.* **2021**, *3*, 100042. https://doi.org/10.1016/j.envc.2021.100042.

(62) Dissanayake, P. D.; Kim, S.; Sarkar, B.; Oleszczuk, P.; Sang, M. K.; Haque, M. N.; Ahn, J. H.; Bank, M. S.; Ok, Y. S. Effects of Microplastics on the Terrestrial Environment: A Critical Review. *Environ. Res.* **2022**, *209*, 112734. https://doi.org/10.1016/j.envres.2022.112734.

(63) Bakir, A.; Rowland, S. J.; Thompson, R. C. Competitive Sorption of Persistent Organic Pollutants onto Microplastics in the Marine Environment. *Mar. Pollut. Bull.* **2012**, *64* (12), 2782–2789. https://doi.org/10.1016/j.marpolbul.2012.09.010.

(64) Tamis, J. E.; Koelmans, A. A.; Dröge, R.; Kaag, N. H. B. M.; Keur, M. C.; Tromp, P. C.; Jongbloed, R. H. Environmental Risks of Car Tire Microplastic Particles and Other Road Runoff Pollutants. *Microplastics Nanoplastics* **2021**, *1* (1), 10. https://doi.org/10.1186/s43591-021-00008-w.

(65) Müller, A.; Becker, R.; Dorgerloh, U.; Simon, F.-G.; Braun, U. The Effect of Polymer Aging on the Uptake of Fuel Aromatics and Ethers by Microplastics. *Environ. Pollut.* **2018**, *240*, 639–646. https://doi.org/10.1016/j.envpol.2018.04.127.

(66) Fu, L.; Li, J.; Wang, G.; Luan, Y.; Dai, W. Adsorption Behavior of Organic Pollutants on Microplastics. *Ecotoxicol. Environ. Saf.* **2021**, *217*, 112207. https://doi.org/10.1016/j.ecoenv.2021.112207.

(67) Chen, Z.; Chen, B.; Chiou, C. T. Fast and Slow Rates of Naphthalene Sorption to Biochars Produced at Different Temperatures. *Environ. Sci. Technol.* **2012**, *46* (20), 11104–11111. https://doi.org/10.1021/es302345e.

(68) Ziccardi, L. M.; Edgington, A.; Hentz, K.; Kulacki, K. J.; Kane Driscoll, S. Microplastics as Vectors for Bioaccumulation of Hydrophobic Organic Chemicals in the Marine Environment: A State-of-the-science Review. *Environ. Toxicol. Chem.* **2016**, *35* (7), 1667–1676. https://doi.org/10.1002/etc.3461.

(69) O'Connor, I. A.; Golsteijn, L.; Hendriks, A. J. Review of the Partitioning of Chemicals into Different Plastics: Consequences for the Risk Assessment of Marine Plastic Debris. *Mar. Pollut. Bull.* **2016**, *113* (1–2), 17–24. https://doi.org/10.1016/j.marpolbul.2016.07.021.

(70) Liu, G.; Zhu, Z.; Yang, Y.; Sun, Y.; Yu, F.; Ma, J. Sorption Behavior and Mechanism of Hydrophilic Organic Chemicals to Virgin and Aged Microplastics in Freshwater and Seawater. *Environ. Pollut.* **2019**, *246*, 26–33. https://doi.org/10.1016/j.envpol.2018.11.100.

(71) Miranda, M. N.; Lado Ribeiro, A. R.; Silva, A. M. T.; Pereira, M. F. R. Can Aged Microplastics Be Transport Vectors for Organic Micropollutants? – Sorption and Phytotoxicity Tests. *Sci. Total Environ.* **2022**, *850*, 158073. https://doi.org/10.1016/j.scitotenv.2022.158073.

(72) Bhagat, K.; Barrios, A. C.; Rajwade, K.; Kumar, A.; Oswald, J.; Apul, O.; Perreault, F. Aging of Microplastics Increases Their Adsorption Affinity towards Organic Contaminants. *Chemosphere* **2022**, *298*, 134238. https://doi.org/10.1016/j.chemosphere.2022.134238.

(73) Wang, W.; Wang, J. Comparative Evaluation of Sorption Kinetics and Isotherms of Pyrene onto Microplastics. *Chemosphere* **2018**, *193*, 567–573. https://doi.org/10.1016/j.chemosphere.2017.11.078.

(74) *Advances in the Use of Liquid Chromatography Mass Spectrometry (LC-MS): Instrumentation, Developments and Application*; Cappiello, A., Ed.; Comprehensive analytical chemistry; Elsevier: Amsterdam, 2018.

(75) Termopoli, V.; Piergiovanni, M.; Ballabio, D.; Consonni, V.; Cruz Muñoz, E.; Gosetti, F. Condensed Phase Membrane Introduction Mass Spectrometry: A Direct Alternative to Fully Exploit the Mass Spectrometry Potential in Environmental Sample Analysis. *Separations* **2023**, *10* (2), 139. https://doi.org/10.3390/separations10020139.

(76) Duncan, K. D.; Hawkes, J. A.; Berg, M.; Clarijs, B.; Gill, C. G.; Bergquist, J.; Lanekoff, I.; Krogh, E. T. Membrane Sampling Separates Naphthenic Acids from Biogenic Dissolved Organic Matter for Direct Analysis by Mass Spectrometry. *Environ. Sci. Technol.* **2022**, *56* (5), 3096–3105. https://doi.org/10.1021/acs.est.1c07359.

(77) Monaghan, J.; Jaeger, A.; Agua, A. R.; Stanton, R. S.; Pirrung, M.; Gill, C. G.; Krogh, E. T. A Direct Mass Spectrometry Method for the Rapid Analysis of Ubiquitous Tire-Derived Toxin *N* -(1,3-Dimethylbutyl)- *N* ′-Phenyl- *p* -Phenylenediamine Quinone (6-PPDQ). *Environ. Sci. Technol. Lett.* **2021**, *8* (12), 1051–1056. https://doi.org/10.1021/acs.estlett.1c00794.

(78) Monaghan, J.; Richards, L. C.; Vandergrift, G. W.; Hounjet, L. J.; Stoyanov, S. R.; Gill, C. G.; Krogh, E. T. Direct Mass Spectrometric Analysis of Naphthenic Acids and Polycyclic Aromatic Hydrocarbons in Waters Impacted by Diluted Bitumen and Conventional Crude Oil. *Sci. Total Environ.* **2021**, *765*, 144206. https://doi.org/10.1016/j.scitotenv.2020.144206.

(79) Termopoli, V.; Famiglini, G.; Palma, P.; Cappiello, A.; Vandergrift, G. W.; Krogh, E. T.; Gill, C. G. Condensed Phase Membrane Introduction Mass Spectrometry with Direct Electron Ionization: On-Line Measurement of PAHs in Complex Aqueous Samples. *J. Am. Soc. Mass Spectrom.* **2016**, *27* (2), 301–308. https://doi.org/10.1007/s13361-015-1285-9.

(80) Fries, E.; Zarfl, C. Sorption of Polycyclic Aromatic Hydrocarbons (PAHs) to Low and High Density Polyethylene (PE). *Environ. Sci. Pollut. Res.* **2012**, *19* (4), 1296–1304. https://doi.org/10.1007/s11356-011-0655-5.

(81) Wang, J.; Guo, X. Adsorption Kinetic Models: Physical Meanings, Applications, and Solving Methods. *J. Hazard. Mater.* **2020**, *390*, 122156. https://doi.org/10.1016/j.jhazmat.2020.122156.

(82) Toro-Vélez, A.; Madera-Parra, C.; Peña-Varón, M.; García-Hernández, H.; Lee, W.; Walker, S.; Lens, P. Longitudinal Removal of Bisphenol-A and Nonylphenols from Pretreated Domestic Wastewater by Tropical Horizontal Sub-SurfaceConstructed Wetlands. *Appl. Sci.* **2017**, *7* (8), 834. https://doi.org/10.3390/app7080834.

(83) Hüffer, T.; Weniger, A.-K.; Hofmann, T. Sorption of Organic Compounds by Aged Polystyrene Microplastic Particles. *Environ. Pollut.* **2018**, *236*, 218–225. https://doi.org/10.1016/j.envpol.2018.01.022.

(84) Hüffer, T.; Hofmann, T. Sorption of Non-Polar Organic Compounds by Micro-Sized Plastic Particles in Aqueous Solution. *Environ. Pollut.* **2016**, *214*, 194–201. https://doi.org/10.1016/j.envpol.2016.04.018.

(85) Vockenberg, T.; Wichard, T.; Ueberschaar, N.; Franke, M.; Stelter, M.; Braeutigam, P. The Sorption Behaviour of Amine Micropollutants on Polyethylene Microplastics – Impact of Aging and Interactions with Green Seaweed. *Environ. Sci. Process. Impacts* **2020**, *22* (8), 1678–1687. https://doi.org/10.1039/D0EM00119H.

(86) Martínez-Romo, A.; González-Mota, R.; Soto-Bernal, J. J.; Rosales-Candelas, I. Investigating the Degradability of HDPE, LDPE, PE-BIO, and PE-OXO Films under UV-B Radiation. *J. Spectrosc.* **2015**, *2015*, 1–6. https://doi.org/10.1155/2015/586514.

(87) Rochman, C. M.; Hoh, E.; Hentschel, B. T.; Kaye, S. Long-Term Field Measurement of Sorption of Organic Contaminants to Five Types of Plastic Pellets: Implications for Plastic Marine Debris. *Environ. Sci. Technol.* **2013**, 130109073312009. https://doi.org/10.1021/es303700s.

(88) Lee, H.; Shim, W. J.; Kwon, J.-H. Sorption Capacity of Plastic Debris for Hydrophobic Organic Chemicals. *Sci. Total Environ.* **2014**, *470–471*, 1545–1552. https://doi.org/10.1016/j.scitotenv.2013.08.023.

(89) Teuten, E. L.; Rowland, S. J.; Galloway, T. S.; Thompson, R. C. Potential for Plastics to Transport Hydrophobic Contaminants. *Environ. Sci. Technol.* **2007**, *41* (22), 7759–7764. https://doi.org/10.1021/es071737s.

(90) Wu, C.; Zhang, K.; Huang, X.; Liu, J. Sorption of Pharmaceuticals and Personal Care Products to Polyethylene Debris. *Environ. Sci. Pollut. Res.* **2016**, *23* (9), 8819–8826. https://doi.org/10.1007/s11356-016-6121-7.

(91) Robeson, L. M.; Liu, Q.; Freeman, B. D.; Paul, D. R. Comparison of Transport Properties of Rubbery and Glassy Polymers and the Relevance to the Upper Bound Relationship. *J. Membr. Sci.* **2015**, *476*, 421–431. https://doi.org/10.1016/j.memsci.2014.11.058.

(92) Carraher Jr., C. E. *Introduction to Polymer Chemistry*, 0 ed.; CRC Press, 2017. https://doi.org/10.1201/9781315369488.

(93) Balani, K.; Verma, V.; Agarwal, A.; Narayan, R. *Biosurfaces: A Materials Science and Engineering Perspective*, 1st ed.; Wiley, 2014. https://doi.org/10.1002/9781118950623.

(94) Guo, X.; Chen, C.; Wang, J. Sorption of Sulfamethoxazole onto Six Types of Microplastics. *Chemosphere* **2019**, *228*, 300–308. https://doi.org/10.1016/j.chemosphere.2019.04.155.

(95) Wang, F.; Shih, K. M.; Li, X. Y. The Partition Behavior of Perfluorooctanesulfonate (PFOS) and Perfluorooctanesulfonamide (FOSA) on Microplastics. *Chemosphere* **2015**, *119*, 841–847. https://doi.org/10.1016/j.chemosphere.2014.08.047.

(96) Song, Y. K.; Hong, S. H.; Eo, S.; Shim, W. J. The Fragmentation of Nano- and Microplastic Particles from Thermoplastics Accelerated by Simulated-Sunlight-Mediated Photooxidation. *Environ. Pollut.* **2022**, *311*, 119847. https://doi.org/10.1016/j.envpol.2022.119847.

(97) Yousif, E.; Haddad, R. Photodegradation and Photostabilization of Polymers, Especially Polystyrene: Review. *SpringerPlus* **2013**, *2* (1), 398. https://doi.org/10.1186/2193-1801-2-398.

(98) Liu, P.; Qian, L.; Wang, H.; Zhan, X.; Lu, K.; Gu, C.; Gao, S. New Insights into the Aging Behavior of Microplastics Accelerated by Advanced Oxidation Processes. *Environ. Sci. Technol.* **2019**, *53* (7), 3579–3588. https://doi.org/10.1021/acs.est.9b00493.

(99) Liu, P.; Lu, K.; Li, J.; Wu, X.; Qian, L.; Wang, M.; Gao, S. Effect of Aging on Adsorption Behavior of Polystyrene Microplastics for Pharmaceuticals: Adsorption Mechanism and Role of Aging Intermediates. *J. Hazard. Mater.* **2020**, *384*, 121193. https://doi.org/10.1016/j.jhazmat.2019.121193.

(100) Letourneau, D. R.; Gill, C. G.; Krogh, E. T. Photosensitized Degradation Kinetics of Trace Halogenated Contaminants in Natural Waters Using Membrane Introduction Mass Spectrometry as an in Situ Reaction Monitor. *Photochem. Photobiol. Sci.* **2015**, *14* (11), 2108–2118. https://doi.org/10.1039/c5pp00286a.

(101) Hu, X.; Zhao, H. (Nina); Tian, Z.; Peter, K. T.; Dodd, M. C.; Kolodziej, E. P. Chemical Characteristics, Leaching, and Stability of the Ubiquitous Tire Rubber-Derived Toxicant 6PPD-Quinone. *Environ. Sci. Process. Impacts* **2023**, *25* (5), 901–911. https://doi.org/10.1039/D3EM00047H.

(102) Badawy, M. E. I.; El-Nouby, M. A. M.; Kimani, P. K.; Lim, L. W.; Rabea, E. I. A Review of the Modern Principles and Applications of Solid-Phase Extraction Techniques in Chromatographic Analysis. *Anal. Sci.* **2022**, *38* (12), 1457–1487. https://doi.org/10.1007/s44211-022-00190-8.

(103) Cao, G.; Wang, W.; Zhang, J.; Wu, P.; Qiao, H.; Li, H.; Huang, G.; Yang, Z.; Cai, Z. Occurrence and Fate of Substituted *p* -Phenylenediamine-Derived Quinones in Hong Kong Wastewater Treatment Plants. *Environ. Sci. Technol.* **2023**, *57* (41), 15635–15643. https://doi.org/10.1021/acs.est.3c03758.

(104) Rodgers, T. F. M.; Wang, Y.; Humes, C.; Jeronimo, M.; Johannessen, C.; Spraakman, S.; Giang, A.; Scholes, R. C. Bioretention Cells Provide a 10-Fold Reduction in 6PPD-Quinone Mass Loadings to Receiving Waters: Evidence from a Field Experiment and Modeling. *Environ. Sci. Technol. Lett.* **2023**, *10* (7), 582–588. https://doi.org/10.1021/acs.estlett.3c00203.

(105) Cao, G.; Wang, W.; Zhang, J.; Wu, P.; Zhao, X.; Yang, Z.; Hu, D.; Cai, Z. New Evidence of Rubber-Derived Quinones in Water, Air, and Soil. *Environ. Sci. Technol.* **2022**, *56* (7), 4142–4150. https://doi.org/10.1021/acs.est.1c07376.

(106) Feehan, J. F.; Monaghan, J.; Gill, C. G.; Krogh, E. T. Direct Measurement of Acid Dissociation Constants of Trace Organic Compounds at Nanomolar Levels in Aqueous Solution by Condensed Phase–Membrane Introduction Mass Spectrometry. *Environ. Toxicol. Chem.* **2019**, *38* (9), 1879–1889. https://doi.org/10.1002/etc.4519.

(107) Zvekic, M.; Vandergrift, G. W.; Tong, C. C.; Gill, C. G.; Krogh, E. T. Monitoring Microplastic–Contaminant Sorption Processes in Real-Time Using Membrane Introduction Mass Spectrometry. *Environ. Sci. Process. Impacts* **2023**, *25* (7), 1169–1180. https://doi.org/10.1039/D3EM00083D.

(108) Kim, K.-H.; Jahan, S. A.; Kabir, E.; Brown, R. J. C. A Review of Airborne Polycyclic Aromatic Hydrocarbons (PAHs) and Their Human Health Effects. *Environ. Int.* **2013**, *60*, 71–80. https://doi.org/10.1016/j.envint.2013.07.019.

(109) Kalam, S.; Abu-Khamsin, S. A.; Kamal, M. S.; Patil, S. Surfactant Adsorption Isotherms: A Review. *ACS Omega* **2021**, *6* (48), 32342–32348. https://doi.org/10.1021/acsomega.1c04661.

(110) Jesus, F.; Pereira, J. L.; Campos, I.; Santos, M.; Ré, A.; Keizer, J.; Nogueira, A.; Gonçalves, F. J. M.; Abrantes, N.; Serpa, D. A Review on Polycyclic Aromatic Hydrocarbons Distribution in Freshwater Ecosystems and Their Toxicity to Benthic Fauna. *Sci. Total Environ.* **2022**, *820*, 153282. https://doi.org/10.1016/j.scitotenv.2022.153282.

(111) Abraham, M. H.; McGowan, J. C. The Use of Characteristic Volumes to Measure Cavity Terms in Reversed Phase Liquid Chromatography. *Chromatographia* **1987**, *23* (4), 243–246. https://doi.org/10.1007/BF02311772.

(112) Vandergrift, G. W.; Krogh, E. T.; Gill, C. G. Polymer Inclusion Membranes with Condensed Phase Membrane Introduction Mass Spectrometry (CP-MIMS): Improved

Analytical Response Time and Sensitivity. *Anal. Chem.* **2017**, *89* (10), 5629–5636. https://doi.org/10.1021/acs.analchem.7b00908.

(113) *Reproductive Biology and Phylogeny of Chondrichthyes: Sharks, Batoids, and Chimaeras, Volume 3*, First edition.; Hamlett, W. C., Ed.; CRC Press: Boca Raton, FL, 2011.

(114) Osgood, G. J.; Timmer, B.; Cox, K.; Juanes, F.; Baum, J. K. Differences in δ^{15} N and δ^{13} C between Embryonic and Maternal Tissues of the Ovoviviparous Bluntnose Sixgill Shark *Hexanchus Griseus*. *J. Fish Biol.* **2020**, *96* (4), 1060–1064. https://doi.org/10.1111/jfb.14294.

(115) Salvo, A.; La Torre, G. L.; Rotondo, A.; Mangano, V.; Gervasi, T.; Gervasi, C.; Vadalà, R.; Bartolomeo, G.; Iaria, C.; Lanteri, G.; Capparucci, F.; Dugo, G. Accumulation of PCBs, PAHs, Plasticizers and Inorganic Elements in *Hexanchus Griseus* from the Strait of Messina (Central Mediterranean Sea). *Nat. Prod. Res.* **2020**, *34* (1), 172–176. https://doi.org/10.1080/14786419.2019.1601197.

(116) Hornung, H.; Krom, M. D.; Cohen, Y.; Bernhard, M. Trace Metal Content in Deep-Water Sharks from the Eastern Mediterranean Sea. *Mar. Biol.* **1993**, *115* (2), 331–338. https://doi.org/10.1007/BF00346351.

(117) Hejna, M.; Gottardo, D.; Baldi, A.; Dell'Orto, V.; Cheli, F.; Zaninelli, M.; Rossi, L. Review: Nutritional Ecology of Heavy Metals. *Animal* **2018**, *12* (10), 2156–2170. https://doi.org/10.1017/S175173111700355X.

(118) Nakajima, R.; Kawato, M.; Fujiwara, Y.; Tsuchida, S.; Ritchie, H.; Fujikura, K. Occurrence and Levels of Polybrominated Diphenyl Ethers (PBDEs) in Deep-Sea Sharks from Suruga Bay, Japan. *Mar. Pollut. Bull.* **2022**, *176*, 113427. https://doi.org/10.1016/j.marpolbul.2022.113427.

(119) IUCN. Hexanchus Griseus: Finucci, B., Barnett, A., Bineesh, K.K., Cheok, J., Cotton, C.F., Dharmadi, Graham, K.J., Kulka, D.W., Neat, F.C., Pacoureau, N., Rigby, C.L., Tanaka, S. & Walker, T.I.: The IUCN Red List of Threatened Species 2020: E.T10030A495630, 2019. https://doi.org/10.2305/IUCN.UK.2020-3.RLTS.T10030A495630.en.

(120) Legislative Services Branch. *Consolidated federal laws of canada, Species at Risk Act*. https://laws-lois.justice.gc.ca/eng/acts/S-15.3/20090305/P1TT3xt3.html (accessed 2023-12-23).

(121) Martins, M. F.; Costa, P. G.; Bianchini, A. Assessing Multigenerational Exposure to Metals in Elasmobranchs: Maternal Transfer of Contaminants in a Yolk-Sac Viviparous Species. *Mar. Pollut. Bull.* **2022**, *175*, 113364. https://doi.org/10.1016/j.marpolbul.2022.113364.

(122) Mull, C. G.; Lyons, K.; Blasius, M. E.; Winkler, C.; O'Sullivan, J. B.; Lowe, C. G. Evidence of Maternal Offloading of Organic Contaminants in White Sharks (Carcharodon

Carcharias). *PLOS ONE* **2013**, *8* (4), e62886. https://doi.org/10.1371/journal.pone.0062886.

(123) Khan, B.; Burgess, R. M.; Cantwell, M. G. Occurrence and Bioaccumulation Patterns of Per- and Polyfluoroalkyl Substances (PFAS) in the Marine Environment. *ACS EST Water* **2023**, *3* (5), 1243–1259. https://doi.org/10.1021/acsestwater.2c00296.

(124) Yang, D.; Han, J.; Hall, D. R.; Sun, J.; Fu, J.; Kutarna, S.; Houck, K. A.; LaLone, C. A.; Doering, J. A.; Ng, C. A.; Peng, H. Nontarget Screening of Per- and Polyfluoroalkyl Substances Binding to Human Liver Fatty Acid Binding Protein. *Environ. Sci. Technol.* **2020**, *54* (9), 5676–5686. https://doi.org/10.1021/acs.est.0c00049.

(125) Dassuncao, C.; Pickard, H.; Pfohl, M.; Tokranov, A. K.; Li, M.; Mikkelsen, B.; Slitt, A.; Sunderland, E. M. Phospholipid Levels Predict the Tissue Distribution of Poly- and Perfluoroalkyl Substances in a Marine Mammal. *Environ. Sci. Technol. Lett.* **2019**, *6* (3), 119–125. https://doi.org/10.1021/acs.estlett.9b00031.

(126) Foord, C. S.; Szabo, D.; Robb, K.; Clarke, B. O.; Nugegoda, D. Hepatic Concentrations of Per- and Polyfluoroalkyl Substances (PFAS) in Dolphins from South-East Australia: Highest Reported Globally. *Sci. Total Environ.* **2024**, *908*, 168438. https://doi.org/10.1016/j.scitotenv.2023.168438.

(127) Grønnestad, R.; Villanger, G. D.; Polder, A.; Kovacs, K. M.; Lydersen, C.; Jenssen, B. M.; Borgå, K. Maternal Transfer of Perfluoroalkyl Substances in Hooded Seals. *Environ. Toxicol. Chem.* **2017**, *36* (3), 763–770. https://doi.org/10.1002/etc.3623.

(128) Lee, K.; Alava, J. J.; Cottrell, P.; Cottrell, L.; Grace, R.; Zysk, I.; Raverty, S. Emerging Contaminants and New POPs (PFAS and HBCDD) in Endangered Southern Resident and Bigg's (Transient) Killer Whales (*Orcinus Orca*): *In Utero* Maternal Transfer and Pollution Management Implications. *Environ. Sci. Technol.* **2023**, *57* (1), 360–374. https://doi.org/10.1021/acs.est.2c04126.

(129) Barrett, H.; Du, X.; Houde, M.; Lair, S.; Verreault, J.; Peng, H. Suspect and Nontarget Screening Revealed Class-Specific Temporal Trends (2000–2017) of Poly- and Perfluoroalkyl Substances in St. Lawrence Beluga Whales. *Environ. Sci. Technol.* **2021**, *55* (3), 1659–1671. https://doi.org/10.1021/acs.est.0c05957.

(130) Barbo, N.; Stoiber, T.; Naidenko, O. V.; Andrews, D. Q. Locally Caught Freshwater Fish across the United States Are Likely a Significant Source of Exposure to PFOS and Other Perfluorinated Compounds. *Environ. Res.* **2023**, *220*, 115165. https://doi.org/10.1016/j.envres.2022.115165.

(131) Chynel, M.; Munschy, C.; Bely, N.; Héas-Moisan, K.; Pollono, C.; Jaquemet, S. Legacy and Emerging Organic Contaminants in Two Sympatric Shark Species from Reunion Island (Southwest Indian Ocean): Levels, Profiles and Maternal Transfer. *Sci. Total Environ.* **2021**, *751*, 141807. https://doi.org/10.1016/j.scitotenv.2020.141807.

(132) Wood, C. M. 1 - An Introduction to Metals in Fish Physiology and Toxicology: Basic Principles. In *Fish Physiology*; Wood, C. M., Farrell, A. P., Brauner, C. J., Eds.; Homeostasis and Toxicology of Essential Metals; Academic Press, 2011; Vol. 31, pp 1–51. https://doi.org/10.1016/S1546-5098(11)31001-1.

(133) Waldichuk, M. Pollution in the Strait of Georgia: A Review. *Can. J. Fish. Aquat. Sci.* **1983**, *40* (7), 1142–1167. https://doi.org/10.1139/f83-132.

(134) Waugh, L. C.; Flores Ruiz, I.; Kuang, C.; Guo, J.; Cullen, J. T.; Maldonado, M. T. Seasonal Dissolved Copper Speciation in the Strait of Georgia, British Columbia, Canada. *Front. Mar. Sci.* **2022**, *9*.

(135) Dutton, J.; Venuti, V. M. Comparison of Maternal and Embryonic Trace Element Concentrations in Common Thresher Shark (Alopias Vulpinus) Muscle Tissue. *Bull. Environ. Contam. Toxicol.* **2019**, *103* (3), 380–384. https://doi.org/10.1007/s00128-019-02667-1.

(136) Eisler, R. Trace Metal Changes Associated with Age of Marine Vertebrates. *Biol. Trace Elem. Res.* **1984**, *6* (2), 165–180. https://doi.org/10.1007/BF02916933.

(137) Kuang, C.; Stevens, S. W.; Pawlowicz, R.; Maldonado, M. T.; Cullen, J. T.; Francois, R. Factors Controlling the Temporal Variability and Spatial Distribution of Dissolved Cadmium in the Coastal Salish Sea. *Cont. Shelf Res.* **2022**, *243*, 104761. https://doi.org/10.1016/j.csr.2022.104761.

(138) Kruzynski, G. Cadmium in Oysters and Scallops: The BC Experience. *Toxicol. Lett.* **2004**, *148* (3), 159–169. https://doi.org/10.1016/j.toxlet.2003.10.030.

(139) Muir, D.; Miaz, L. T. Spatial and Temporal Trends of Perfluoroalkyl Substances in Global Ocean and Coastal Waters. *Environ. Sci. Technol.* **2021**, *55* (14), 9527–9537. https://doi.org/10.1021/acs.est.0c08035.

(140) Alves, L. M. F.; Nunes, M.; Marchand, P.; Le Bizec, B.; Mendes, S.; Correia, J. P. S.; Lemos, M. F. L.; Novais, S. C. Blue Sharks (Prionace Glauca) as Bioindicators of Pollution and Health in the Atlantic Ocean: Contamination Levels and Biochemical Stress Responses. *Sci. Total Environ.* **2016**, *563–564*, 282–292. https://doi.org/10.1016/j.scitotenv.2016.04.085.

(141) De Souza-Araujo, J.; Andrades, R.; De Oliveira Lima, M.; Hussey, N. E.; Giarrizzo, T. Maternal and Embryonic Trace Element Concentrations and Stable Isotope Fractionation in the Smalleye Smooth-Hound (Mustelus Higmani). *Chemosphere* **2020**, *257*, 127183. https://doi.org/10.1016/j.chemosphere.2020.127183.

(142) Ding, N.; Harlow, S. D.; Randolph Jr, J. F.; Loch-Caruso, R.; Park, S. K. Perfluoroalkyl and Polyfluoroalkyl Substances (PFAS) and Their Effects on the Ovary. *Hum. Reprod. Update* **2020**, *26* (5), 724–752. https://doi.org/10.1093/humupd/dmaa018.

(143) Baró-Camarasa, I.; Galván-Magaña, F.; Cobelo-García, A.; Marmolejo-Rodríguez, A. J. Major, Minor and Trace Element Concentrations in the Muscle and Liver of a Pregnant Female Pacific Sharpnose Shark (Rhizoprionodon Longurio) and Its Embryos. *Mar. Pollut. Bull.* **2023**, *188*, 114619. https://doi.org/10.1016/j.marpolbul.2023.114619.

(144) Lee, J.-W.; Jo, A.-H.; Lee, D.-C.; Choi, C. Y.; Kang, J.-C.; Kim, J.-H. Review of Cadmium Toxicity Effects on Fish: Oxidative Stress and Immune Responses. *Environ. Res.* **2023**, *236*, 116600. https://doi.org/10.1016/j.envres.2023.116600.

(145) Lee, J.-W.; Choi, H.; Hwang, U.-K.; Kang, J.-C.; Kang, Y. J.; Kim, K. I.; Kim, J.-H. Toxic Effects of Lead Exposure on Bioaccumulation, Oxidative Stress, Neurotoxicity, and Immune Responses in Fish: A Review. *Environ. Toxicol. Pharmacol.* **2019**, *68*, 101–108. https://doi.org/10.1016/j.etap.2019.03.010.

(146) Hauser-Davis, R. A. The Current Knowledge Gap on Metallothionein Mediated Metal-Detoxification in Elasmobranchs. *PeerJ* **2020**, *8*, e10293. https://doi.org/10.7717/peerj.10293.

(147) Lopes, C. A.; Araujo, N. L. F.; Rocha, L.; Monteiro, F.; Rocha, R. C. C.; Saint'Pierre, T. D.; Lutfi, D. S.; Vianna, M.; Hauser-Davis, R. A. Toxic and Essential Metals in Narcine Brasiliensis (Elasmobranchii: Narcinidae): A Baseline Ecotoxicological Study in the Southeast Atlantic and Preliminary Maternal Transfer Implications. *Mar. Pollut. Bull.* **2019**, *149*, 110606. https://doi.org/10.1016/j.marpolbul.2019.110606.

(148) Endo, T.; Kimura, O.; Ohta, C.; Koga, N.; Kato, Y.; Fujii, Y.; Haraguchi, K. Metal Concentrations in the Liver and Stable Isotope Ratios of Carbon and Nitrogen in the Muscle of Silvertip Shark (Carcharhinus Albimarginatus) Culled off Ishigaki Island, Japan: Changes with Growth. *PLoS ONE* **2016**, *11* (2), e0147797. https://doi.org/10.1371/journal.pone.0147797.

(149) Baró-Camarasa, I.; Marmolejo-Rodríguez, A. J.; Cobelo-García, A.; Palacios, M. D.; Murillo-Cisneros, D. A.; Galván-Magaña, F. Essential and Non-Essential Trace Element Concentrations in Muscle and Liver of a Pregnant Munk's Pygmy Devil Ray (Mobula Munkiana) and Its Embryo. *Environ. Sci. Pollut. Res.* **2022**, *29* (41), 61623–61629. https://doi.org/10.1007/s11356-021-17390-w.

(150) Taguchi, M.; Yasuda, K.; Toda, S.; Shimizu, M. Study of Metal Contents of Elasmobranch Fishes: Part 1—Metal Concentration in the Muscle Tissues of a Dogfish, Squalus Mitsukurii. *Mar. Environ. Res.* **1979**, *2* (3), 239–249. https://doi.org/10.1016/0141-1136(79)90021-7.

(151) Castro, J. I.; Sato, K.; Bodine, A. B. A Novel Mode of Embryonic Nutrition in the Tiger Shark, *Galeocerdo Cuvier*. *Mar. Biol. Res.* **2016**, *12* (2), 200–205. https://doi.org/10.1080/17451000.2015.1099677.

(152) Ohishi, Y.; Arimura, S.; Shimoyama, K.; Yamada, K.; Yamauchi, S.; Horie, T.; Hyodo, S.; Kuraku, S. Egg Yolk Protein Homologs Identified in Live-Bearing Sharks: Co-Opted in the Lecithotrophy-to-Matrotrophy Shift? *Genome Biol. Evol.* **2023**, *15* (3), evad028. https://doi.org/10.1093/gbe/evad028.

(153) Zhang, B.; Wei, Z.; Gu, C.; Yao, Y.; Xue, J.; Zhu, H.; Kannan, K.; Sun, H.; Zhang, T. First Evidence of Prenatal Exposure to Emerging Poly- and Perfluoroalkyl Substances Associated with E-Waste Dismantling: Chemical Structure-Based Placental Transfer and Health Risks. *Environ. Sci. Technol.* **2022**, *56* (23), 17108–17118. https://doi.org/10.1021/acs.est.2c05925.

(154) Li, A.; Zhuang, T.; Shi, J.; Liang, Y.; Song, M. Heavy Metals in Maternal and Cord Blood in Beijing and Their Efficiency of Placental Transfer. *J. Environ. Sci. China* **2019**, *80*, 99–106. https://doi.org/10.1016/j.jes.2018.11.004.

(155) Rosenboom, J.-G.; Langer, R.; Traverso, G. Bioplastics for a Circular Economy. *Nat. Rev. Mater.* **2022**, *7* (2), 117–137. https://doi.org/10.1038/s41578-021-00407-8.

(156) Broughton, E. The Bhopal Disaster and Its Aftermath: A Review. *Environ. Health* **2005**, *4* (1), 6. https://doi.org/10.1186/1476-069X-4-6.

(157) Ferronato, N.; Torretta, V. Waste Mismanagement in Developing Countries: A Review of Global Issues. *Int. J. Environ. Res. Public. Health* **2019**, *16* (6), 1060. https://doi.org/10.3390/ijerph16061060.

(158) Duncan, K. D.; Bergman, H.-M.; Lanekoff, I. A Pneumatically Assisted Nanospray Desorption Electrospray Ionization Source for Increased Solvent Versatility and Enhanced Metabolite Detection from Tissue. *The Analyst* **2017**, *142* (18), 3424–3431. https://doi.org/10.1039/C7AN00901A.

(159) Baragaño, D.; Ratié, G.; Sierra, C.; Chrastný, V.; Komárek, M.; Gallego, J. R. Multiple Pollution Sources Unravelled by Environmental Forensics Techniques and Multivariate Statistics. *J. Hazard. Mater.* **2022**, *424*, 127413. https://doi.org/10.1016/j.jhazmat.2021.127413.

(160) Richards, L. C.; Davey, N. G.; Gill, C. G.; Krogh, E. T. Discrimination and Geo-Spatial Mapping of Atmospheric VOC Sources Using Full Scan Direct Mass Spectral Data Collected from a Moving Vehicle. *Environ. Sci. Process. Impacts* **2020**, *22* (1), 173–186. https://doi.org/10.1039/C9EM00439D.

(161) Kirkwood-Donelson, K. I.; Dodds, J. N.; Schnetzer, A.; Hall, N.; Baker, E. S. Uncovering Per- and Polyfluoroalkyl Substances (PFAS) with Nontargeted Ion Mobility Spectrometry–Mass Spectrometry Analyses. *Sci. Adv.* **2023**, *9* (43), eadj7048. https://doi.org/10.1126/sciadv.adj7048.